Study on the analytical approach of anthocyanins on intestinal absorption by MALDI-MS imaging technique

咸, 兌勳

Study on the analytical approach of anthocyanins on intestinal absorption by MALDI-MS imaging technique

Tae-Hun Hahm

Kyushu University

2023

LIST OF CONTENTS

Abbreviation

- **A:** ATP-binding cassette (ABC); acetonitrile (ACN); average fluorescence intensity (A_{FL}); apical sodium dependent-bile acid transporter (ASBT)
- **C:** cyclosporine A (CSA); cyanidin (Cy); cyanidin-3-*O*-*β*-D-glucoside (Cy3G); cyanidin-3-*O*-*β*-D-galactoside (Cy3-Gal); cyanidin-3-*O*-(6-*O*-(4-*O*-(E)-*p*-coumaroyl)-*β*-D-glucopyranosyl)-(1→6)-[*β*-D-xylopyranosyl-(1→2)]-*β*-D-galactopyranoside (Cy3XCGG); cyanidin-3-*O*-(*β*-D-gluco-pyranosyl)-(1→6)-[*β*-D-xylopyranosyl-(1→2)]-*β*-D-galactopyranoside (Cy3XGG); cyanidin-3-*O*-(6-*O*-sinapoyl-*β*-D-glucopyranosyl)-(1→6)-[*β*-D-xylopyranosyl-(1→2)]-*β*-D-galactopyranoside (Cy3XSGG); cyanidin-3-*O*-(6-*O*-feruloyl-*β*-D-glucopyranosyl)-(1→6)-[*β*-D-xylo-pyranosyl-(1→2)]-*β*-D-galactopyranoside (Cy3XFGG); α-cyano-4-hydroxycinnamic acid (CHCA)
- **D:** 2,5-dihydroxybenzoic acid (DHB); 1,5-diaminonaphthalene (1,5-DAN); 3,4-dimethoxycinnamic acid (DMCA); deuterium chloride (DCl)
- **E:** estrone-3-sulfate (E3S); electrospray ionization (ESI); epicatechin-3-*O*-gallate (ECG)
- **F:** formic acid (FA); ferulic acid (FCA)
- **G:** glucose transporter 2 (GLUT2); glucuronide (GlcA);

- **H:** high performance liquid chromatography (HPLC); human umbilical vein endothelial cells (HUVECs)
- **I:** indium-tin oxide (ITO); internal standard (IS); interleukin 8 (IL-8)
- **K:** Krebs-Ringer bicarbonate (KRB)
- **L:** limit of detection (LOD); limit of quantification (LOQ); liquid chromatography-mass spectrometry (LC-MS);
- **M:** matrix-assisted laser desorption/ionization mass spectrometry (MALDI-MS); methyl (Me); Methanol-*d*4 (CD_3OD); pro-inflammatory markers monocyte chemoattractant protein-1 (MCP-1); multidrug resistance protein 2 (MRP2); monocarboxylate transporters (MCTs)
- **N:** nucleoside transporters (NTs)
- **O:** organic anion transporting polypeptide (OATP); *O*-dinitrobenzene (*O*-DNB)
- **P:** P-glycoprotein (P-gp); peptide transporter 1 (PepT1)
- **Q:** quantitative MALDI-MS (qMALDI-MS)
- **R:** rhodamine 6G (R6G); region of interest (ROI); relative standard deviation (RSD)
- **S:** Sprague-Dawley (SD); sulfate (Sul); sodium-dependent glucose transporter 1 (SGLT1)
- **T:** time-of-flight/mass spectrometry (TOF/MS); tetramethylsilane (TMS); theaflavin-3′-*O*-gallate (TF3′G); tumor necrosis factor-α (TNF-α); trifluoroacetic acid (TFA)
- **W:** wortmannin (WOR)

Chapter I

Introduction

Researches on physiologically active food compounds have been performed, among which polyphenols may exert the prevention of age-related diseases, such as cardio protective,[1] lipid and cholesterol-lowering,[2-5] anti-hypertensive,[6-9] anti-diabetes,[10,11] and anti-inflammatory[12-14] effects. Polyphenols are a group of natural phytochemicals having >2 hydroxyl (OH) groups in benzene ring and flavonoids are a typical phytochemical.

Flavonoids with C6-C3-C6 skeleton provide health benefits against the onset of chronic degenerative diseases, e.g., cancers, diabetes, and cardiovascular diseases (CVD). Hence, flavonoids could serve as a fascinating natural food supplement for our health.

Among the flavonoids, anthocyanins are a unique contributor to food quality by their characteristic colors. The name comes from a combination of greek *anthos* (flower) and *kyanous* (blue). The unique chemical properties are caused by flavylium cationic backbone, which can make them charged electrically.[15] Hence, anthocyanins can be used as a pH indicator. Change in color and chemical structure of anthocyanins by pH is shown in Figure 1-1. Anthocyanins are a subgroup of flavonoids from the structural aspect and are further classified by the position and number of methyl and hydroxyl substitutions in the flavylium cationic ring, as cyanidin (Cy), malvidin (Mal), delphinidin (Del), pelargonidin (Pel), petunidin (Pet), and peonidin (Peo).[16] They are

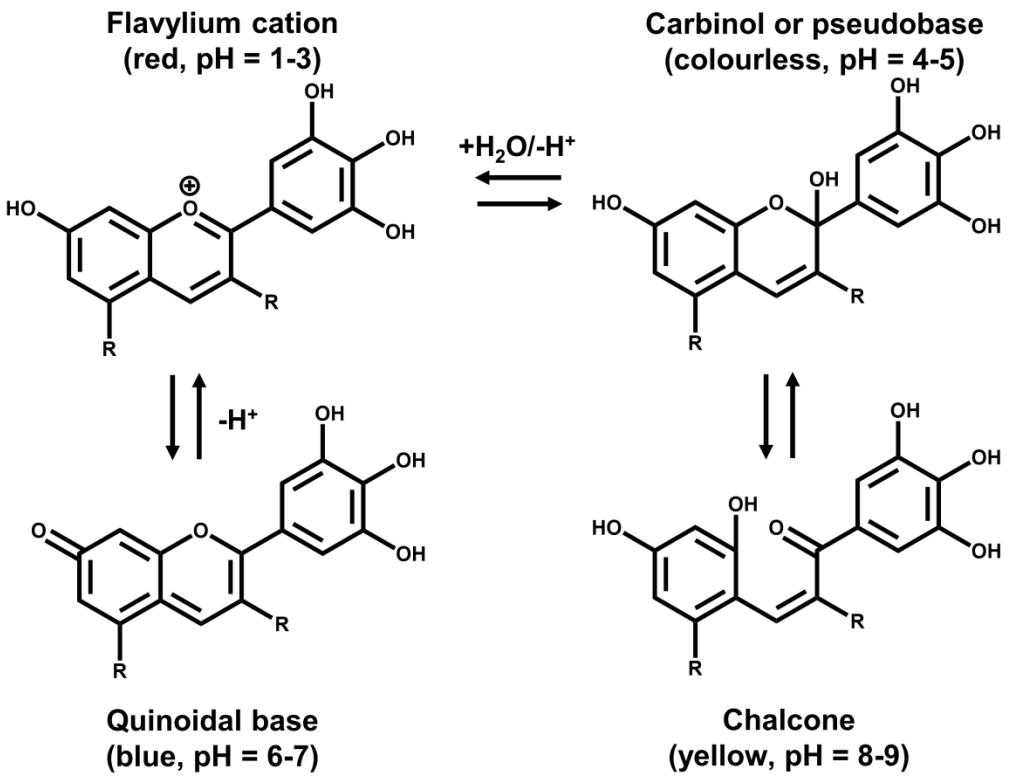

Figure 1-1 Chemical structures and color of anthocyanin in different pH

naturally modified via acylation and glycosylation to improve their solubility and stability in natural plants.[17] It has been reported that such diverse anthocyanins formed in natural plants have exhibited various health benefits, such as immunostimulation,[18] anti-tumor,[19,20] and anti-inflammatory[21,22] effects, as well as the prevention of diabetes[23,24] and hypertension.[25-28] For instance, the intake of bilberry extract reduced venous plasma glucose level in human trials.[23] Acylated (Cy-3-*O*-(6-*O*-feruloyl-*β*-D-glucopyranosyl)-(1→6)-[*β*-D-xylo-pyranosyl-(1→2)]-*β*-D-galactopyranoside, Cy3XFGG) anthocyanins and monoglycosylated (Cy-3-*O*-*β*-D-glucoside, Cy3G) have been reported to reduce the secretion of interleukin 8 (IL-8) in human umbilical vein endothelial cells (HUVECs) inflamed by tumor necrosis factor-α (TNF-α) and pro-inflammatory markers monocyte chemoattractant protein-1 (MCP-1).[29,30]

In order to demonstrate the aforementioned physiological actions of anthocyanins, it is necessary to clarify the effective bioavailability of anthocyanins after the intake *in vivo*.[31-36] As summarized in Table 1-1, studies on most anthocyanin absorption have been conducted using acylated anthocyanins, such as Cy-3-*O*-[*β*-D-xylopyranosyl-(1→2)]-*β*-D-galactopyranoside (Cy3XG), Cy-3-*O*-(*β*-D-gluco-pyranosyl)-(1→6)-[*β*-D-xylopyranosyl-(1→2)]-*β*-D-galactopyranoside (Cy3XGG), Cy-3-*O*-(6-*O*-(4-*O*-(*E*)-*p*-coumaroyl)-*β*-D-glucopyranosyl)-(1→6)-[*β*-D-xylopyranosyl-(1→2)]-*β*-D-galactopyranoside (Cy3XCGG), Cy-3-*O*-(6-*O*-sinapoyl-*β*-D-glucopyranosyl)-(1→6)-[*β*-D-xylopyranosyl-(1→2)]-*β*-D-galactopyranoside (Cy3XSGG), Cy3XFGG, etc.[37-49]

Table 1-1 Pharmacokinetics of anthocyanins in literature

Anthocyanins		Source	Dose	Species	Biological sample	Plasma conc. (pmol/mL)	Metabolite	Reference
cyanidin (Cy)	Cy-3-glucoside (Cy3G)	-	404 mg/kg (Cy3G)	Wistar	plasma, jejunum, stomach	-	cyanidin (aglycon)	[39]
		black currant	359 mg/kg (equiv. Cy3G)	Wistar	plasma, urine	C_{max}, 840 ± 190 T_{max}, 0.5 h	-	[42]
		black currant	0.165 mg/kg (equiv. Cy3G)	Human	plasma, urine	C_{max}, 5.0 ± 3.7 T_{max}, 1.25 ± 0.46 h	-	[42]
		elderberry, black currant	160 mg/kg (equiv. Cy3G)	SD	plasma, liver	C_{max}, 3490 T_{max}, 0.25 h	Methylated	[41]
		elderberry	720 mg/human (extract)	Human	plasma, urine	C_{max}, 42.5 ± 4.5 T_{max}, 1.08 ± 0.34 h	-	[44]
		redgrape juice	283.5 mg/human (juice)	Human	plasma, urine	C_{max}, 0.001 T_{max}, 0.5 h	-	[46,47]
		black raspberry	135 mg/human (equiv. Cy3G)	Human	plasma, urine	C_{max}, 0.005 T_{max}, 1.09 ± 0.30 h	glucuronided	[49]
	Cy-3,5-diglucoside (Cy3,5DG)	elderberry, black currant	20 mg/kg (equiv. Cy3,5DG)	SD	plasma, liver	-	-	[38,41]
		elderberry, black currant	0.25 mg/kg (equiv. Cy3,5DG)	Human	plasma	-	-	
		red cabbage	100-300 g/human (cooked)	Human	urine	-	-	
	Cy-3-rutinoside (Cy3R)	black currant	476 mg/kg (equiv. Cy3R)	Wistar	plasma, kidney, heart, bladder, urine	C_{max}, 840 ± 190 T_{max}, 0.5 h	-	[42]
		black raspberry	963 mg/human (equiv. Cy3R)	Human	plasma, urine	C_{max}, 0.038 T_{max}, 1.64 ± 0.50 h	glucuronided	[49]
		black currant	1.24 mg/kg (equiv. Cy3R)	Human	plasma, urine	C_{max}, 46.3 ± 22.5 T_{max}, 1.50 ± 0.53 h	-	[42]

Table 1-1 (Continued)

Anthocyanins	Source	Dose	Species	Biological sample	Plasma conc. (pmol/mL)	Metabolite	Reference
Cy-3-sambubioside (Cy3S)	black raspberry	85.5 mg/human (equiv. Cy3S)	Human	plasma, urine	C_{max}, 0.004 T_{max}, 2.18 ± 1.54 h	glucuronided	[49]
	elder berry	720 mg/human (extract)	Human	plasma, urine	C_{max}, 38.9 ± 7.4 T_{max}, 1.18 ± 0.28 h	-	[44]
Cy-3-rutinoside-5-glucoside	tart cherry	-	Wistar	kidney, heart, brain, bladder	-	-	[40]
Cy-3-arabinoside	choke berry	721 mg/human (extract)	Human	plasma, urine	-	-	[48]
Cy-3-galactoside	choke berry	721 mg/human (extract)	Human	plasma, urine	-	-	[48]
Cy-3-xylosyl rutinoside (Cy3XR)	black raspberry	256.5 mg/human (equiv. Cy3XR)	Human	plasma, urine	C_{max}, 0.009 T_{max}, 2.55 ± 0.16 h	glucuronided	[49]
Cy-3-diglucoside-5-glucoside	red cabbage	100-300 g/human (cooked)	Human	urine	-	-	[38]
Cy-3-(sinapoyl)-diglucoside-5-glucoside	red cabbage	100-300 g/human (cooked)	Human	urine	-	-	[38]
Cy-3-(glycopyranosyl-sinapoyl) diglucoside-5-glucoside	red cabbage	100-300 g/human (cooked)	Human	urine	-	-	[38]
Cy-3-(caffeoyl) (*p*-coumaroyl) diglucoside-5-glucoside	red cabbage	100-300 g/human (cooked)	Human	urine	-	-	[38]
Cy-3-(glycopyranosyl-feruloyl) diglucoside-5-glucoside	red cabbage	100-300 g/human (cooked)	Human	urine	-	-	[38]
Cy-3-(*p*-coumaroyl) -(sinapoyl) triglucoside-5-glucoside	red cabbage	100-300 g/human (cooked)	Human	urine	-	-	[38]

Table 1-1 (Continued)

Anthocyanins		Source	Dose	Species	Biological sample	Plasma conc. (pmol/mL)	Metabolite	Reference
	Cy-3-(*p*-coumaroyl) diglucoside-5-glucoside	red cabbage	100-300 g/human (cooked)	Human	urine	-	-	[38]
	Cy-3-(feruloyl) diglucoside-5-glucoside	red cabbage	100-300 g/human (cooked)	Human	urine	-	-	[38]
	Cy3XG	purple carrot	250 g/human (raw)	Human	plasma, urine	-	-	[37]
	Cy3XGG	purple carrot	250 g/human (raw)	Human	plasma, urine	-	-	[37]
	Cy3XSGG	purple carrot	250 g/human (raw)	Human	plasma, urine	-	-	[37]
	Cy3XFGG	purple carrot	250 g/human (raw)	Human	plasma, urine	-	-	[37]
	Cy3XCGG	purple carrot	250 g/human (raw)	Human	plasma, urine	-	-	[37]
delphinidin (Del)	Del-3-glucoside (D3G)	black currant	0.488 mg/kg (equiv. D3G)	Human	plasma, urine	C_{max}, 22.7 ± 12.4 T_{max}, 1.50 ± 0.53 h	-	[39]
		red grape	283.5 mg/human (juice)	Human	plasma, urine	C_{max}, 0.013 T_{max}, 0.5 h	-	[46.47]
	Del-3-rutinoside (D3R)	black currant	489 mg/kg (equiv. D3R)	Wistar	plasma, urine	C_{max}, 580 ± 410 T_{max}, 2.0 h	-	[42]
		black currant	1.68 mg/kg (equiv. D3R)	Human	plasma, urine	C_{max}, 73.4 ± 35.0 T_{max}, 1.75 ± 1.04 h	-	
		black currant	-	Wistar	plasma, urine	-	-	[43]
malvidin (Mal)	Mal-3-glucoside	red grape	117 mg/human (juice)	Human	plasma, urine	-	-	[45]
		red grape	283.5 mg/human (juice)	Human	plasma, urine	C_{max}, 0.092 T_{max}, 0.5 h		[46.47]

Table 1-1 (Continued)

Anthocyanins		Source	Dose	Species	Biological sample	Plasma conc. (pmol/mL)	Metabolite	Reference
peonidin (Peo)	Peo-3-glucoside	red grape	283.5 mg/human (juice)	Human	plasma, urine	C_{max}, 0.059 T_{max}, 0.5 h	-	[46.47]
	Peo-3-galactoside	choke berry	721 mg/human (extract)	Human	plasma, urine	-	-	[48]
	Peo-3-rutinoside	tart cherry	-	Wistar	kidney, heart, brain, bladder	-	-	[40]
	Peo-3-diglucoside-5-glucoside	red cabbage	100-300 g/human (cooked)	Human	urine	-	peonidin mono-glucuronide	[38]
petunidin (Pet)	Pet-3-glucoside	red grape	283.5 mg/human (juice)	Human	plasma, urine	C_{max}, 0.056 T_{max}, 0.5 h	-	[46.47]

-: Not available

In general, nutrients and food compounds may run into the body system after the diet. The intestinal tract is the first barrier responsible for the absorption of nutrients and physiologically active food compounds.[50-54] Except for hydrophobic compounds (e.g., drugs, and vitamin E, etc.) transported via the transcellular (epithelial tight junction, TJ) or passive paracellular transport system, most nutrients (monosaccharides, fatty acids, amino acids, di-/tripeptides, organic acids, and sterols, etc.) are recognized by diverse intestinal transporters[55-62] located at the brush border (brush border membrane or striated border) of the apical side of the enterocytes, along with the first and second phases (I/II) metabolism as one of the detoxification processes.[55] For anthocyanin absorption, anthocyanins have been reported to suffer from phase I hydrolysis, demethylation, and phase II metabolism such as methylation, glucuronidation, and sulfation.[63-66] Methylated form of Cy3G was detected in both the liver and plasma of SD rats after oral administeration of black currant and elderberry extracts (160 mg/kg).[41] In human trials, glucuronidated forms of Cy3G, Cy-3-*O*-*β*-D-rutinoside, Cy-3-*O*-*β*-D-sambubioside, and Cy-3-*O*-[*β*-D-xylopyranosyl-(1→2)]-*β*-D-rutinoside were detected in plasma samples after the intake of anthocyanin extracts.[31-36,49] These findings indicate that absorbed glycosylated anthocyanins may cause phase I/II metabolism during blood circulation and intestinal absorption. Thus, anthocyanin metabolites including phenolic metabolites and aglycon forms may also play a role in physiological access and action. However, metabolic behavior of anthocyanins still remains unascertained; in other words, it is important to get insights of metabolism of anthocyanins from the aspect of bioaccessibility in the body.

As mentioned earlier, the intestine expresses numerous transporters to deliver food compounds. The intestinal transporters include apical sodium dependent-bile acid transporter (ASBT),[56] nucleoside transporters (NTs),[57] organic anion transporting

polypeptides (OATP),[58] and monocarboxylate transporters (MCTs) for organic acids,[59] sodium-dependent glucose transporter 1 (SGLT1) for glucose,[60] peptide transporter 1 (PepT1) for di/tripeptides.[61] While compounds are incorporated into the intestinal microvillus membrane by influx transporters, some compounds may be pumped out into the gut by efflux ATP-binding cassette (ABC) transporters, including P-glycoprotein (P-gp), multidrug resistance protein 2 (MRP2), and breast cancer resistance protein (BCRP).[62] Thus far, to elucidate the transport routes of anthocyanins, a cell-based assay using Caco-2 cell monolayers, which imitate the intestinal epithelium layer, was performed with the aid of transport inhibitors[67-72] and an index of apparent permeability (P_{app}) (Table 1-2). As shown in Table 1-2, Cy3G, which is an anthocyanin monoglycoside, was transported through Caco-2 cell monolayers (P_{app} of 1.50×10^{-6} cm/s) in intact form.[69] In this report, Cy3G transport was inhibited by phlorizin (an inhibitor of SGLT1) and phloretin (an inhibitor of glucose transporter 2 (GLUT2)), indicated the involvement of both transporters in the intestinal absorption of Cy3G.[69] Furthermore, the transport routes for diverse anthocyanins, including aglycon, acylated, and/or glycosylated have not been clarified yet. Thus, although the bioavailability of anthocyanins has been extensively studied, the actual absorption behavior or bioavailability of anthocyanins remains unexpected.

Table 1-2 Anthocyanin transport through Caco-2 cell monolayers

Anthocyanins		Transporter	P_{app} (cm/s)	Reference
cyanidin (Cy)	Cy-3-glucoside	SGLT1, GLUT2	14.96 ± 1.88 x 10^{-7}	[69]
	Cy-3-galactoside	-	-	[72]
	Cy-3-rutinoside	-	-	[70]
	Cy-3,5-diglucoside	-	-	[68]
delphinidin (Del)	Del-3-glucoside	-	-	[68]
	Del-3-rutinoside	-	-	[70]
	Del-3,5-diglucoside	-	-	[67]
malvidin (Mal)	Mal-3-glucoside	-	-	[68]
	Mal-3,5-diglucoside	-	-	[67]
peonidin (Peo)	Peo-3-glucoside	-	-	[68]
	Peo-3-galactoside	-	-	[72]
petunidin (Pet)	Pet-3-glucoside	-	-	[68]
	Pet-3,5-diglucoside	-	-	[67]
pelargonidin (Pel)	Pel-3-glucoside	-	-	[71]
	Pel-3-malonylglucoside	-	-	[71]

-: Not available

In terms of methodology, although Caco-2-cell-monolayer-based experimental system could be useful to figure out the transport routes in combination with specific inhibitors or the siRNA technique, the cell model has certain downsides, such as differences in protease expression from intestinal epithelium cells and lack of a mucus layer. It has been also reported that the co-culture of a human colorectal adenocarcinoma cell line (HT-29; Human colon cancer) with the Caco-2 cell line did not exhibit the result as anticipated.[73] In the case of *in vivo* experimental models, experimental animals, mainly mice or rats, are generally employed to detect the target compounds in circulating blood via the liver after intestinal absorption. These *in vivo* experimental systems can reflect real behaviors of absorption and metabolism. However, the results observed from urine or plasma samples cannot provide information on the site of the metabolism and intestinal transport route(s) because of the limitation of analytical methods.

Lately, matrix-assisted laser desorption/ionization mass spectrometry (MALDI-MS) geneally known as “soft” ionization that can produce intact pseudomolecular ion species without fragmentation has been used for selective and simultaneous detection of ionizable food compounds even in complex matrix.[74-80] The advantages of MALDI-MS are high selectivity and sensitivity by selected mass units, as well as tolerance for impurities and high speed.[79,80] Thus, MALDI-MS has been employed for diverse food compounds such as lipids, proteins, carbohydrate, and polyphenols.[74-77] Currently, MALDI-MS-aided imaging technique comes into the limelight, since the extensive technique can visually provide not only the detection of target compounds presented in biological samples, but also the spatial distribution, or localization in tissues. As illustrated in Figure 1-2, target organs are cryosectioned into μm-thick slices and mouted onto an indium-tin oxide (ITO)-coated conductive glass slide. Upon irradiated by e.g., neodymium-doped yttrium aluminum garnet (Nd:YAG) laser, the sprayed

matrix reagent absorbs the light energy at 355 nm to sublimate and ionize the analytes with the matrix reagent in the matrix plume.[79] The analytes are subsequently detected with corresponding mass-to-charge ratio (*m/z*).

Considering the advantage of MALDI-MS and aforementioned issues in the experimental systems for intestinal absorption, a novel assay system, namely, *in situ* MALDI-MS with imaging techniques,[77] has been developed, which can visualize incorporated bioactive food compounds into the intestinal membrane tissue without using specific labels, such as antibodies (Figure 1-2). In this technique with *in situ* and *ex vivo* approaches, the rat intestinal membrane tissue is mounted on the Ussing chamber system, to obviously evaluate the transport dynamics of polyphenols which has physiological effects, such as vasorelaxation[75] and anti-atherosclerosis[76] in real intestinal tracts of the animals. In the previous study,[77] it has been indicated that the *in situ* MALDI-MS imaging technique clearly visualized not only the intestinal absorption process of the tissue accumulation of an absorbable polyphenol such as anthocyanins, epicatechin-3-*O*-gallate (ECG), but also non-absorbable theaflavin-3′-*O*-gallate (TF3′G) in intestinal tissue section. The intestinal incorporation of non-absorbable bioactive compounds was the first evidence that could only be clarified by the novel MS imaging technique. The visualization technique of *in situ* MALDI-MS imaging technique is applicable to determine the absorption routes involved in both the influx and efflux of bioactive compounds with the aid of the specific transport inhibitors.

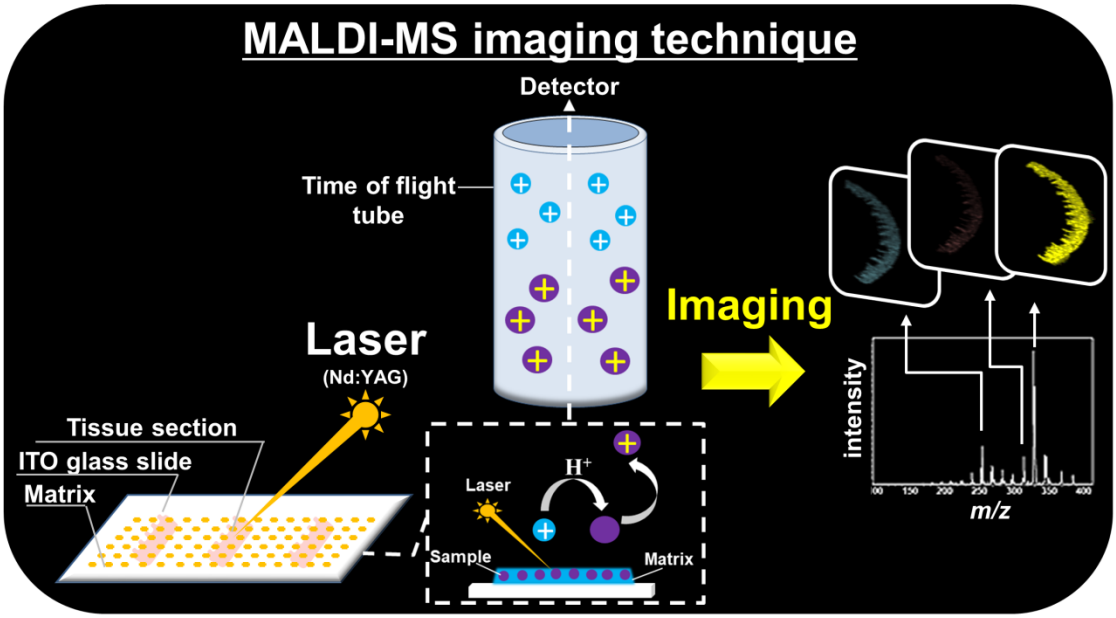

Figure 1-2 Matrix-assisted laser desorption/ionization mass spectrometry imaging technique

The matrix was sprayed onto indium-tin oxide (ITO) glass slide and tissue section. Target compounds on the tissue section were visualized by using matrix-assisted laser desorption/ionization mass spectrometry imaging (MALDI-MS imaging) technique.

Besides, the evidence of the tissue accumulation of orally administered bioactive food compounds such as anthocyanins and their metabolites has also been considered important to understand their physiological behavior *in vivo*. Furthermore, spatial distribution on the target organs is critical to determine the site and mechanism of action. Although the quantitative evaluation of the organ-accumulated amount of the bioactive food compounds has been generally performed by using liquid chromatography-mass spectrometry (LC-MS)-based assay systems that accompany tedious sample preparations,[40] the spatial information is lost throughout the homogenization processes. Moreover, since there are fewer specific labeling systems, such as antibodies,[74] for food compounds, the immunohistochemical staining is not applicable. Hence, the MALDI-MS imaging technique can be a useful tool that can visualize tissue accumulation of bioactive food compounds and only requires a simpler sample preparation and a smaller amount of biological tissue than the LC-MS technique. Despite having these advantages, MALDI-MS imaging technique was still rarely employed for the quantification approach, because, the fluctuation of matrix spray amount and heterogeneous crystallization of the matrix on the tissue section are serious problems in the quantitative capability of MALDI-MS imaging technique.[78-81] In particular, the lack of quantification due to the inhomogeneity of the internal standard sprayed on tissues during analytical runs is a critical issue to be solved for the improvement of the quantitative capability of MALDI-MS imaging technique. Although robotic matrix sprayers and spotters[82] have been developed to achieve reproducible matrix spraying, the homogeneity of matrix crystal and its distribution, and the amount on the tissue sections still cannot be monitored and controlled.

According to the aforementioned research background, although most studies on bioavailability such as intestinal absorption, metabolism, and tissue accumulation of

physiologically active anthocyanins have been reported to elucidate bioactivity and mechanisms *in vitro* and *in vivo*, detailed information is still lacking to understand fully and accurately on anthocyanin's bioavailability in organs. One of the factors would be considered as the lack of an analytical assay capable of accurate evaluation of their bioavailability. Thus, the aim of the present study was to clarify bioavailability such as intestinal absorption, metabolism, and tissue accumulation of food compounds like anthocyanins using *in situ* MALDI-MS imaging technique. Then, the present study also aimed to establish novel MALDI-MS imaging systems to visually and quantitatively assess the tissue accumulation of food compounds including the metabolites of acylated anthocyanins. The summaries for each chapter are described as follows:

1) In **Chapter II,** an *in situ* MALDI-MS with imaging technique was performed to evaluate the intestinal absorption process of anthocyanins, including an acylated Cy (Cy-3-(2"-xylose-6"-feruloyl-glucose-galactoside, Cy3XFGG) that exhibit *in vivo* hemodynamic improvement in rat blood vessels.[30] It was visualized that intact form of Cy3XFGG can be absorbed into intestinal tissue via OATP 2B1, while glycosylated anthocyanin form and its aglycon form were found to be favorably transported via both GLUT2 and OATP 2B1 transport routes.

2) In **Chapter III,** establishment of novel MALDI-MS imaging system was achieved visually and quantify the tissue accumulation of ferulic acid (FCA), which is one of anthocyanin's metabolites. Successful quantitative MALDI-MS imaging analysis of FCA were achieved in kidney tissues via fluorescence-assisted spraying method using R6G (the MS normalizing standard) in the 1,5-DAN solution containing *O*-DNB as an additive. Moreover, the present MALDI-MS imaging technique

quantitatively visualized tissue-accumulated FCA in kidneys after the oral administration (50 mg/kg B.W.).

Taken together, the present study has demonstrated for the first time that an intact form of acylated anthocyanin can be absorbed into the intestine via OATP 2B1 by *in situ* MALDI-MS imaging technique, and novel fluorescence-assisted spraying method improved quantitative capabilities of MALDI-MS imaging technique.

Chapter II

Visualization of rat intestinal absorption of acylated anthocyanins by MALDI-MS imaging technique

1. Introduction

As mentioned in **Chapter I**, anthocyanins, a group of flavonoids, provide several colors as natural pigments to plants, such as red and purple lettuce, grape, and carrot,[83] and have been reported to exhibit anti-hyperglycemic, anti-cancer, and anti-inflammatory effects.[20,21,26-28,84] The anthocyanin extract of *Daucus carota* L. (purple carrot) reduced secretion of IL-8, a pro-inflammatory marker, and MCP-1 in TNF-α-treated HUVECs.[29] In the previous report, a cremaster arteriole blood flow was improved following oral administration of the purple carrot extract (10 mg/kg) in rats via the activation of Akt signaling pathways and aortic endothelial nitric oxide synthase.[30] Health benefits of anthocyanins have been also provided by anti-mutagenic and anti-proliferative effects in Wistar rats,[85] anti-obesity effect in humans,[86] and anti-diabetic effect in streptozotocin-induced diabetic rats.[87]

Thus far, it has been reported that a monoglycosylated Cy, Cy3G,[16] can be detected in the circulatory system in its intact glycoside form in SD rats following oral administration.[88] Caco-2 cell assay exhibited that Cy3G can be transported via GLUT2.[69] Despite the aforementioned findings on bioavailability and physiological

effects of monoglycosylated anthocyanins, there have been no reports on intestinal absorption of “acylated” anthocyanins showing hemodynamic effects in rats.[30]

Thus, the aim of **Chapter II** was to clarify the intestinal absorption of acylated anthocyanins in SD rat experiments. An inhibitor-aided MALDI-MS imaging technique [77] was used to simultaneously analyze intestinal absorption behaviors, including metabolism and transport route(s) of acylated anthocyanins. Purple carrots were used in this study, since they have rich acylated anthocyanins and exhibit *in vivo* hemodynamic improvement in rat blood vessels.[30]

2. Materials and methods

2.1. Materials

Estrone-3-sulfate (E3S), nifedipine, and 2,5-dihydroxybenzoic acid (DHB) were purchased from Sigma-Aldrich Co. (St. Louis, MO, USA). Cy and Cy3G were purchased from Tokiwa Phytochemical Co., Ltd. (Chiba, Japan). Wortmannin (WOR) was purchased from Enzo Life Science (Lausen, Switzerland). Tetramethylsilane (TMS), phytic acid and cyclosporine A (CSA) were obtained from Nacalai Tesque Co. (Kyoto, Japan). Phloretin was obtained from Wako Pure Chemical Ind. (Osaka, Japan). Methanol-d_4 (CD_3OD), and deuterium chloride (DCl) were purchased from Sigma-Aldrich Co. Sevoflurane was purchased from Maruishi Pharmaceutical Co. Ltd. (Osaka, Japan). All other chemicals were employed without further purification and were of analytical reagent grade.

2.2. Preparation of anthocyanin extract in purple carrot

A powdered extract of anthocyanins from purple carrots (*Daucus carota* L.) was prepared according to previous report.[30] In brief, the concentrate of purple carrot, purchased from Diana Naturals (Antrain, France), was subjected to a liquid-liquid extraction with an equivalent volume of ethyl acetate. The aqueous phase was applied onto a Sephadex LH20 column (5.1 × 60 cm; GE Healthcare UK Ltd, Amersham Place, England). The purple-colored fraction was eluted with 30% methanol, and was evaporated, and stored at −80 °C.

Anthocyanins in the purple carrot extract were isolated by a high performance liquid chromatography (HPLC) separation on a Develosil ODA-HG-5 column (20 × 250 mm) from Nomura Chemical. Co., Ltd. (Aichi, Japan) using the elution of 0.1%

trifluoroacetic acid (TFA) for mobile phase A and a methanol solution containing 0.1% TFA for mobile phase B, with the following gradient: 26% B from 0 to 80 min; 100% B from 80 to 110 min at 1.0 mL/min with monitoring absorbance at 520 nm.

2.3. ^{1}H NMR and MS measurements

A mixed solvent consisting of CD_3OD containing DCL and TMS as an internal reference compound was used for all one-dimensional (1D) ^{1}H NMR measurements. The NMR measurement conditions were set as follows: an acquisition time of 2.18 s, 16,384 acquisition data points, 8 scans, relaxation delay of 5 s, and spinning at 15 Hz. The ^{1}H NMR spectra were referenced using TMS at 0 ppm. ^{1}H NMR spectra of five anthocyanins (1 mg in 0.8 mL of CD_3OD/DCl) were acquired at 25 ℃ using an ECS-400 spectrometer (JEOL, Tokyo, Japan).

Time-of-flight/mass spectrometry (TOF/MS) measurements were performed using a micrOTOF-II mass spectrometer (Bruker Daltonics, Bremen, Germany). Purple carrot extract was diluted 1:10 (V/V) in methanol (HPLC grade) for the TOF/MS experiments in the positive ion mode and directly infused at a flow of 10 µL/min. The MS conditions were set as follows: drying temperature of 200 ℃; capillary voltage of 3800 V; and nebulizing gas pressure of 1.6 bar. Data acquisition and analysis were performed using Bruker Data Analysis 3.2 software.

2.4. Oral administration of anthocyanin extract to Sprague-Dawley (SD) rats

The purple carrot extract dissolved in the saline solution (0.9% NaCl) was administered orally to male 8 week-old SD rats (SPF/VAF Crj, 292.7 ± 3.8 g); Charles River Japan; Kanagawa, Japan at a dose of 30 mg/kg. At 60 min following oral administration, blood from either the abdominal aorta or the portal vein was collected into blood collection tubes containing EDTA-2Na. Blood samples were centrifuged at

4 ℃ for 15 min at 3,500 × *g* to obtain plasma, which was immediately frozen and stored at −80 ℃ before LC-TOF/MS analysis. SD rats were sacrificed via exsanguination from the abdominal aorta during induction of anesthesia by volatile anesthetic agents, sevoflurane. All animal experiments were performed conforming to the Guideline for Animal Experiments in the Faculty of Agriculture in the Graduate School of Kyushu University, and conforming to law (low no. 105, 1973 and notification no. 71, 2006) and Notification (No. 6, 1980 of the Prime Minister's Office) of the Japanese Government. All experimental processes were reviewed and approved by the Animal Care and Use Committee of Kyushu University (permit number: A30-015-5).

2.5. *In situ* intestinal transport experiments

Intestinal transport experiments using jejunum membranes from SD rats were carried out in accordance with our previous report.[77] Namely, the jejunum segment (15–20 cm below the stomach) was washed out with Krebs-Ringer bicarbonate solution (KRB, pH 7.4, 4.8 mM KCl, 2.5 mM $CaCl_2$, 1.3 mM KH_2PO_4, 118.1 mM NaCl, 1.2 mM $MgSO_4$, 10 mM D-glucose, and 25 mM $NaHCO_3$). The jejunum was subsequently cut along the mesenteric border to expose the mucosal surfaces and mounted onto the Dual Channel Model Ussing Chamber (model U-2500) from Warner Instrument (Hamden, CT, USA). An aliquot (5 mL) of KRB solution was filled up to the apical (pH 6.0) and basolateral (pH 7.4) sides, respectively. For inhibitor-aided transport experiments with inhibitor, KRB solution containing inhibitors (20 μM CSA as an inhibitor of ATP-binding cassette (ABC) transporters, 100 μM E3S as an inhibitor of OATP, 1 μM WOR as an inhibitor of transcytosis, or 200 μM phloretin as an inhibitor of GLUT2) dissolved in 0.05% DMSO was used as the solution of apical side. After 15 min of incubation, the apical solution was replaced with KRB solution containing 100 μM Cy, Cy3G, or Cy3XFGG in the presence or absence of each inhibitor. Then, intestinal transport experiments of

anthocyanins were conducted for 60 min. During the intestinal transport period, a 95:5 O_2/CO_2 mixture was regularly bubbled into apical and basolateral solutions via air vents of the Ussing chamber to provide stirring and improve tissue viability during transport experiment. Apical and basolateral solutions were immediately retrieved for subsequent LC-TOF/MS analysis after 60 min of transport experiment, the jejunum membranes were washed out twice with KRB solution and immediately frozen in powdered dry ice. The frozen jejunum membranes were subsequently stored at −30 ℃ before MALDI-MS imaging analysis.

2.6. LC-TOF/MS analysis

An aliquot (4 mL) of the retrieved apical or basolateral solutions following 60 min of transport experiment was mixed with 1 mL of 5% TFA containing Del-3-*O*-*β*-D-glucoside as an internal standard (10 nmol/mL) to maintain stable flavylium cation in acidic aqueous solution. An aliquot (100 µL) of plasma was mixed with 500 µL of 5% TFA containing IS, and was applied to a Waters Sep-PakC18 short cartridge (360 mg sorbent, Waters, Milford, MA, USA), and eluted with methanol containing 0.1% TFA. The eluate was subsequently evaporated to dryness and dissolved in 100 µL of LC grade water containing 5% formic acid (FA). An aliquot (20 µL) of the solution was injected into an LC-TOF/MS system. LC separation of anthocyanins was carried out using an Agilent 1200 series HPLC (Agilent Technologies, Waldbronn, Germany) equipped with a binary pump (G1312A), a thermostatically controlled oven compartment (G1316A), a micro degasser (G1379B), and Cosmosil 5C18-MS-II column (2.0 × 150 mm, Nacalai Tesque Co.). The mobile phase containing solvent A (LC grade water containing 5% FA) and solvent B (acetonitrile (ACN) containing 0.1% FA) was employed to establish a linear gradient from 0 to 100% of solvent B over 30 min at 40 ℃ at a flow rate of 0.2 mL/min. MS analysis was carried out using a

micrOTOF-II mass spectrometer (Bruker Daltonics, Bremen, Germany) with a single TOF/MS reflector-mode. Ionization was performed by electrospray ionization (ESI) in the positive ion mode, and the mass range was set to 100–1300 *m/z*. The ESI-MS conditions were set as follows: drying temperature of 200 ℃; drying gas (nitrogen) at a flow rate of 8.0 L/min; capillary voltage of 3800 V; and nebulizing gas pressure of 1.6 bar. Calibration was carried out at the initiation of each analytical run using 10 mM sodium formate in 50% ACN. Data acquisition and analysis were performed using Bruker Data Analysis 3.2 software.

2.7. MALDI-MS imaging analysis

The frozen intestinal tissue was sliced into 12 µm-thick tissue sections using a CryoStar NX70 (Thermo Scientific, MA, USA) at −25 °C. The tissue sections were thaw-mounted onto an ITO-coated conductive glass slide (Bruker Daltonics) and dried under nitrogen (N_2) gas flow. An automatic matrix sprayer, ImagePrep (Bruker Daltonics) was employed to spray the matrix evenly over the ITO glass slide. DHB (20 mg/mL in 70% ACN) containing 20 mM phytic acid was used as matrix reagent.[77] The following spraying conditions were set: modulation 20%; spray power 20%; spraying time of 1.5 s; spraying for 90–100 cycles; incubation time of 10 s; and drying time of 60 s. MALDI-MS imaging technique was performed using an Autoflex III mass spectrometer equipped with a SmartBeam (Bruker Daltonics). MALDI-MS imaging technique in the positive ion-linear mode was carried out to analyze Cy ($[M]^+$, 287.1 *m/z*), Cy3G ($[M]^+$, 449.1 *m/z*), Cy3XFGG ($[M]^+$, 919.3 *m/z*), as well as CSA ($[M+H]^+$, 1202.8 *m/z*) and WOR ($[M+Na]^+$, 451.1 *m/z*). For phloretin ($[M-H]^-$, 273.1 *m/z*) and E3S ($[M-H]^-$, 349.1 *m/z*) detections, MALDI-MS data were obtained in the negative ion-linear mode using nifedipine (20 mg/mL) containing phytic acid (20 mM) as a matrix reagent.[77] MS parameters were as follows: laser frequency of 200 Hz; laser

focus range of 100%; laser power of 36%; off set of 59%; range of 20%; ion source 1 of 20.00 kV; ion source 2 of 18.80 kV; lens voltage of 7.50 kV; value of 6.0%; and gain of 12.00. MALDI-MS imaging analysis was carried out at a raster width of 50 µm. The obtained MS spectra were analyzed by Flexanalysis software (version 3.3, Bruker Daltonics, Bremen, Germany) as the sum of all spectra obtained from the tissue region of MS image. MS image data were reconstituted for visualization of spatial distribution with mass filtering of ± 0.2 *m/z* by Flex-imaging software (version 2.1, Bruker Daltonics, Bremen, Germany). In this study, relative MS intensity (%) of analytes against DHB intensity was used to compare MS spectra of anthocyanins incorporated in tissue sections.

2.8. Statistical data analysis

The results are expressed as the mean ± standard error of mean (SEM) obtained from three independent samples. The analysis was conducted between multiple groups by using a one-way analysis of variance followed by the Tukey-Kramer test for post-hoc analysis. A P value < 0.05 was considered statistically significant. All analyses were carried out by Stat View J 5.0 (SAS Institute Inc., Cary, NC, USA).

3. Results and discussion

3.1. *In vivo* intestinal absorption of purple carrot anthocyanins in SD rats

There have been numerous reports regarding the physiological effects of anthocyanins in humans and animals, including anti-diabetes,[87] anti-cancer,[20] hemodynamic,[30] and anti-inflammation effects.[29] In order to clarify these physiological characteristics, it is important to clarify absorption process. Lately, there have been conflicting opinions on intestinal absorption of anthocyanins whether they must be metabolized and/or degraded by gut microbiota[16] or if they can be absorbed into the intestine in their intact form.[69] In particular, the bioavailability such as metabolism and absorption route(s) of acylated anthocyanins remains unidentified. In **Chapter II**, as summarized in Table 2-1, the extract obtained from purple carrots comprised five major anthocyanins with their content range of 0.34 − 2.92 mg/g. These anthocyanins were also identified by using ^{1}H NMR and the exact mass of TOF/MS (Tables 2-1 and 2-2). Although degradation of anthocyanin aglycon to phenolic acids, including hippuric acid, ferulic acid, and vanillic acid,[69] cannot be excluded, the lack of Cy (and monoglycosylated anthocyanins) in the purple carrot extract used in the present study suggested that glycosylated anthocyanin forms may be stable in the purple carrot matrix; this is consistent with a previous reported result revealing that purple carrot anthocyanins such as Cy3XG, Cy3XGG, Cy3XCGG, Cy3XSGG, and Cy3XFGG do not convert their structures throughout heat-processing of purple carrot juice.[89] Acylated anthocyanins such as Cy3XCGG, Cy3XSGG, and Cy3XFGG, have been reported to be prevailing anthocyanins in purple carrot extract.[90] In the purple carrot (*Daucus carota* L.) used in the present study, an acylated form, Cy3XFGG, exhibited the highest content (2.92 ± 0.01 mg/g) among the five major anthocyanins (Table 2-1). The anthocyanins of purple carrot extract (30 mg/kg) were orally administered to SD

rats to elucidate whether and which anthocyanins are absorbed into the small intestine in their intact form. Surprisingly, all five anthocyanins derived from the purple carrot (Figure 2-1) were clearly detected by LC-TOF/MS in intact anthocyanin form in both the circulating and portal blood at 60 min following oral administration (Figures 2-2 and 2-3). Their plasma levels ranged from 0.2% (percentage of absorption) or 0.92 ± 0.02 pmol/mL-plasma (Cy3XSGG) to 2.2% (percentage of absorption) or 39.3 ± 0.1 pmol/mL-plasma (Cy3XFGG). These results indicate that some acylated and/or non-acylated anthocyanins can get through the intestinal brush border membrane and enter the circulatory blood system via the liver (Figure 2-3). Among the five major anthocyanins, Cy3XFGG with bulky glycosylated and acylated moieties showed a significantly highest concentration (39.3 ± 0.1 pmol/mL-plasma; $P < 0.05$) in SD rat's blood (Figure 2-3). Assuming from these results of a bulky Cy3XFGG that exhibited the highest concentration among the three major acylated anthocyanins detected in its intact form into bloodstream in Figures 2-2 and 2-3, the feruloyl group of a bulky Cy3XFGG may be a crucial factor for intestinal absorption process. Thus, the detection of a bulky Cy3XFGG into bloodstream allowed further investigation and discussion on absorption route(s) and its metabolism during the intestinal absorption process.

Table 2-1 Anthocyanins extracted from *Daucus carota* L.

Anthocyanin targeted in this study	Abbreviation	Content in purple carrot extract (mg/g)	*m/z* (Theo./Exp.)
cyanidin (aglycon)	Cy	*n.d.*	287.0550/-
cyanidin 3-*O*-[*β*-D-xylopyranosyl-(1→2)]-*β*-D-galactopyranoside	Cy3XG	0.98 ± 0.06	581.1501/581.1502
cyanidin 3-*O*-(*β*-D-glucopyranosyl)-(1→6)-[*β*-D-xylopyranosyl-(1→2)]-*β*-D-galactopyranoside	Cy3XGG	0.34 ± 0.03	743.2029/743.1956
cyanidin 3-*O*-(6-*O*-(4-*O*-(*E*)-*p*-coumaroyl)-*β*-D-glucopyranosyl)-(1→6)-[*β*-D-xylopyranosyl-(1→2)]-*β*-D-galactopyranoside	Cy3XCGG	0.70 ± 0.01	889.2397/889.2391
cyanidin 3-*O*-(6-*O*-feruloyl-*β*-D-glucopyranosyl)-(1→6)-[*β*-D-xylopyranosyl-(1→2)]-*β*-D-galactopyranoside	Cy3XFGG	2.92 ± 0.01	919.2503/919.2491
cyanidin 3-*O*-(6-*O*-sinapoyl-*β*-D-glucopyranosyl)-(1→6)-[*β*-D-xylopyranosyl-(1→2)]-*β*-D-galactopyranoside	Cy3XSGG	0.68 ± 0.04	949.2608/949.2667

Table 2-2 ^{1}H NMR data of five anthocyanins extracted from *Daucus carota* L.

Cy3XG		
^{1}H NMR		
Position	***δ* (ppm)**	**Multiplicity (Hz)**
Cy (aglycon)		
H-4	8.989	s
H-6	6.676	d (2.2)
H-8	6.928	d (1.2)
H-2'	8.077	d (1.2)
H-5'	7.034	d (1.6)
H-6'	8.290	dd (1.3, 3.0)
Galactose		
H-1	5.408	d (2.4)
H-2	4.220	dd (~1, 4.5)
H-3	3.897	dd (~1, 2.3)
H-4	3.966	dd (2.0, *n.d.*)
H-5	*n.d.*	*n.d.*
H-6	4.843	*n.d.*
Xylose		
H-1	4.687	d (5.2)
H-2	3.148	dd (~2, *n.d.*)
H-3	3.272	dd (3.2, *n.d.*)
H-4	3.348	ddd (2.3, 9.0, *n.d.*)
H-5A	3.015	d (~1)
H-5B	3.613	*n.d.*

n.d.: Not detected

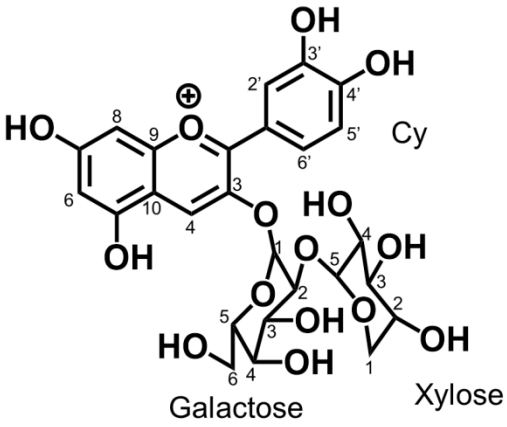

Table 2-2 (Continued)

Cy3XGG		
^{1}H NMR		
Position	**δ (ppm)**	**Multiplicity (Hz)**
Cy (aglycon)		
H-4	8.994	s
H-6	6,688	d (1.4)
H-8	6,940	d (3.2)
H-2'	8.102	d (1.6)
H-5'	7.048	d (2.0)
H-6'	8.313	dd (2.0, 3.5)
Galactose		
H-1	5.418	d (1.1)
H-2	4.256	dd (4.1, *n.d.*)
H-3	3.909	dd (3.0, 5.5)
H-4	3.917	dd (2.3, *n.d.*)
H-5	3.883	*n.d.*
H-6A	4.102	*n.d.*
H-6B	4.055	*n.d.*
Glucose		
H-1	*n.d.*	*n.d.*
H-2	3.252	dd (~2, *n.d.*)
H-3	*n.d.*	*n.d.*
H-4	3.199	d (2.9)
H-5	3.268	ddd (2.1, 9.0, *n.d.*)
H-6A	3.894	dd (3.0, *n.d.*)
H-6B	3.697	dd (3.2, 6.0)
Xylose		
H-1	4.734	d (2.3)
H-2	3.128	dd (1.2, 3.2)
H-3	3.339	dd (3.8, *n.d.*)
H-4	3.415	ddd (2.0, 9.1, 11.3)
H-5A	3.697	*n.d.*
H-5B	*n.d.*	*n.d.*

n.d.: Not detected

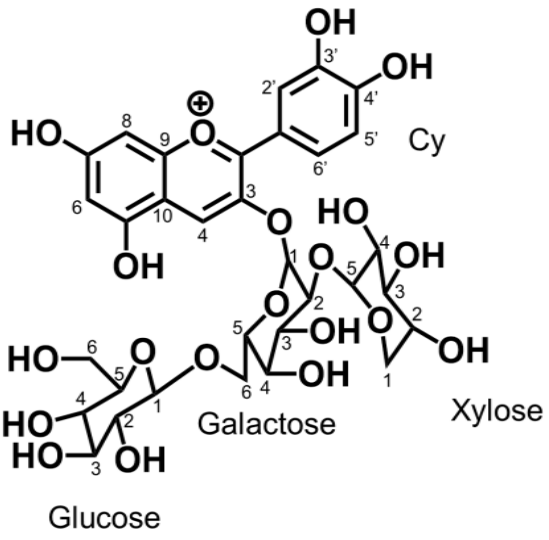

Table 2-2 (Continued)

Cy3XSGG		
	^{1}H NMR	
Position	**δ (ppm)**	**Multiplicity (Hz)**
Cy (aglycon)		
H-4	8.498	s
H-6	6.675	d (1.3)
H-8	6.525	d (1.4)
H-2'	7.948	d (2.1)
H-5'	7.044	d (2.9)
H-6'	8.152	dd (2.1, 8.9)
Galactose		
H-1	5.310	d (2.3)
H-2	4.304	dd (3.0, *n.d.*)
H-3	4.224	dd (2.5, 6.3)
H-4	3.974	dd (3.9, 9.0)
H-5	4.525	*n.d.*
H-6A	4.263	*n.d.*
H-6B	3.781	*n.d.*
Glucose		
H-1	4.520	*n.d.*
H-4	3.770	d (3.5)
H-6A	5.342	dd (7.7, 9.3)
H-6B	4.139	dd (~3, *n.d.*)
Xylose		
H-1	*n.d.*	*n.d.*
H-2	3.228	dd (5.0, *n.d.*)
H-4	3.272	ddd (~2, 6.5, *n.d.*)
H-5A	3.638	*n.d.*
H-5B	3.145	*n.d.*
Sinapinic acid		
H-2/H-6	6.213	*n.d.*
H-7	7.340	dd (7.8, 8.9)
H-8	6.193	dd (6.0, *n.d.*)
H-10/H-11	3.459	*n.d.*

n.d.: Not detected

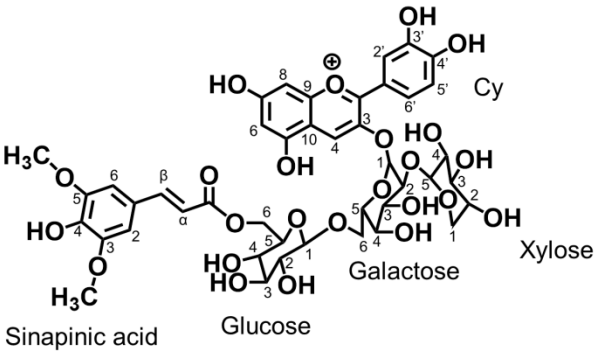

Table 2-2 (Continued)

Cy3XFGG		
^{1}H NMR		
Position	***δ* (ppm)**	**Multiplicity (Hz)**
Cy (aglycon)		
H-4	8.516	s
H-6	6.668	d (2.3)
H-8	6.533	d (1.4)
H-2'	7.945	d (2.3)
H-5'	7.071	d (8.7)
H-6'	8.103	dd (2.3, 8.7)
Galactose		
H-1	5.285	d (7.3)
H-2	*n.d.*	*n.d.*
H-3	4.188	dd (3.2, 4.0)
H-4	3.948	dd (2.3, *n.d.*)
H-5	*n.d.*	*n.d.*
H-6A	4.265	*n.d.*
H-6B	3.770	*n.d.*
Glucose		
H-1	4.488	d (6.4)
H-2	3.542	*n.d.*
H-3	3.542	*n.d.*
H-4	3.765	d (2.1)
H-5	3.542	*n.d.*
H-6A	5.339	dd (1.2, 4.0)
H-6B	4.152	dd (7.0, *n.d.*)
Xylose		
H-1	4.721	d (7.3)
H-2	3.272	dd (4.5, *n.d.*)
H-3	3.439	dd (2.0, *n.d.*)
H-4	*n.d.*	*n.d.*
H-5A	3.579	*n.d.*
H-5B	*n.d.*	*n.d.*
Ferulic acid		
H-2	6.498	d (1.8)
H-5	6.341	d (8.2)
H-6	6.578	dd (2.0, 6.9)
H-7	7.328	d (16.0)
H-8	6.164	d (16.0)

n.d.: Not detected

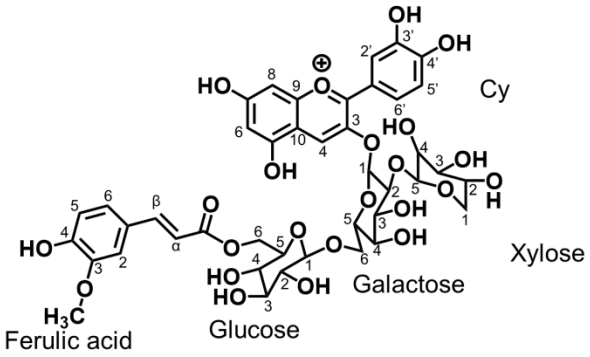

Table 2-2 (Continued)

Cy3XCGG		
	^{1}H NMR	
Position	**δ (ppm)**	**Multiplicity (Hz)**
Cy (aglycon)		
H-4	8.538	s
H-6	6.665	d (2.1)
H-8	6.592	d (1.4)
H-2'	7.953	d (2.4)
H-5'	7.091	d (8.5)
H-6'	8.091	dd (2.1, 8.5)
Galactose		
H-1	5.349	d (7.2)
H-2	4.221	dd (3.3, 9.0)
H-3	4.179	dd (~2, *n.d.*)
H-4	3.948	dd (2.9, *n.d.*)
H-5	4.466	*n.d.*
H-6A	*n.d.*	*n.d.*
H-6B	3.772	*n.d.*
Glucose		
H-1	4.492	*n.d.*
H-2	3.477	dd (~3, *n.d.*)
H-3	3.482	*n.d.*
H-4	3.729	d (2.9)
H-5	3.484	ddd (*n.d.*)
H-6A	5.288	dd (1.3, 5.0)
H-6B	4.167	dd (6.3, *n.d.*)
Xylose		
H-1	*n.d.*	*n.d.*
H-2	*n.d.*	*n.d.*
H-3	3.347	dd (3.1, *n.d.*)
H-4	3.432	ddd (~2, 6.9, 9.0)
H-5A	3.504	*n.d.*
H-5B	2.810	*n.d.*
Coumaric aicd		
H-2	6.972	d (8.2)
H-3	6.390	d (2.3)
H-5	6.390	d (2.5)
H-6	6.961	*n.d.*
H-7	7.350	d (15.8)
H-8	6.186	d (15.9)

n.d.: Not detected

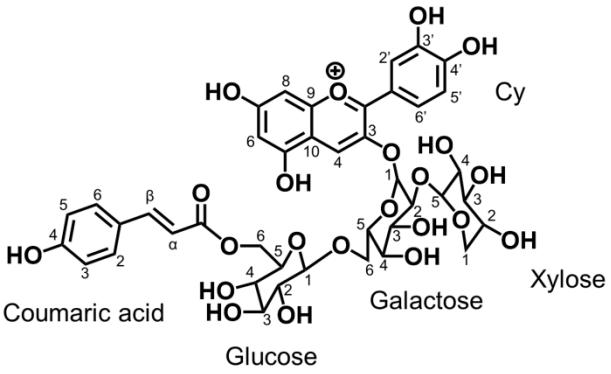

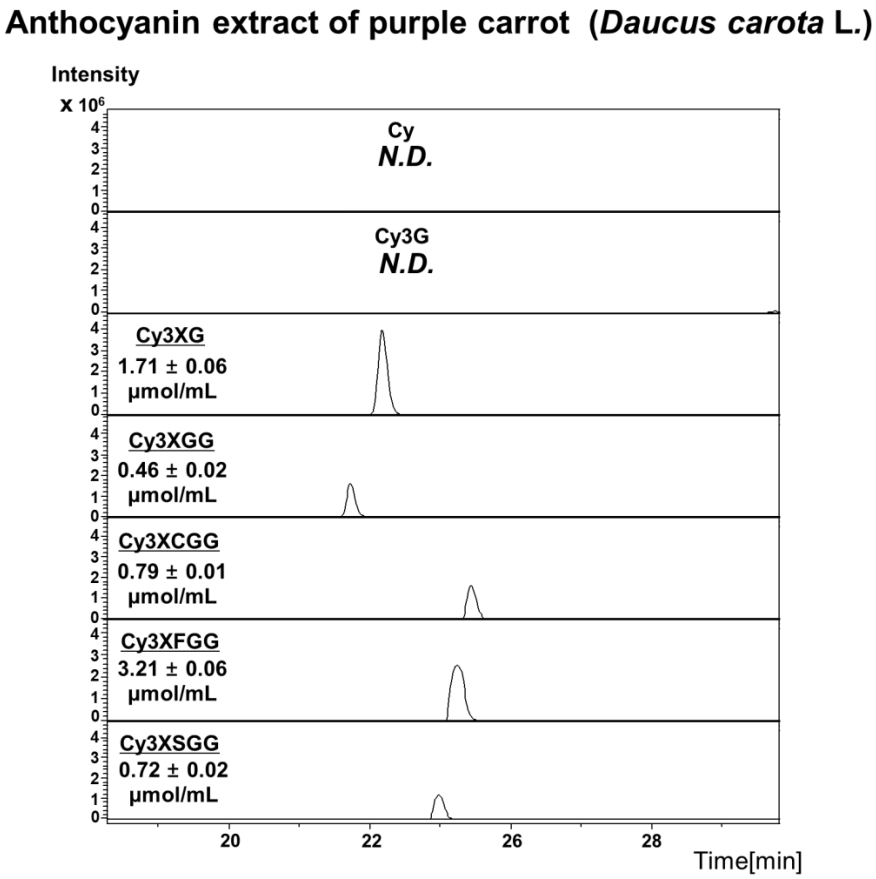

Figure 2-1 LC-MS chromatograms of anthocyanins of purple carrot extract (*Daucus carota* L., 1 mg/mL) by LC-TOF/MS

Each chromatogram shows the elution of the target anthocyanins ($[M]^+$: Cy = 287.0550 *m/z*; Cy3G = 449.1078 *m/z*; Cy3XG = 581.1501 *m/z*; Cy3XGG = 743.2029 *m/z*; Cy3XCGG = 889.2397 *m/z*; Cy3XFGG = 919.2503 *m/z*; Cy3XSGG = 949.2608 *m/z*). Numbers inserted in MS chromatograms indicate the concentration (pmol/mL) of anthocyanins in purple carrot extract (mean ± SEM, n = 3). *N.D.*: not detected.

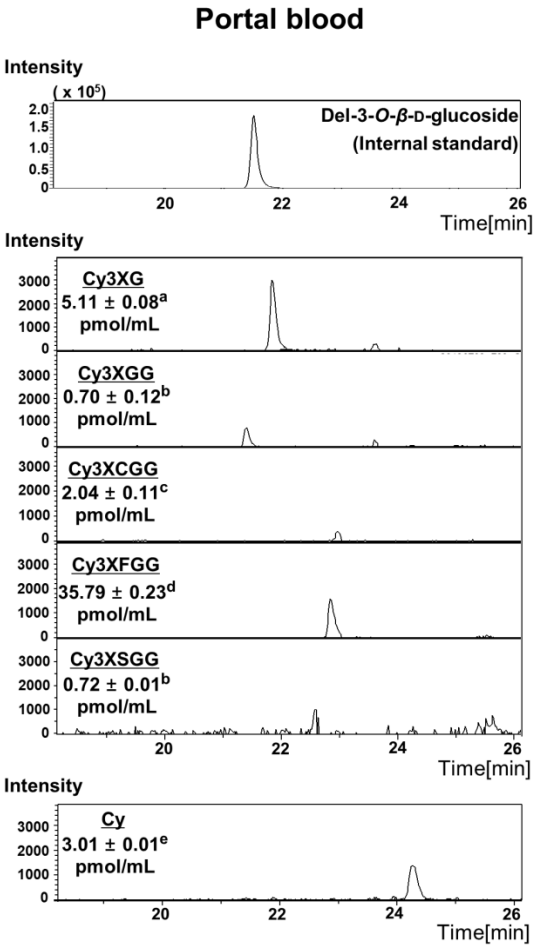

Figure 2-2 LC-MS chromatograms of anthocyanins via LC-TOF/MS in portal plasma of SD rats at 60 min after oral administration of the purple carrot extract (30 mg/kg)

Each chromatogram shows the elution of the target anthocyanins ($[M]^+$: Del-3-*O*-*β*-D-glucoside (an internal standard) = 465.1027 *m/z*; Cy = 287.0550 *m/z*; Cy3G = 449.1078 *m/z*; Cy3XG = 581.1501 *m/z*; Cy3XGG = 743.2029 *m/z*; Cy3XCGG = 889.2397 *m/z*; Cy3XFGG = 919.2503 *m/z*; Cy3XSGG = 949.2608 *m/z*). Numbers inserted in MS chromatograms indicate the concentration (pmol/mL) of anthocyanins in portal plasma (mean ± SEM, n = 3). Different superscript letters indicate significant difference ($P < 0.05$) between groups by Tukey-Kramer's *t*-test.

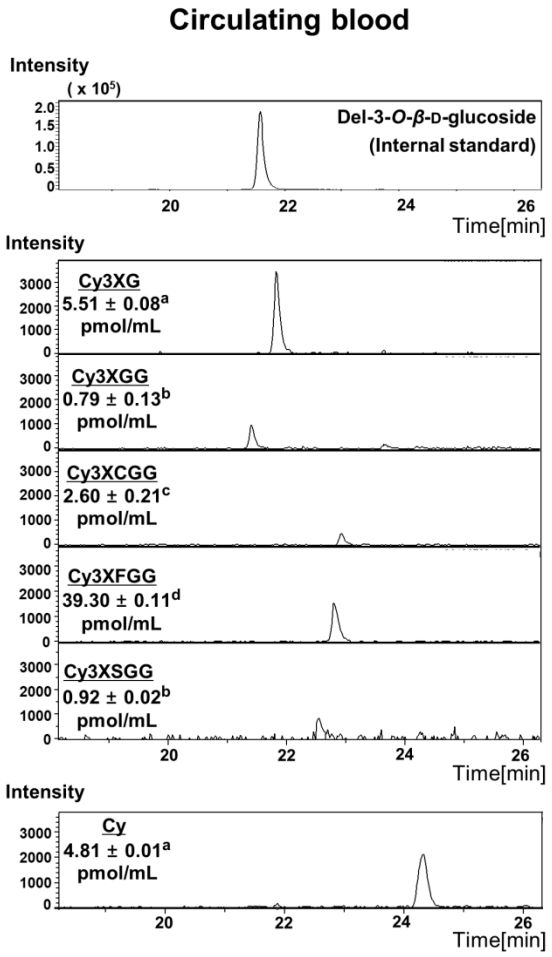

Figure 2-3 LC-MS chromatograms of anthocyanins via LC-TOF/MS in circulating plasma of SD rats at 60 min after oral administration of the purple carrot extract (30 mg/kg)

Each chromatogram shows the elution of the target anthocyanins ($[M]^+$: Del-3-*O*-*β*-D-glucoside (an internal standard) = 465.1027 *m/z*; Cy = 287.0550 *m/z*; Cy3G = 449.1078 *m/z*; Cy3XG = 581.1501 *m/z*; Cy3XGG = 743.2029 *m/z*; Cy3XCGG = 889.2397 *m/z*; Cy3XFGG = 919.2503 *m/z*; Cy3XSGG = 949.2608 *m/z*). Numbers inserted in MS chromatograms indicate the concentration (pmol/mL) of anthocyanins in circulating plasma (mean ± SEM, n = 3). Different superscript letters indicate significant difference ($P < 0.05$) between groups by Tukey-Kramer's *t*-test.

3.2. MALDI-MS imaging analysis of acylated anthocyanin transport across SD rat intestinal membranes

MALDI-MS imaging technique is a powerful analytical technique for direct visualization of targeted analytes in organs. Combinatorial transport experiments of the analytes with transport inhibitors allow for the prediction of absorption route by diminishing their visualized distribution and MS intensity in the intestinal tissue sections by MALD-MS imaging technique .[77] DHB matrix solution with phytic acid as a matrix additive can form homogeneous DHB matrix crystal formation, and exhibits reproducibility of MS intensity ($[M+H]^+$, 155.1 *m/z*; intensity of DHB: 2.61 ± 0.36 × 106, CV: 33.9%) on intestinal tissue sections (Figure 2-4), which can be utilized for semi-quantitative analysis of analytes in a visualization region by acquiring the relative MS intensity of matrix solution, DHB in MALDI-MS. The MALDI-MS imaging technique was also applied to investigate the transport pathways of bulky Cy3XFGG that can be absorbed into bloodstream (Figures 2-2 and 2-3). *In situ* transport experiments of acylated anthocyanin, Cy3XFGG, and its aglycon, Cy, were conducted in jejunum for 60 min of transport. Cy3G was also used as a typical non-acylated target that was known to be transported via GLUT2 in the intestine membrane.[16,91]

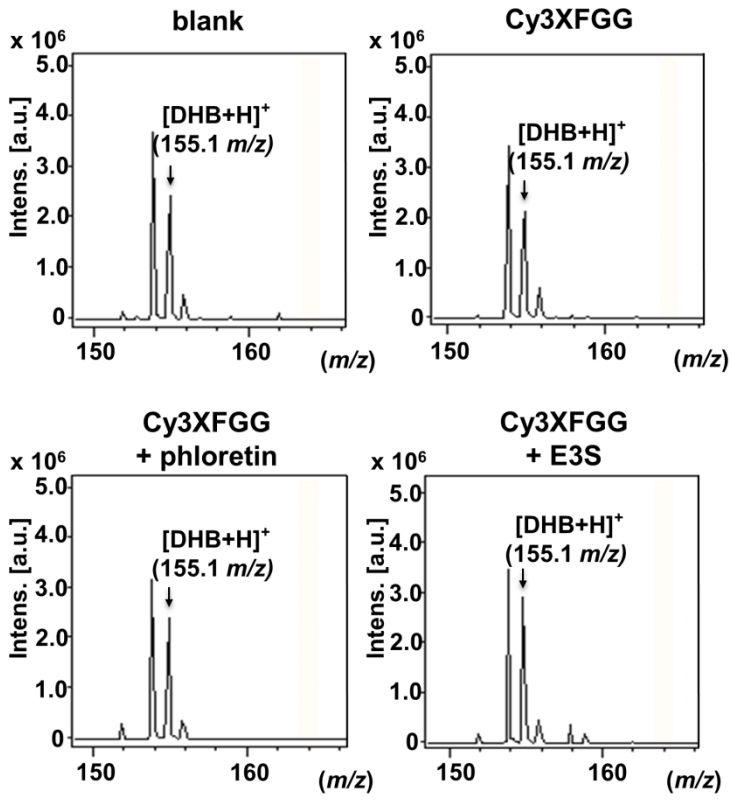

Figure 2-4 MALDI-MS spectra of DHB on jejunum membrane tissue sections after 60 min intestinal transport of Cy3XFGG with or without phloretin and E3S as the influx transporter inhibitors

DHB matrix solution with phytic acid as a matrix additive was used for MALDI-MS. Blank indicates the intestinal tissue section without intestinal transport of Cy3XFGG. The details of experimental conditions are described in "Materials and methods" section. Reproducibility of MS intensity of DHB ($[M+H]^+$, 155.1 *m/z*; intensity: 2.61 ± 0.36 × 106, CV: 33.9%) was acquired for 4 tissue sections of small intestine.

As shown in Figures 2-5, 2-6, 2-7, and 2-8, Cy3XFGG, as well as its aglycon (Cy) and Cy3G, was clearly visualized in jejunum tissue sections. Their intact transports were also further confirmed in the basolateral direction via LC-TOF/MS (Figure 2-9). LC-TOF/MS (>1 pmol/injection) and MALDI-MS imaging technique (>100 pmol/spot, Figure 2-10) have different detection sensitivity, but both showed that the Cy3XFGG can be incorporated and transported into the intestinal membrane in its intact form.

As can be seen in Figures 2-5, 2-6, and 2-7, inhibition of intestinal transport by phloretin and E3S caused the noticeable diminishment of MS intensity of Cy (Figures 2-5, 2-8, and 2-9) and Cy3G (Figures 2-6, 2-8, and 2-9) in the jejunum tissue section, indicating that these non-acylated anthocyanins were incorporated via both the OATP and GLUT2 routes. Alzaid et al. reported that Cy inhibited GLUT2-mediated glucose transport in Caco-2 cell monolayers.[91] Monoglycosylated anthocyanins, such as quercetin-4′-*O*-*β*-D-glucoside, quercetin-3-*O*-*β*-D-glucoside, and Cy-3-*O*-*β*-D-glucoside, can be reportedly absorbed via hexose transport routes like GLUT2.[16,41,92] Consistently, the present results exhibit that Cy3G and Cy in the jejunum tissue sections with 60 min of transport were diminished by the presence of phloretin as a GLUT2 inhibitor (Figures 2-5 and 2-6). In contrast, there was no change of appearance in the MS image and intensity for Cy3XFGG with phloretin, while OATP inhibition caused the noticeable diminishment of all MS images and intensities of acylated, glycosylated, as well as aglycon forms (Figures 2-7, 2-8, and 2-9). This strongly suggested that the OATP route involved in the incorporation process of acylated anthocyanin, Cy3XFGG, into the intestinal membrane, but not the GLUT2 route. The absence of an acylated moiety, including the feruloyl group, may be a crucial factor for intestinal GLUT2-mediated anthocyanins transport as there has been reported that the feruloyl moiety of arabinoxylan oligosaccharide inhibited its GLUT2-mediated transport in Caco-2 cell experiments.[93] In this study, although MALDI-MS detection could not accomplish

selective MS detection of diverse anthocyanin forms, such as quinoidal anion, carbinol flavylium cation, and chalcone psuedobases at physiological small intestine condition (pH 7.4) owing to the acidic condition by using 20 mM phytic acid in DHB matrix solution,[94,95] any targeted anthocyanins must be incorporated into the small intestinal membrane in their intact form. Considering the broad range substrate specificity of OATP route that can recognize anionic substrates,[52,96,97] it seems likely that the formation of quinoidal anion from flavylium cationic structure at around pH 6[94] (in the present study, pH 6.0) can cause readily transport of acylated anthocyanins, as well as other anthocyanins via OATP route.

In situ MALDI-MS imaging technique experiments using WOR as a transcytosis inhibitor[53] and CSA as an efflux ABC transporter inhibitor[54] also provided noteworthy information on the small intestinal transport mechanism of acylated anthocyanins with specific pathways. Inhibition of the transcytosis route was not involved in the intestinal transport of Cy3XFGG (Figure 2-11), while the inhibition of efflux pumps by CSA caused a noticeable increase in the MS image and intensity of Cy3XFGG (Figure 2-12). These results demonstrate that membrane-incorporated Cy3XFGG can be pumped out to the apical side via ABC transporter efflux routes.

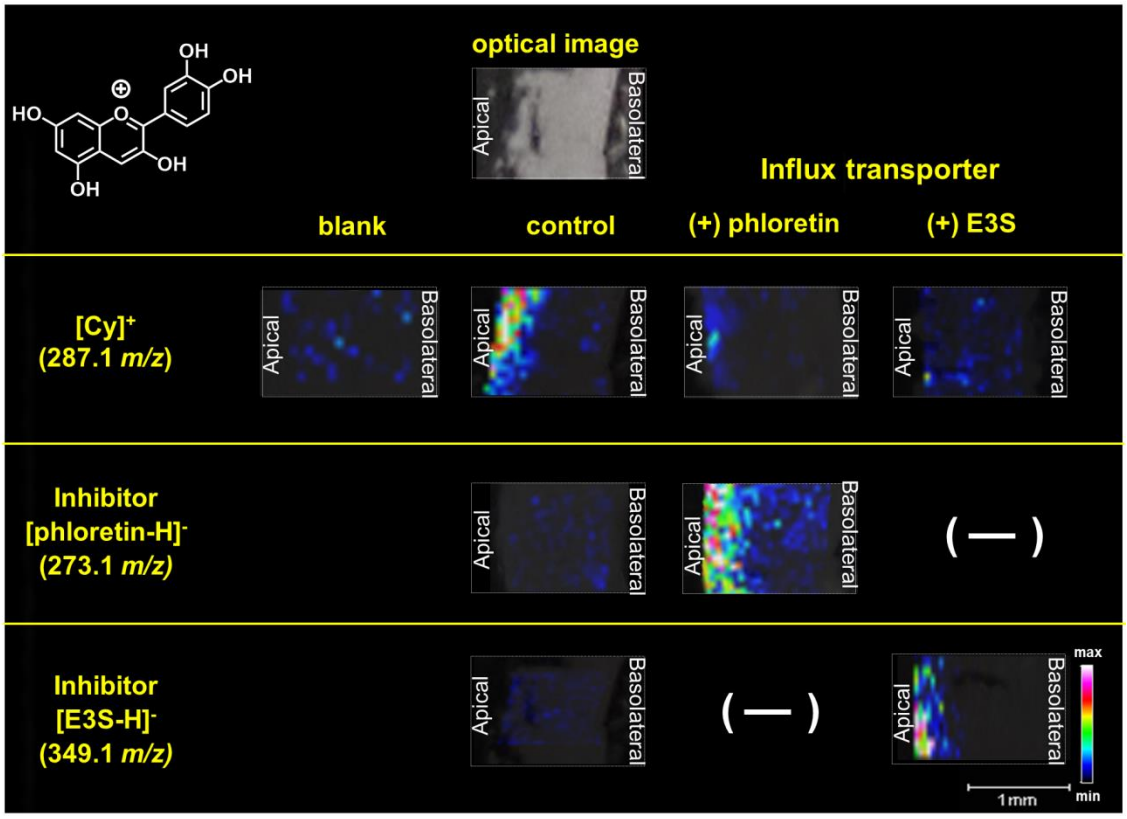

Figure 2-5 MALDI-MS imaging analysis of Cy distributed in rat jejunum membranes after 60 min intestinal transport experiments in the presence or absence of each transport inhibitor

Blank indicates the intestinal tissue section without intestinal transport of Cy. The concentration of Cy was 100 μM. Each MS image shows the spatial distribution of the Cy, phloretin, and E3S on the jejunum tissue section; $[Cy]^+$ (287.1 *m/z*) in positive ion mode, and $[phloretin-H]^-$ (273.1 *m/z*) and $[E3S-H]^-$ (349.1 *m/z*) in negative ion mode.

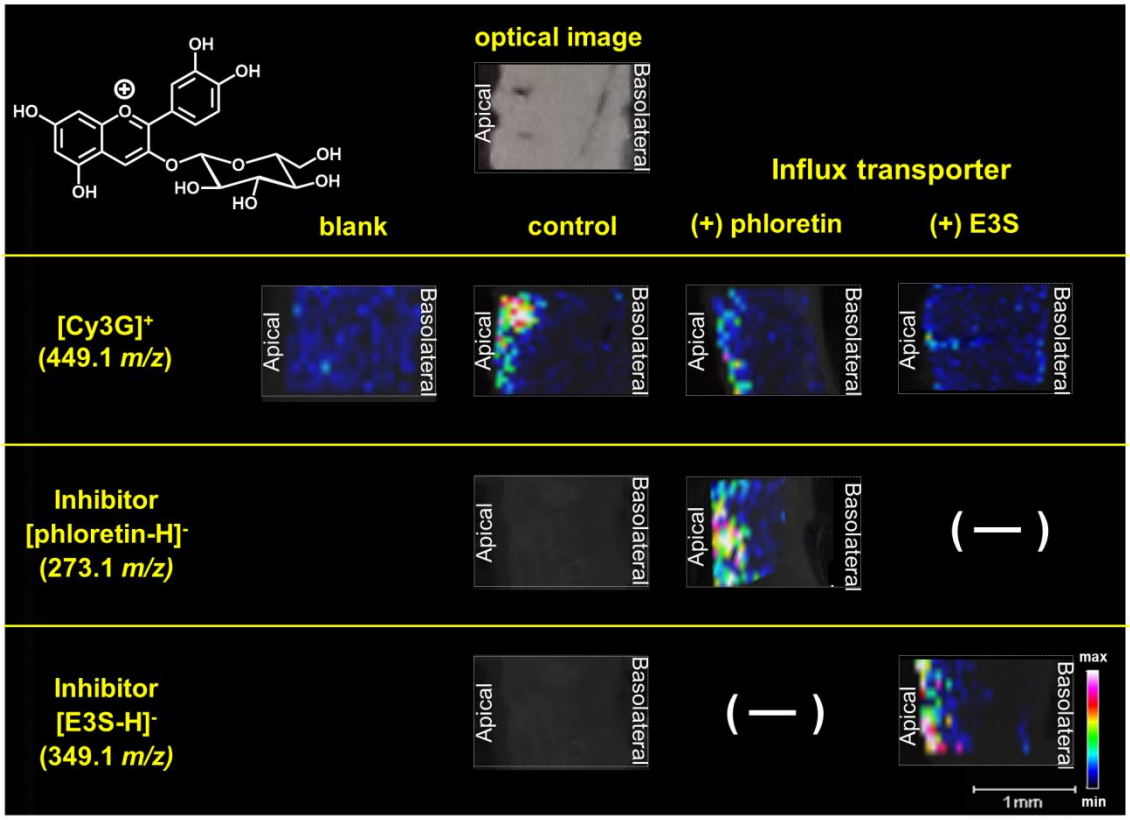

Figure 2-6 MALDI-MS imaging analysis of Cy3G distributed in rat jejunum membranes after 60 min intestinal transport experiments in the presence or absence of each transport inhibitor

Blank indicates the intestinal tissue section without intestinal transport of Cy3G. The concentration of Cy3G was 100 μM. Each MS image shows the spatial distribution of Cy3G, phloretin, and E3S on the jejunum tissue section; $[Cy3G]^+$ (449.1 *m/z*) in positive ion mode, and $[phloretin-H]^-$ (273.1 *m/z*) and $[E3S-H]^-$ (349.1 *m/z*) in negative ion mode.

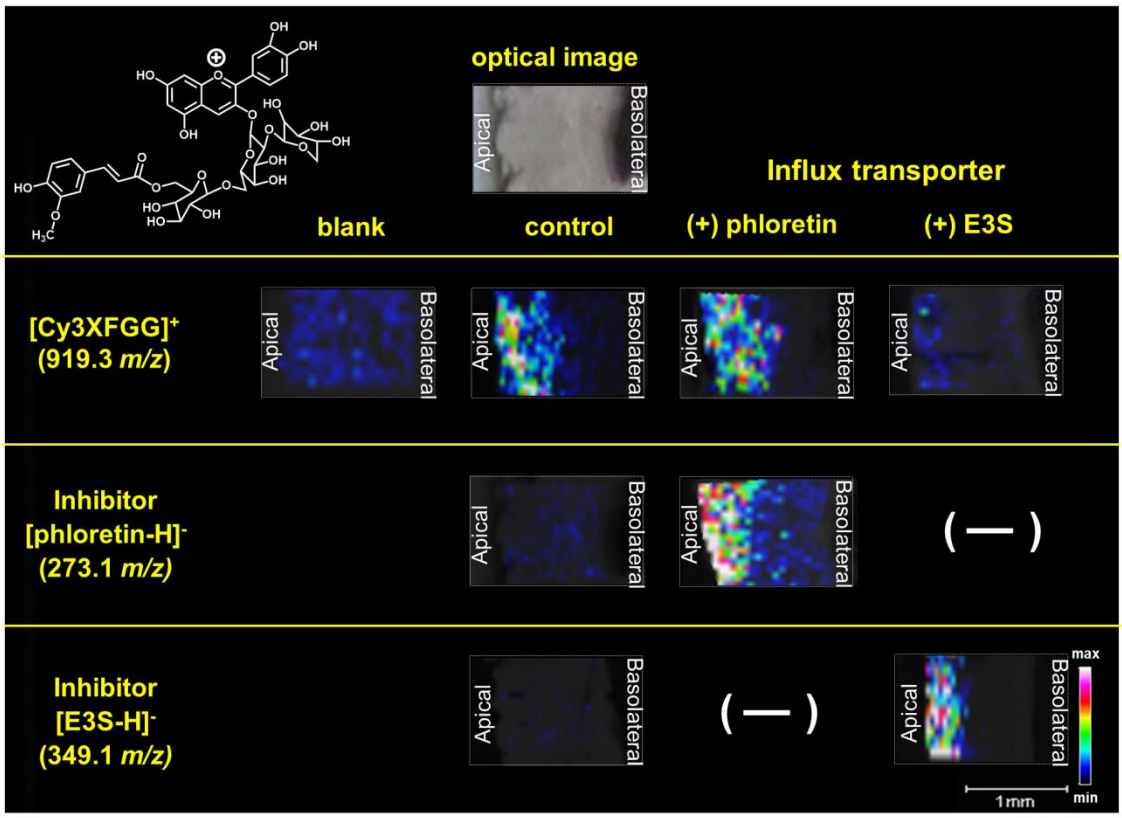

Figure 2-7 MALDI-MS imaging analysis of Cy3XFGG distributed in rat jejunum membranes after 60 min intestinal transport experiments in the presence or absence of each transport inhibitor

Blank indicates the intestinal tissue section without intestinal transport of Cy3XFGG. The concentration of Cy3XFGG was 100 μM. Each MS image shows the spatial distribution of the Cy3XFGG, phloretin, and E3S on the jejunum tissue section; $[Cy3XFGG]^+$ (919.3 *m/z*) in positive ion mode, and $[phloretin-H]^-$ (273.1 *m/z*) and $[E3S-H]^-$ (349.1 *m/z*) in negative ion mode.

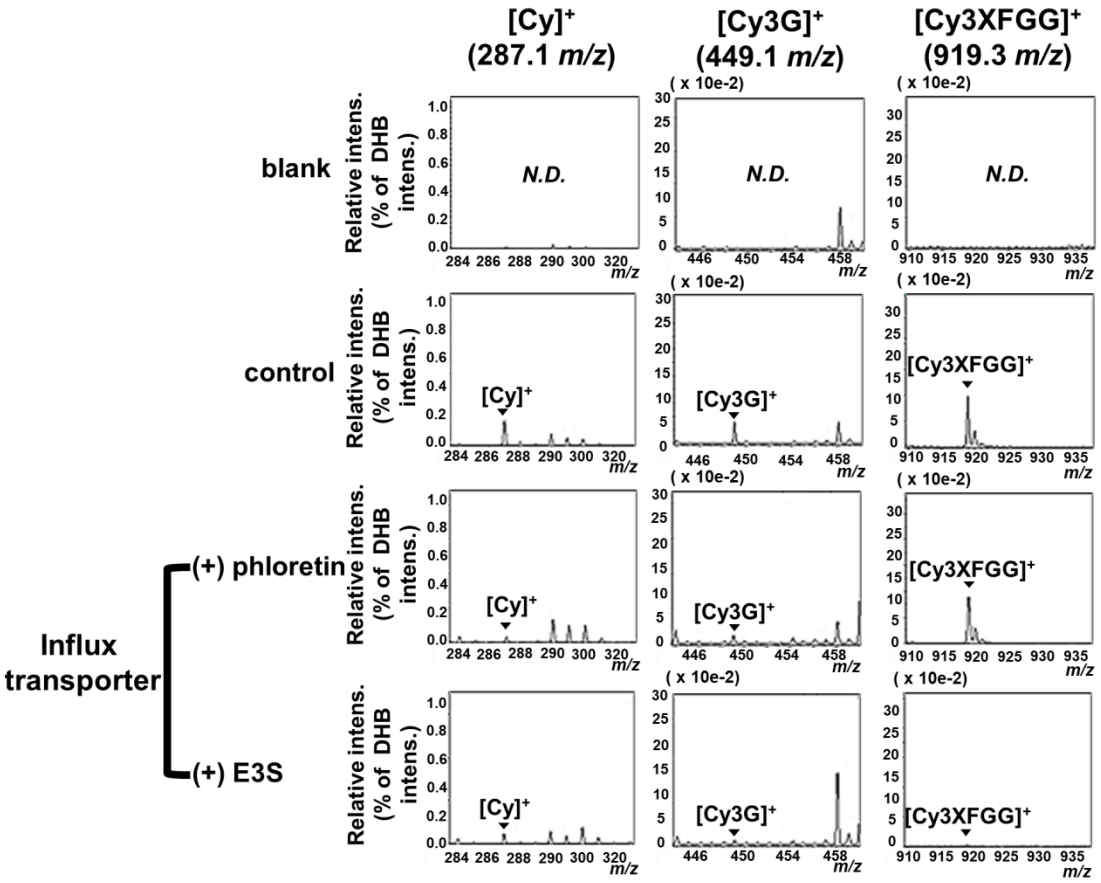

Figure 2-8 MALDI-MS spectra corresponding to visualized Cy, Cy3G, and Cy3XFGG in jejunum membranes after 60 min intestinal transport experiments in the presence or absence of each transport inhibitor shown in Figures 2-5, 2-6, and 2-7

The concentration of each anthocyanin in intestinal transport experiments was set at 100 μM. The spectrum of MALDI-MS is shown as a relative MS intensity of the analyte against MS intensity of DHB. *N.D.* indicates no MS detection.

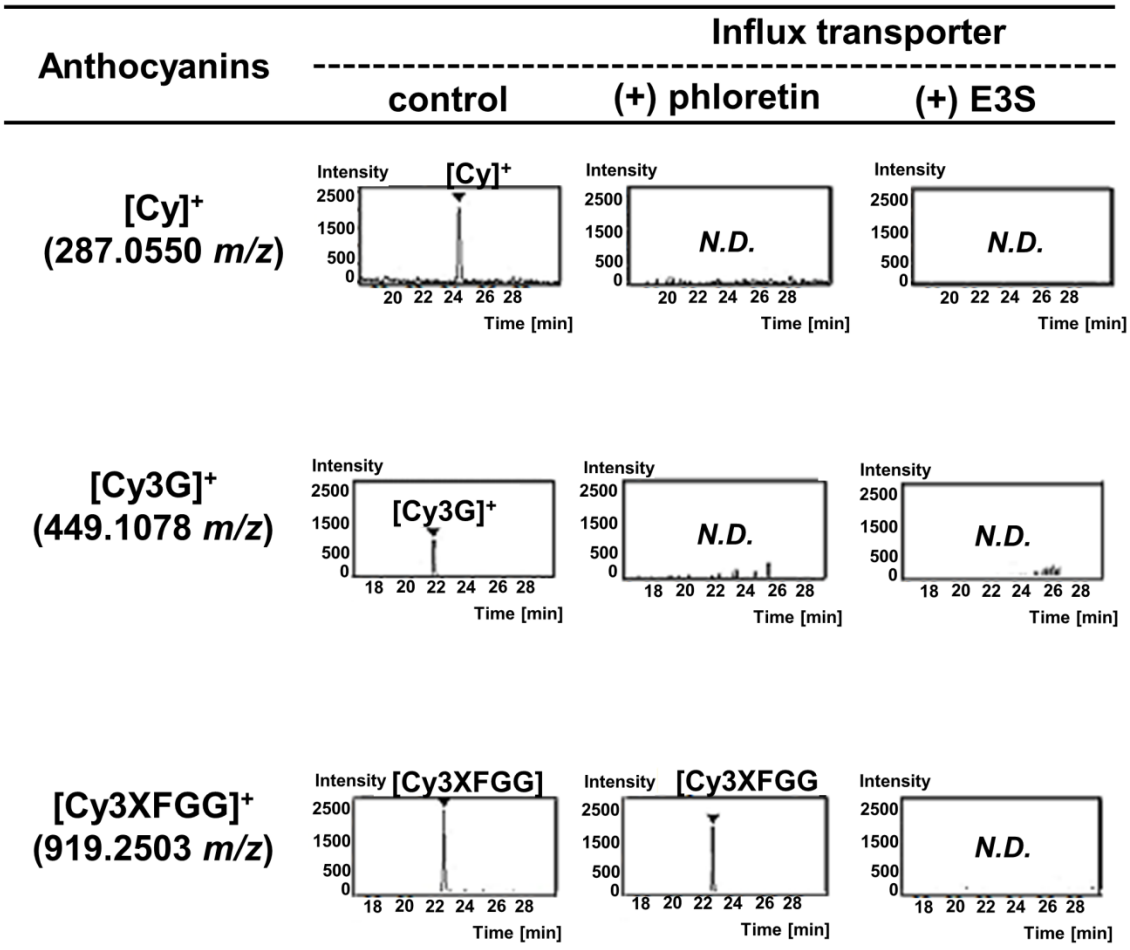

Figure 2-9 LC-MS chromatograms corresponding to Cy, Cy3G, and Cy3XFGG in basolateral solutions after 60-min intestinal transport experiments in the absence or presence of each influx transport inhibitor

The concentration of each anthocyanin in intestinal transport experiments was set at 100 μM. The corresponding extracted-ion chromatograms of $[Cy]^+$ (287.0550 *m/z*), $[Cy3G]^+$ (449.1078 *m/z*), and $[Cy3XFGG]^+$ (919.2503 m/z) in basolateral solutions were shown by LC-MS. *N.D.* indicates no MS detection.

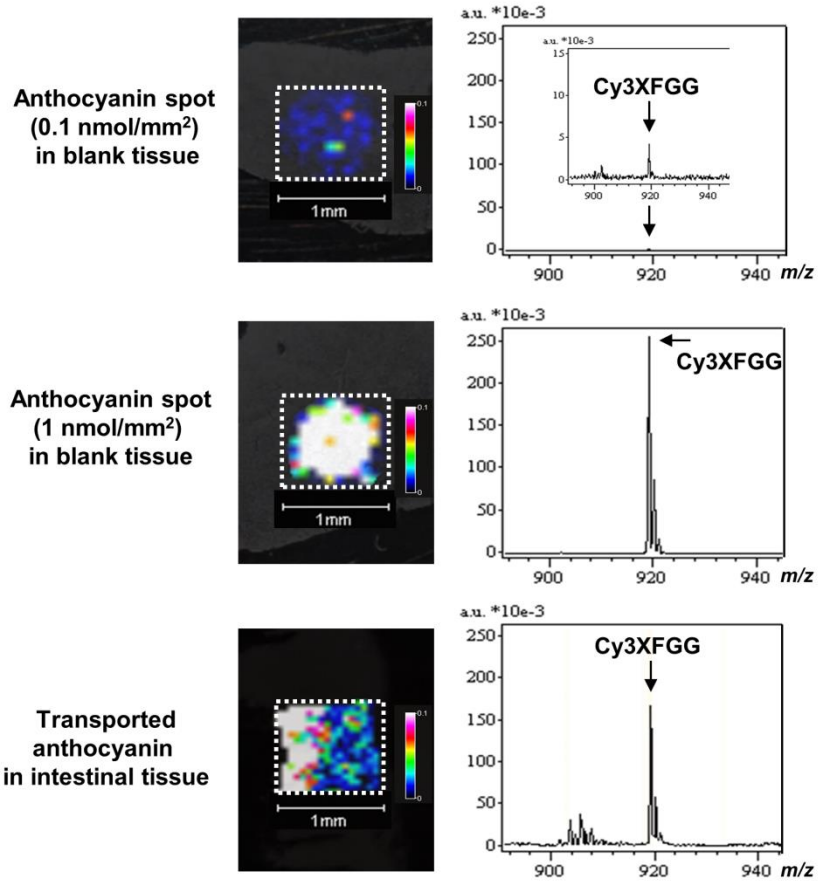

Figure 2-10 MALDI-MS detection of Cy3XFGG spots on the blank intestine tissue section at 0.1 and 1.0 nmol/mm^2

Measurement areas of MALDI-MS imaging technique are shown as white dotted area. MS images of 0.1 and 1.0 nmol/mm^2 of Cy3XFGG were acquired on the blank intestine tissue sections via MALDI-MS imaging technique. MALDI-MS also detected spatial distribution of the transported Cy3XFGG on the jejunum tissue section; $[Cy3XFGG]^+$ (919.3 *m/z*) in positive ion mode.

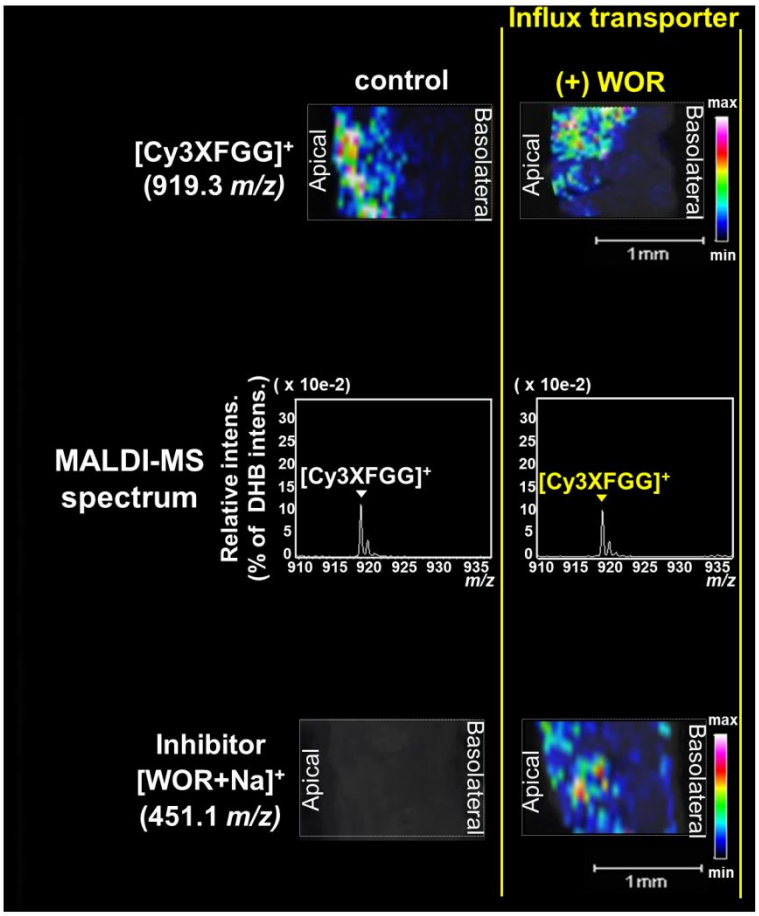

Figure 2-11 MALDI-MS imaging analysis of Cy3XFGG distributed in rat jejunum membrane sections after 60 min intestinal transport in the presence or absence of wortmannin (WOR, 1 μM)

The concentration of Cy3XFGG for the intestinal transport experiments was 100 μM. Each MS image shows the spatial distribution of Cy3XFGG ($[M]^+$, 919.3 *m/z*) and WOR ($[M+Na]^+$, 451.1 *m/z*) in the intestinal tissue section. The spectrum of MALDI-MS is shown as a relative MS intensity of target against DHB MS intensity.

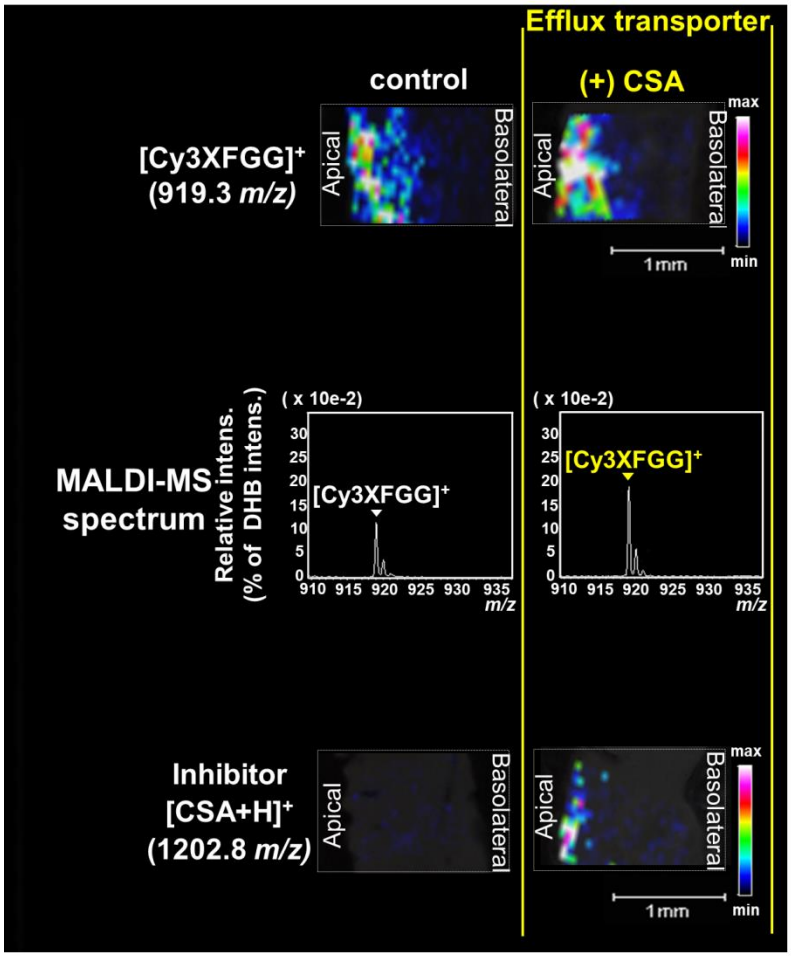

Figure 2-12 MALDI-MS imaging analysis of Cy3XFGG distributed in rat jejunum membrane sections after 60 min intestinal transport in the presence or absence of an efflux transport inhibitor, cyclosporine A (CSA, 20 μM)

The concentration of Cy3XFGG for the intestinal transport experiments was 100 μM. Each MS image shows the localization of Cy3XFGG ($[M]^+$, 919.3 *m/z*) and CSA ($[M+H]^+$, 1202.8 *m/z*) in the intestinal section. The spectrum of MALDI-MS is shown as a relative MS intensity of target against DHB MS intensity.

3.3. Metabolic behavior of acylated anthocyanins in SD rat intestinal transport

Figures 2-13 and 2-14 visually show detection result of phase I enzymatic degradation products and phase II metabolites of Cy3XFGG via MALDI-MS imaging technique, respectively. MS images for $[Cy3XGG]^+$ (743.2 *m/z*), $[Cy3GG]^+$ (611.2 *m/z*), $[Cy3XG]^+$ (581.2 *m/z*), [Cy3-galactoside]$^+$ (449.1 *m/z*, Cy3-Gal), and $[Cy]^+$ (287.1 *m/z*) are shown as degraded fragments from Cy3XFGG ($[M]^+$, 919.3 *m/z*) (Figure 2-13). MS images of Cy3XFGG-transported jejunum tissue sections exhibited that only Cy was visualized at the apical regions (Figuure 2-13), in agreement with detection of its aglycon form degraded from Cy-based anthocyanins in blood samples (Figures 2-2 and 2-3). In addition, there has been reported that monoglycosylated Cy, Cy3G, can undergo enzymatic hydrolysis to its aglycon, Cy,[92] following the methyl conjugation.[94,98] In this study, conjugated Cy3XFGG (glucuronidated, sulfated, methylated, and their combination forms) was not detected in the Cy3XFGG-transported intestine tissue sections, while methylated Cy was slightly visualized in the Cy- and Cy3XFGG-transported tissue setions (Figure 2-14). Although the possibility of production of other metabolites in the tissue section was not excluded, these MS images indicated that Cy3XFGG is stable against phase I/II metabolism during intestinal absorption process. In this study, LC-TOF/MS analysis also exhibited that Cy3XFGG was not degraded and was stable in the apical solution following the 60-min transport experiments (Figure 2-15).

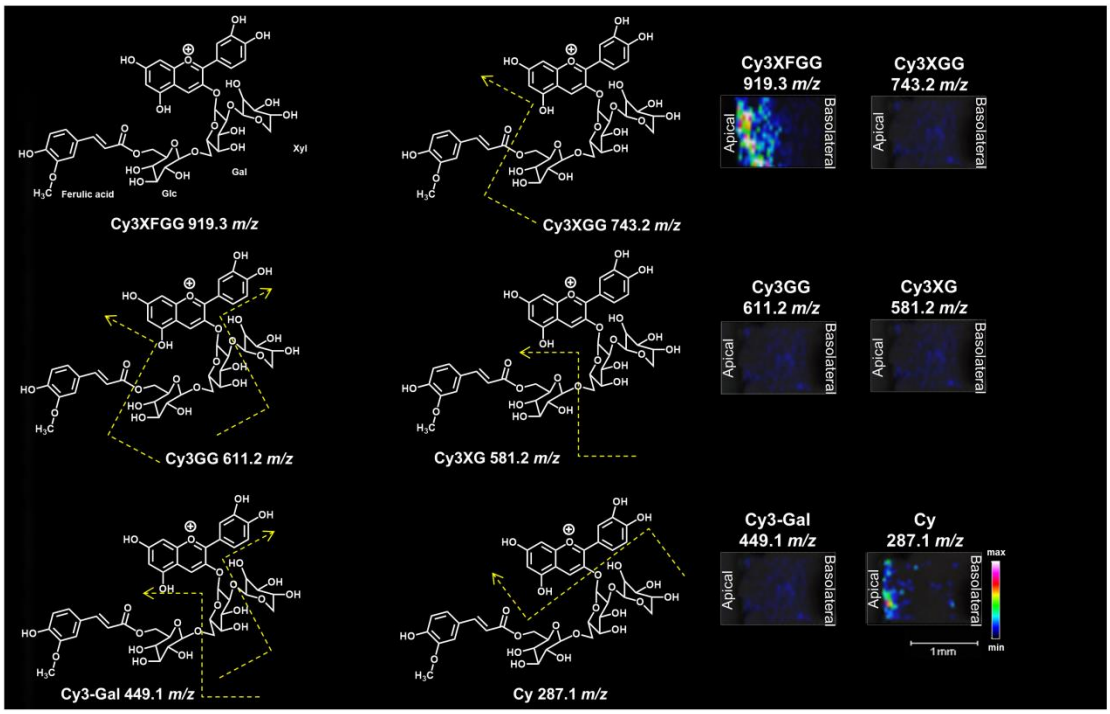

Figure 2-13 MALDI-MS imaging analysis of degraded metabolites from Cy3XFGG in rat jejunum membranes after 60 min intestinal transport

MS images of degraded metabolites of Cy3XFGG were acquired on the intestine tissue sections via MALDI-MS imaging technique in positive ion mode. Each MS image shows the spatial distribution of the targets on the intestinal tissue section; degraded metabolites of Cy3XFGG ($[M]^+$, 919.3 *m/z*): Cy3XGG ($[M]^+$, 743.2 *m/z*), Cy3GG ($[M]^+$, 611.2 *m/z*), Cy3XG ($[M]^+$, 581.2 *m/z*), Cy3-Gal ($[M]^+$, 449.1 *m/z*) and Cy ($[M]^+$, 287.1 *m/z*).

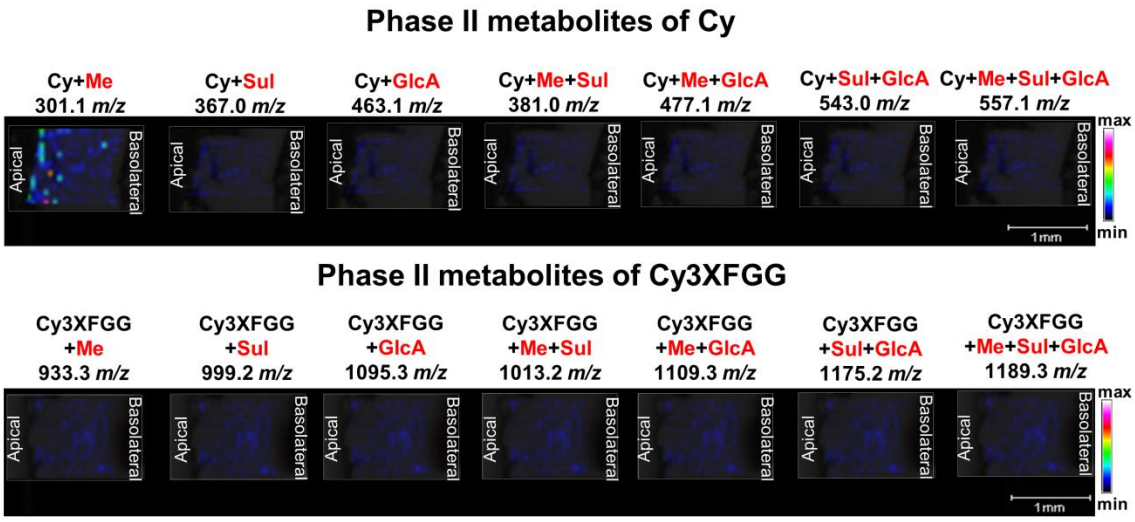

Figure 2-14 MALDI-MS imaging analysis of phase II metabolites of Cy and Cy3XFGG after 60 min intestinal transport in jejunum membranes

MS images of phase II metabolites of Cy and Cy3XFGG were acquired on the intestine tissue sections via MALDI-MS imaging technique in positive ion mode. Each MS image shows the spatial distribution of the target on the intestinal tissue section; Phase II metabolites of Cy: Cy + methyl (Me) ($[M]^+$,301.1 *m/z*), Cy + sulfate (Sul) ($[M]^+$, 367.0 *m/z*), Cy + glucuronide (GlcA), ($[M]^+$, 463.1 *m/z*), Cy + Me + Sul ($[M]^+$, 381.0 *m/z*), Cy + Me + GlcA ($[M]^+$, 477.1 *m/z*), Cy + Sul + GlcA ($[M]^+$, 543.0 *m/z*), Cy + Me + Sul + GlcA ($[M]^+$, 557.1 *m/z*), and metabolites of Cy3XFGG: Cy3XFGG + Me ($[M]^+$, 933.3 *m/z*), Cy3XFGG + Sul ($[M]^+$, 999.2 *m/z*), Cy3XFGG + GlcA ($[M]^+$, 1095.3 *m/z*), Cy3XFGG + Me + Sul ($[M]^+$, 1013.2 *m/z*), Cy3XFGG + Me + GlcA ($[M]^+$, 1109.3 *m/ z*), Cy3XFGG + Sul + GlcA ($[M]^+$, 1175.2 *m/z*), Cy3XFGG + Me + Sul + GlcA ($[M]^+$, 1189.3 *m/z*).

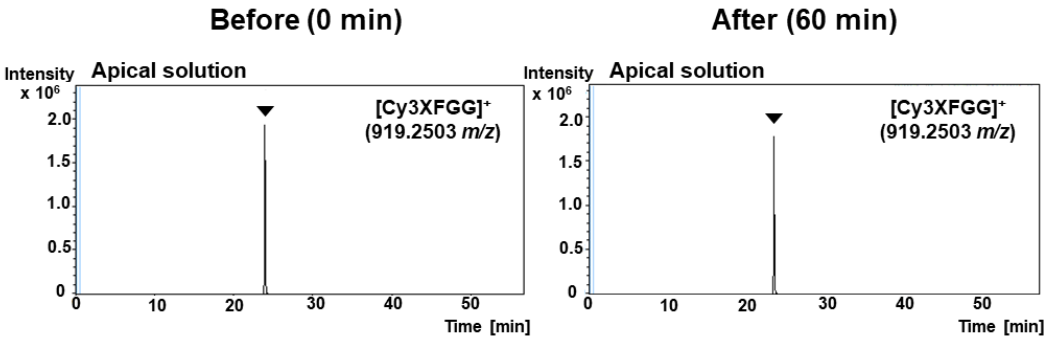

Figure 2-15 Extracted-ion chromatograms of Cy3XFGG via LC-TOF/MS in the apical solution before (0 min) and after (60 min) intestinal transport in rat jejunum membranes

Extracted-ion chromatograms of Cy3XFGG were acquired in the apical solution before (0 min) and after (60 min) intestinal transport via LC-MS in positive ion mode. Each chromatogram shows the elution of the target anthocyanin ($[M]^+$: Cy3XFGG = 919.2503 *m/z*)

4. Summary

In conclusion, **Chapter II** demonstrated for the first time that acylated anthocyanins can be incorporated and transported in their intact form with a relatively strong resistance against phase I/II metabolism. *In situ* MALDI-MS imaging technique provided the remarkable finding that the small intestinal transport of an acylated anthocyanin, Cy3XFGG, is confining for the OATP 2B1 route, while glycosylated anthocyanin form and its aglycon form are favorably transported via both the GLUT2 and OATP 2B1 transport routes (Figure 2-16). Taken together, acylated anthocyanins with anti-inflammatory,[29] hemodynamic,[30] and anti-oxidant effects[99] can be absorbed into the intestine via OATP 2B1.

These findings also prove that the MALDI-MS imaging technique is the outstanding tool to visually evaluate bioavailability such as accumulation, metabolism, and absorption of targeted bioactive food compounds. However, bioavailability evaluation using a conventional MALDI-MS system was only available for the acquisition of visual localization and qualitative information, excluding quantitative information. Therefore, a novel quantitative approach of MALDI-MS imaging technique in biological tissue sections, which allows not only quantification of tissue accumulated bioactive food compounds but also visualization of their spatial localization was investigated in the next **Chaper III**.

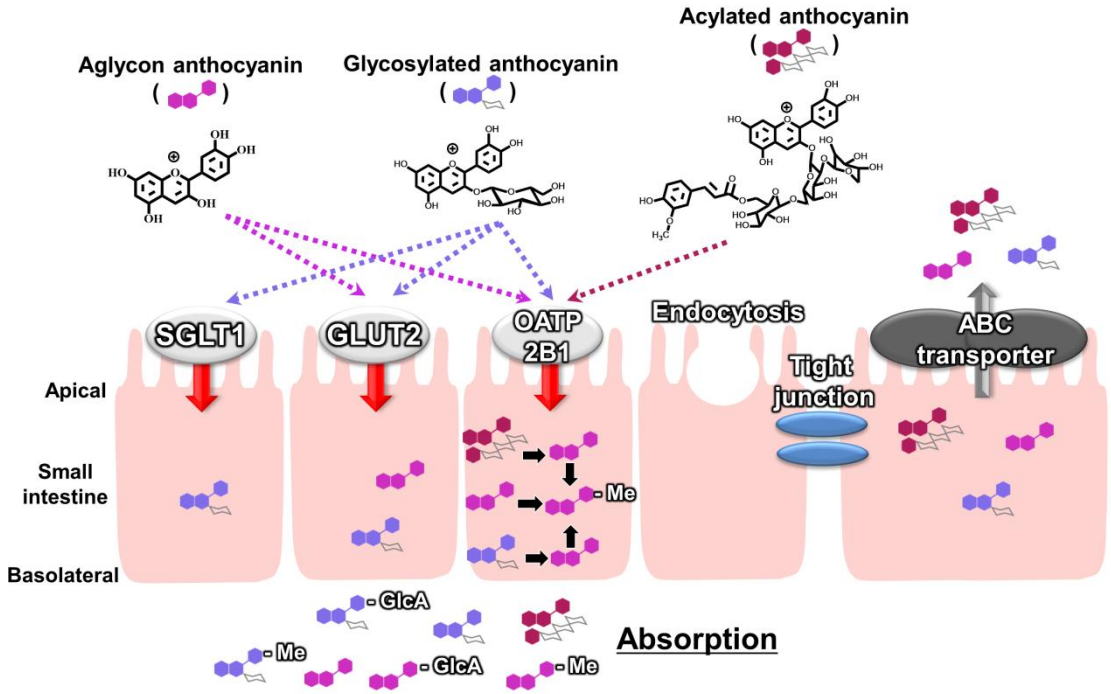

Figure 2-16. Graphic overview of intestinal absorption process of anthocyanins

OATP 2B1, organic anion transporting polypeptide 2B1; ABC transporter, ATP-binding cassette transporter; GLUT2, glucose transporter 2; and SGLT1, sodium-dependent glucose transporter 1; Me, methyl; GlcA, glucuronide.

Chapter III

Establishment of quantitative MALDI-MS imaging technique for tissue accumulation of anthocyanin-related compounds

1. Introduction

As mentioned in **Chapter I** and **Chapter II**, the explication of absorption mechanisms is indispensable for verifying the nutritional properties and functionalities of food compounds. The absorption process of food compounds into the blood circulatory system, as well as tissue accumulation, must be considered. However, analytic methods for precisely analyzing the microenvironments in organs are still lacking and requiring.[77] Therefore, it is essential to establish an analytic method that can topically and quantitatively visualize the tissue accumulation of absorbed bioactive compounds, including their metabolites, in aimed organs.

MALDI-MS imaging technique has been used in various fields, such as food science,[100-102] medical science,[103] pharmacology,[104,105] and plant physiology,[106] because it can visualize the localization and distribution of MS detectable compounds in organs without using specific labels, such as antibodies. Nonetheless MALDI-MS imaging technique has the lack of quantitative property. The factors that affect directly quantitative performance of MALDI-MS imaging technique have included the extraction efficiency of analyte molecules,[107] inhomogeneity of tissue sections,

matrix-to-analyte ratio,[108] heterogeneous matrix crystallization on the tissue section,[109] variation of MALDI laser intensity,[110] ion suppression from tissue section,[111] etc. In particular, the inhomogeneity of matrix crystal formation and low-level reproducibility during analytical runs[78] are crucial issues to be solved for the enhancement of the quantification capability of MALDI-MS. Thus, analytic methods with high-level reproducibility, such as LC–MS systems, generally using an IS which is detectable to compensate the analytic fluctuation, are preferred in quantification of analytes.[112] Otherwise, MALDI-MS imaging technique, which has exhibited considerable advantages of maintaining the form of biological tissues, as well as simplifying the processing of samples,[113] can be a indispensable analytical technique in several scientific fields if the aimed analytes can be visually and precisely quantified. However, the inhomogeneity of the matrix crystals, as well as the fluctuation in the matrix spray amount on the tissue sections,[114-116] is a crucial issue to the quantitative capability of MALDI-MS imaging technique. Thus, the regulation of constant matrix spraying, as well as the nondestructive evaluation of the amount of matrix spray before MALDI laser irradiation, may extremely improve the quantitative capability.

Although quantitative MALDI-MS (qMALDI-MS) methods utilizing robotic matrix spotters[104,117,118] which exhibit small fluctuation in the matrix amount, have been developed, a crucial limitation persists with regard to the distance (>250 μm) between the spots. This limitation significantly affects the resolution of MS image or imaging quality. Furthermore, the inhomogeneity of matrix crystal formation is a critical factor that diminishes the imaging resolution of MALDI-MS.[78-81,120] Although robotic or automatic matrix sprayers have been evolved to achieve reproducible matrix spraying,[119] the homogeneity of the matrix crystal formation, its amount, and distribution on the biological tissue sections cannot be controlled and monitored.

Thus, **Chapter III** focus on establishing a novel quantitative method for MALDI-MS imaging technique by utilizing MS ionizable fluorescent and crystal-homogenizing substances as the additives to matrix solution, allowing the nondestructive monitoring of matrix spray amount and improving the homogeneity of the matrix crystals. The fluorescent substance added to matrix solution could behave as both an index to control the amount of the matrix sprayed prior to MALDI laser irradiation and a MS normalizing standard to enable compensation of the MS intensity variability of analytes owing to the heterogenous matrix crystallization and ion suppression from tissue sections (Figure 3-1). Ferulic acid (FCA), a representative absorbable metabolite of acylated anthocyanins as visualized in **Chapter II**, possessing various physiological benefits such as anticancer activities[121−123] was applied to the qMALDI-MS imaging technique to validate its quantification capability by correlating it with capability of LC-MS in negative-ion detection mode. Nifedipine, an oral antihypertensive agent that can accumulate in organs following oral administration,[124-126] was also subjected to the qMALDI-MS imaging technique in positive-ion detection mode.

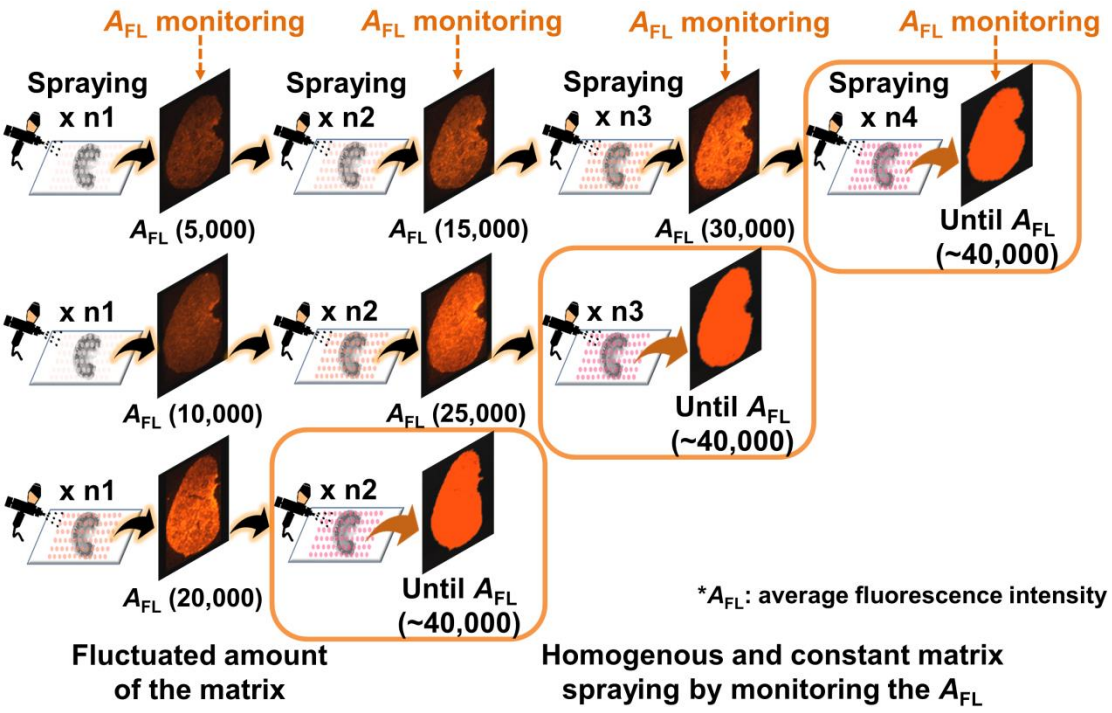

Figure 3-1 Scheme of the fluorescence-assisted matrix-spraying method

The matrix solution containing the fluorescent IS was homogeneously sprayed onto the kidney tissue sections. The homogeneity of the matrix crystal was significantly enhanced by adding a matrix additive. The average fluorescence intensity (A_{FL}) of the fluorescent IS that was sprayed on the tissue sections was measured using the Fusion SOLO.7S.EDGE system (a convenient and quick fluorescent imager) at every number of spray cycles, either 1 or 5 cycles, until the desired A_{FL} (~40,000) was acquired.

2. Materials and methods

2.1. Materials

O-Dinitrobenzene (*O*-DNB) was obtained from Nacalai Tesque Co. (Kyoto, Japan). nitrobenzene and α-Cyano-4-hydroxycinnamic acid (CHCA) were obtained from Wako Pure Chemical Industries Ltd. (Osaka, Japan). Sevoflurane was purchased from Maruishi Pharmaceutical Co., Ltd. (Osaka, Japan). Furthermore, DHB, quercetin, rhodamine 6G (R6G), 6-carboxyfluorescein, nifedipine, ferulic acid (FCA), and aniline were purchased from Sigma-Aldrich Co. (St. Louis, MO, USA). Additionally, 1,5-diaminonaphthalene (1,5-DAN) and 7-methoxycoumarin-3-carboxylic acid were purchased from Tokyo Chemical Industry Co., Ltd. (Tokyo, Japan). Naphthalene was obtained from Kanto Chemical Co., Inc. (Tokyo, Japan). All the reagents, which were of analytical grade, were used without further purification.

2.2. Animal experiments

Male 8-week-old SD rats (268.7 ± 3.9 g, SPF/VAF Crj; Charles River, Kanagawa, Japan) were used for the present study. The SD rats were acclimated under the following conditions: light, 12 h period (from 8:00 am to 8:00 pm); humidity, 55 ± 5%; and temperature, 21 ± 1 ℃. After 16 h of fasting, the FCA (dose = 50 mg/kg) was administered orally to SD rats. Afterward, the SD rats were sacrificed by exsanguination from the abdominal aorta during induction of anesthesia via volatile anesthetic agents, sevoflurane. Their kidneys were collected at 0, 15, 30, and 60 min following the oral administration. The residual blood in the organs was washed out by perfusion from their left ventricles using an ice-cold pH 7.0 phosphate-buffered saline solution (100 mL) to focus on the tissue-accumulated FCA except for the blood-accumulated ones. Thereafter,

the kidney was dissected and immediately stored at −80 °C until the analyses. All the animal experiments were carried out conforming to the Guidelines for Animal Experiments in the Faculty of Agriculture in the Graduate Course of Kyushu University and according to the law (no. 105, 1973) and notification (no. 6, 1980 of the Prime Minister's Office) of the Japanese Government. All the experiments were reviewed and approved by the Animal Care and Use Committee of Kyushu University (permit number: A20-095).

2.3. Fluorescence measurement

First, R6G, 7-methoxycoumarin-3-carboxylic acid, 6-carboxyfluorescein, and naphthalene were dissolved in 70% ACN. Each fluorescent substance (0.01−1 mM, 2−200 pmol/spot) was spotted onto tissue sections of blank kidney. The fluorescence images of the spotted substances were acquired using the Fusion SOLO.7S.EDGE system (Vilber-Lourmat, Marne-la-Vallée, France) consisting of blue (excitation/emission ($\lambda_{ex}/\lambda_{em}$) = 480/536 nm), green (excitation/emission ($\lambda_{ex}/\lambda_{em}$) = 530/595 nm), and red filters (excitation/emission ($\lambda_{ex}/\lambda_{em}$) = 640/750 nm). The image capture condition was set at a detection time of 1.8 s. As MALDI imaging technique is performed on-tissue area, the A_{FL} was calculated from the regions on the kidney tissue sections was used to control and monitor the sprayed matrix amount.

2.4. Preparation of tissue samples for MALDI-MS imaging technique

The frozen kidneys were sliced into 12 μm thick tissue sections using a CryoStar NX70 (Thermo Scientific, MA, USA) at −25 °C. The kidney sections were collected sequentially for MALDI-MS imaging technique and LC-MS to compare the quantitative capabilities of the two analytic systems. The tissue samples were thaw-mounted onto an ITO-coated conductive glass slide (Bruker Daltonics) and immediately dried under the

flow of nitrogen gas for qMALDI-MS imaging technique. ImagePrep (automatic matrix sprayer) was used to spray the matrix solution containing R6G (40 μg/mL), *O*-DNB (10 mg/mL), and 1,5-DAN (10 mg/mL) in 70% ACN, over the tissue sections onto the ITO glass slide in accordance with the following spraying conditions: spraying time 1.5 s; spraying cycles, 20−60; spray power, 20%; modulation, 20%; incubation time, 10 s; and drying time, 60 s. The A_{FL} of sprayed R6G as the fluorescent IS on the kidney tissue sections was measured using the Fusion SOLO.7S.EDGE system which was equipped with the green fluorescence filter, at every 1−5 cycles consecutively to regulate further matrix spraying (until the desired fluorescence intensity was obtained) to gain a constant matrix amount between the kidney tissue sections, as shown in Figure 3-1. The A_{FL} of kidney tissue sections was calculated by dividing the sum of fluorescence intensity that was acquired from the kidney tissue via the number of pixels acquired in the corresponding whole tissue area on the ITO-coated glass slide. The optical images of microscopy were captured on ITO-coated glass slide at 40−100× resolutions using an Eclipse Ts2-FL microscope (Nikon Corporation, Tokyo, Japan) before and after matrix spraying.

2.5. Quantitative MALDI-MS imaging analysis

The matrix-sprayed kidney tissue sections were analyzed using an Autoflex III MALDI-TOF/MS that was equipped with a SmartBeam (Bruker Daltonics) at 100 μm spatial resolution. The kidney tissue sections were subjected to qMALDI-MS imaging analysis in both the positive- and negative-ion detection modes using the following MALDI-MS parameters: the number of shots per pixel, 100; lens voltage, 7.50 kV; gain, 12.00; laser power, 39%; laser frequency, 200 Hz; range, 20%; offset, 59%; laser focus range, 100%; value, 6.0%; and ion source 1, 20.00 kV; ion source 2, 18.80 kV. The MS image data were reconstituted for visualization of spatial distribution with a mass

filtering of ± 0.2 *m/z* using Flex imaging software (version 2.1, Bruker Daltonics, Bremen, Germany). The obtained MS spectra were analyzed using Flexanalysis software (version 3.3, Bruker Daltonics, Bremen, Germany) as the sum of all the MS spectra obtained in the MS-imaging region. The average MS intensity was calculated as the sum of the MS spectra that were exported from the region of interest (ROI) divided by the number of pixels obtained in the ROI (100 pixels/mm^2). Calibration curves were constructed by plotting the average MS intensity ratio of FCA (2−300 pmol/0.2 μL spot) or nifedipine (2−160 pmol/0.2 μL spot) to R6G, which was calculated with MS spectra from the ROI covering the whole sample spot area (4 mm^2). The weight of the kidney tissue section (12 μm) was 430 μg/section, as calculated from the sum of weights of three sequential kidney tissue sections. The whole area of the kidney tissue sections was measured based on the number of pixels obtained on the kidney tissue section (204 ± 2 mm^2/kidney section = 20,411 ± 215 pixel/ kidney section) using Flex imaging software, which provided the density of kidney tissue section as mol/g dry tissue, to calculate the amount of FCA accumulated in the kidney tissue. The limit of detection (LOD) and limit of quantification (LOQ) were calculated respectively in accordance with the equations that were reported by Sammour et al.[115]

2.6. LC-TOF/MS analysis

The kidney tissue sections of the FCA-administered SD rats were immediately lyophilized and mashed using a BioMasher II (Nippi. Inc., Tokyo, Japan). The mashed powder of five sequential kidney tissue sections (~1.5 mg), which was adjacent to that for qMALDI-MS imaging technique, was homogenized with 0.1% FA and 500 μL of 50% MeOH containing 100 μL of 3,4-dimethoxycinnamic acid (DMCA, 1 μmol/L) as an IS using a Polytron homogenizer (20,000 rpm for 30 s × 3 times at 4 ℃; KINEMATICA AG; Luzern, Switzerland). The homogenate was subjected to sonication using a

SONIFIRE 250 (Branson Ultrasonics, Emerson Japan Co., Kanagawa, Japan) at an output control of 3 for 10 s × 3 times at 4 ℃. After centrifuging for 15 min at 4 ℃ and 14,000 × *g*, the supernatant was ultrafiltered using the Amicon® Ultra-0.5 mL centrifugal filter 3kDa centrifugal filter (Millipore, Carrigtwohill, Ireland) for 30 min at 4 ℃ and 14,000 × *g*. The obtained filtrate was evaporated, and the dried filtrate was subsequently dissolved in 100 μL of a 0.1% FA solution. Afterward, an aliquot (20 μL) of the solution was subjected to LC- TOF/MS analysis. LC-TOF/MS analysis was carried out, as described in the previous report.[101] LC separation was performed using an Agilent 1200 series system (Agilent, Waldbronn, Germany) on a Cosmosil 5C 18 AR-II column (particle size, 5 μm; 2.0 mm I.D. × 150 mm; Nacalai Tesque, Kyoto, Japan) with a linear gradient elution of ACN (0−100% for 20 min) containing 0.1% FA at a flow rate of 0.2 mL/min at 40 ℃. ESI-TOF/MS analysis was conducted using a microTOF II instrument (Bruker Daltonics) in the negative ion mode. The conditions of ESI-TOF/MS were as follows: the drying nitrogen (N_2) gas was used at a mass range of 100−1000 *m/z,* a drying temperature of 200 ℃, a flow rate of 8.0 L/min, a capillary voltage of 3800 V, and a nebulizing gas pressure of 1.6 bar. Acquisition and analyses of all data were performed using Bruker Data Analysis 3.2 software. The MS calibration solution containing 10 mM of sodium formate in 50% ACN was injected at the process of initiating of each analytical run of ESI-TOF/MS, and all the MS spectra were internally calibrated. To quantify the amount of FCA, a calibration curve of FCA, which was acquired from the blank kidney sections under the aforementioned MS conditions, was used: $y = 0.0994x + 7.6448$ ($R^2 = 0.9904$) [y is the peak intensity ratio (the observed MS intensity of the analyte to that of IS) and x is the concentration of FCA (6−600 nmol/g dry tissue).

3. Results and discussion

3.1. Establishment of fluorescence-assisted spraying method

The fluctuation of the spray amount of the matrix, as well as the inhomogeneity of the matrix crystal formation on the tissue section, were serious issues to the quantitative capability of MALDI-MS imaging technique.[78,111,112] Thus, the present study examined the applicability of a fluorescence substance as an IS to compensate for the fluctuation in the spray amount of the matrix between the measurements or tissue sections. A FUSION imaging system (simple fluorescent imager) was used in this study to ensure convenient and quick fluorescent image and intensity monitoring. As fluorescent ISs, compounds containing naphthalene ($\lambda_{ex}/\lambda_{em}$ = 290/330 nm), coumarin ($\lambda_{ex}/\lambda_{em}$ = 355/405 nm), fluorescein ($\lambda_{ex}/\lambda_{em}$ = 490/520 nm), and rhodamine ($\lambda_{ex}/\lambda_{em}$ = 530/550 nm) as their fluorophores were used for the fluorophore screening to determine the quantities of IS on the tissue section surfaces. R6G was certainly monitored on the kidney tissue sections (Figure 3-2) via fluorescence imaging technique using a green filter ($\lambda_{ex}/\lambda_{em}$ = 530/595 nm), while significant autofluorescence background, which hindered the fluorescence detections of other fluorescent substances, such as 6-carboxyfluorescein, naphthalene, and coumarin, by the blue ($\lambda_{ex}/\lambda_{em}$ = 480/536 nm) or red ($\lambda_{ex}/\lambda_{em}$ = 640/750 nm) filters, from the tissues, was observed. Furthermore, R6G was detected by MALDI-MS in both the negative- and positive-ion modes using 1,5-DAN as the matrix (Figure 3-3).

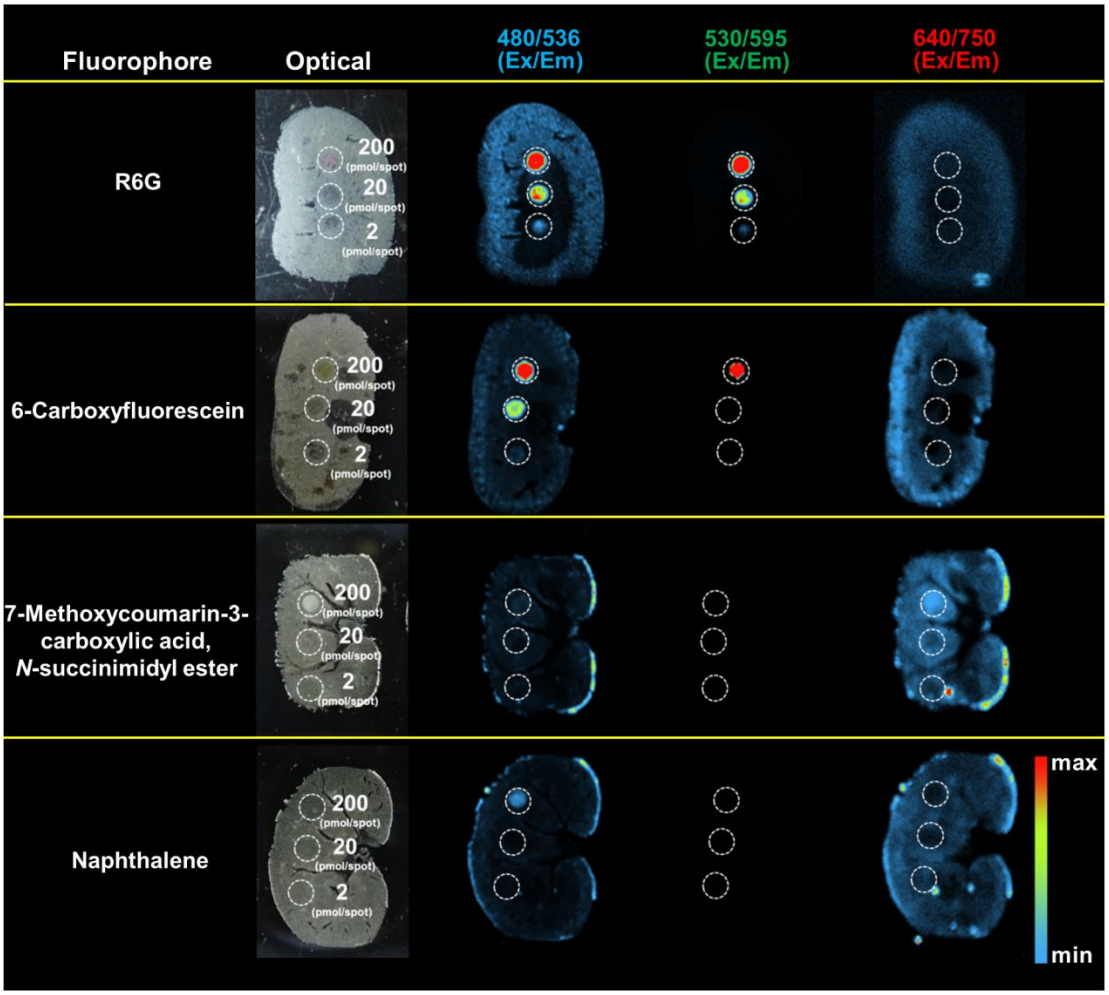

Figure 3-2 Fluorescent images of fluorescent IS candidates on tissue section

Each fluorescent IS candidate (2−200 pmol/0.2 μL spot) was spotted onto kidney tissue sections. Fluorescent images of R6G, 6-carboxyfluorescein, 7-methoxycoumarin-3-carboxylic acid-*N*-succinimidyl ester, and naphthalene were acquired by the fluorescent imager consisting of the blue (excitation/emission ($\lambda_{ex}/\lambda_{em}$) = 480/536 nm) and red filters (excitation/emission ($\lambda_{ex}/\lambda_{em}$) = 640/750 nm).

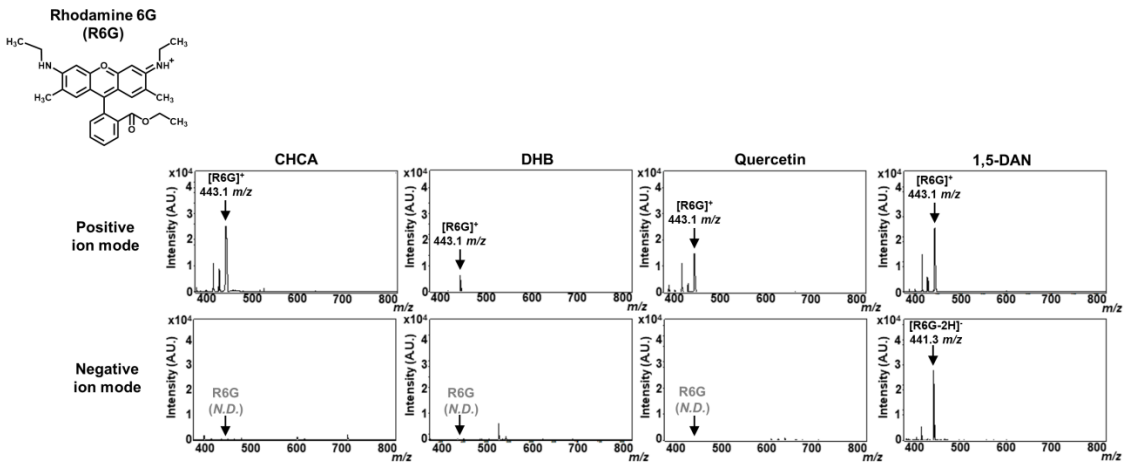

Figure 3-3 MALDI-MS analysis of R6G using four different matrix solutions

R6G was analyzed via MALDI-MS in the positive and negative detection modes using CHCA, DHB, quercetin, and 1,5-DAN. R6G (20 pmol/0.2 μL spot) was spotted with each matrix (10 mg/mL) onto the ITO-coated glass slide and subjected to MALDI-MS.

Although R6G has been known to be ionized in the positive-ion-mode LDI-MS without the matrix and to be employed as a matrix reagent for the negative-ion-mode MALDI-MS,[127−130] its detected intensity without the 1,5-DAN matrix was almost negligible in this experimental set-up (at 0.04 mg/mL) of R6G when compared to that in MALDI-MS with 1,5-DAN (19-fold higher intensity, Figure 3-4). Owing to the linear correlation coefficient between the MS and fluorescence intensities of R6G (R^2 = 0.9441, Figure 3-5), these results demonstrate that the fluorescent IS of R6G is a new MS-detectable index for assessing the matrix amount. Furthermore, since the crystal fineness and homogeneity of the matrix[78,131−134] are also key to ameliorating the tissue spatial resolution of MALDI-MS imaging technique,[134−136] some attempts at ameliorating the homogeneity of matrixes via matrix additives have been reported. For instance, aniline, which can form ionic bonds with CHCA, formed fine CHCA crystals.[101] In the present study, Figure 3-6 shows that *O*-DNB and nitrobenzene, but not aniline, at a concentration of 10 mg/mL among examined concentrations (0–10 mg/mL) in the matrix solution (1,5-DAN, 10 mg/mL) seemed to enhance the homogeneity of the matrix crystal formation. Moreover, the addition of *O*-DNB, not nitrobenzene, clearly enhanced the fineness and homogeneity of the matrix crystals of sprayed 1,5-DAN matrix (average matrix crystal diameter of sprayed droplets, 1,5-DAN only: 72 μm, nitrobenzene: 54 μm, *O*-DNB: 25 μm) (Figure 3-7). Compounds possessing nitro groups could be crystallized in compact crystal sizes and structures by strong and tight N–H•••O hydrogen bonds regarding the amino group.[137-139] Based on these findings, the optimized concentration of *O*-DNB (10 mg/mL) in the solution of the 1,5-DAN matrix (10 mg/mL), which exhibited the most homogeneous and finest matrix crystals, was used for the subsequent experiments.

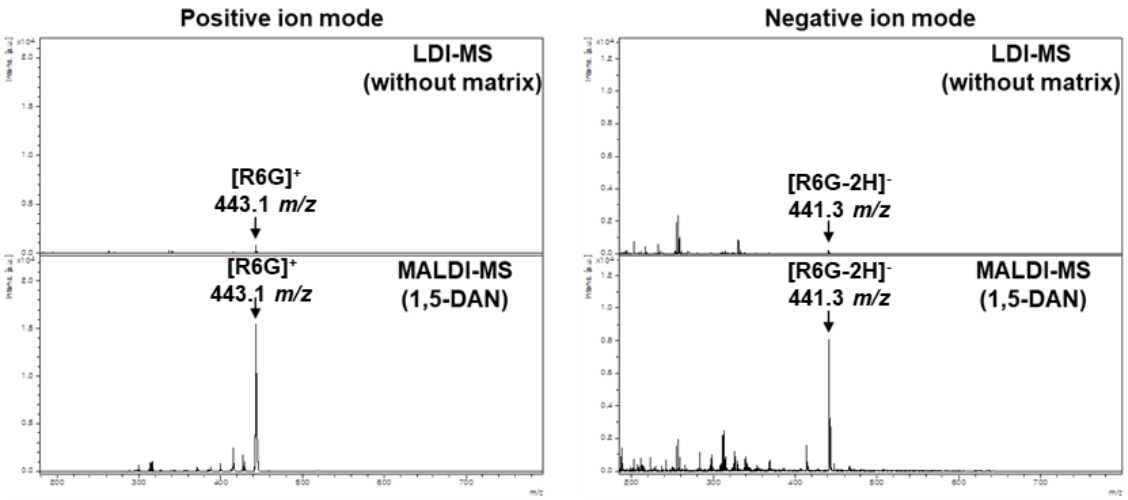

Figure 3-4 MS spectra of R6G via LDI-MS analysis with or without 1,5-DAN matrix solution in positive and negative ion modes

R6G was analyzed via MALDI-MS and LDI-MS with or without 1,5-DAN matrix solution (10 mg/mL) in the positive and negative detection modes. R6G (20 pmol/0.2 μL spot) was spotted with or without 1,5-DAN (10 mg/mL) onto the ITO-coated glass slide.

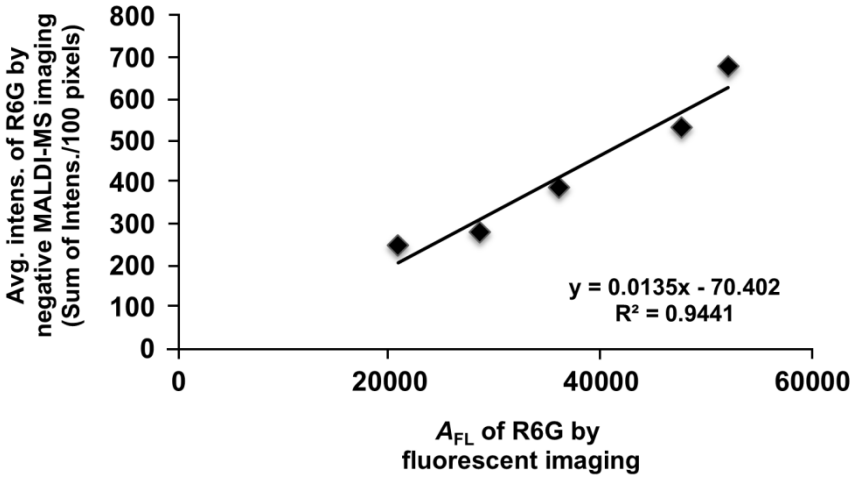

Figure 3-5 Linear correlation between fluorescent intensity and MS intensity of R6G sprayed on rat kidney tissue sections

1,5-DAN (10 mg/mL) matrix solution containing R6G (40 μg/mL) and *O*-DNB (10 mg/mL) was sprayed onto the blank kidney sections in a range of 20,000–60,000 of average fluorescent intensity. The fluorescent and MS intensities of R6G extracted from the sprayed area of kidney tissue sections were calculated as average intensity [sum of the spectra/the number of pixels in the ROI].

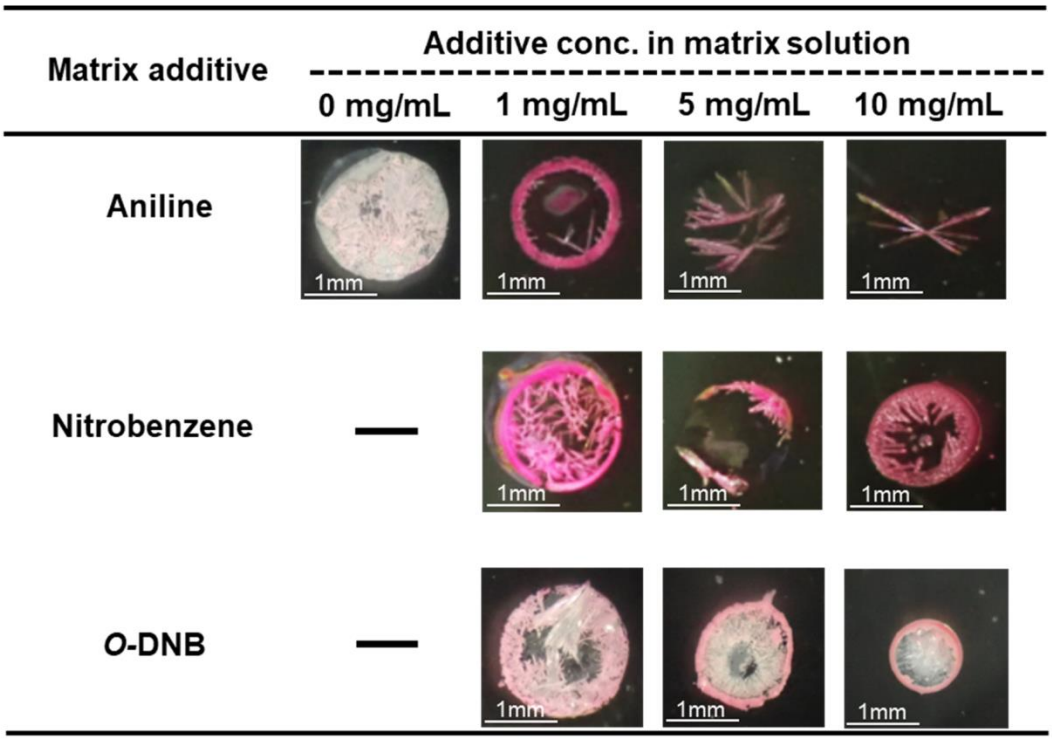

Figure 3-6 Optimization of the concentration of matrix additives (such as aniline, nitrobenzene, and *O*-DNB) for the matrix crystal formation of a homogeneous crystal with 1,5-DAN

The matrix crystal of the 1,5-DAN solution (10 mg/mL) containing R6G (0.04 mg/mL) and each additive (0–10 mg/mL) was formed by spotting a 0.2 μL volume onto the ITO-coated conductive glass slide. The optical images were acquired using an Eclipse Ts2-FL microscope with 40× resolution.

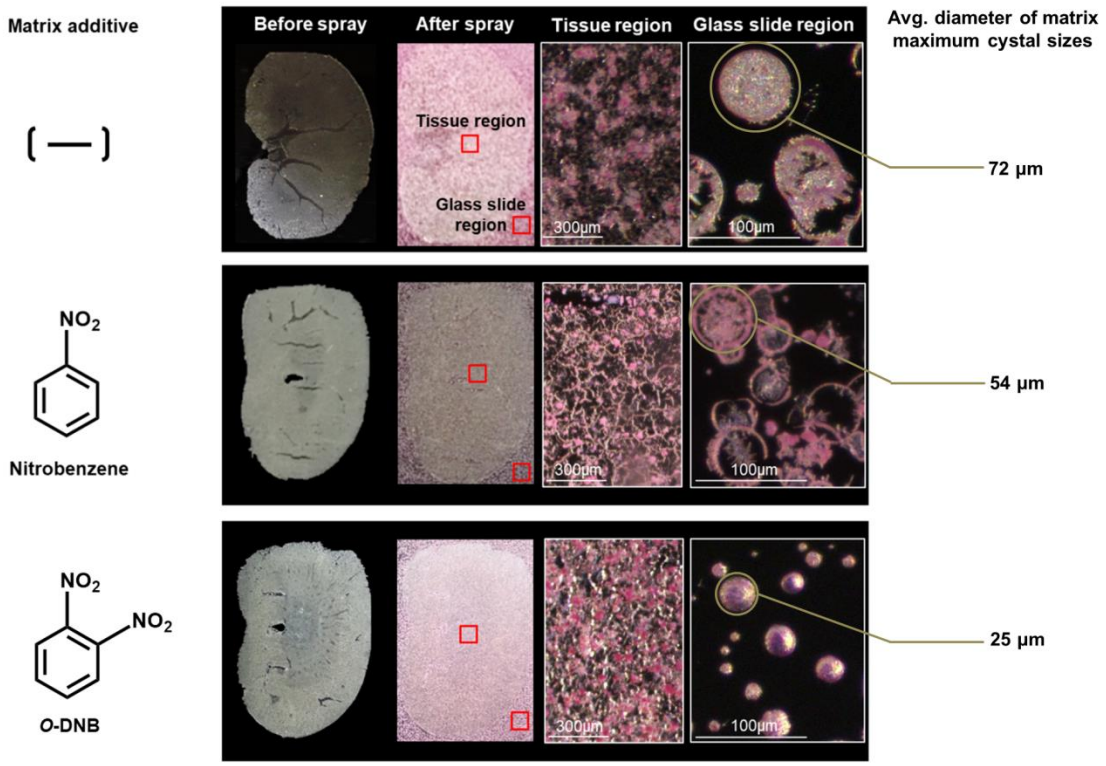

Figure 3-7 Matrix crystals of the 1,5-DAN solution containing different additives sprayed on rat kidney tissue sections

1,5-DAN solution containing R6G and a matrix additive (nitrobenzene or *O*-DNB) was sprayed to cover the kidney tissue sections until the desired fluorescent intensity (~40,000). The optical images before and after the matrix spraying were acquired by an optical microscope with 40× and 100× resolutions from the kidney tissue section and glass-slide regions, respectively. The average diameters of matrix crystals were calculated from the largest crystal among five randomly selected crystals on ITO-coated conductive glass slide.

Figure 3-8 shows the fluorescent images and intensities of the R6G after spraying. The calculated value of average fluorescent intensity was acquired from the kidney tissue regions among the whole sprayed regions shown in Figure 3-9, as MALDI-MS imaging technique was performed on kidney tissue. It was demonstrated that the fluorescent intensity fluctuated remarkably between the kidney tissue sections (RSD of A_{FL} = 15.3%), even though similar optical sprayed tissue images were obtained by 40 cycles of conventional fixed matrix spraying for the three kidney tissue sections which were sprayed with the 1,5-DAN matrix solution containing the R6G. Under the varying matrix conditions, the relative MS intensity of FCA to R6G also fluctuated in negative ion mode (RSD = 31.1%). Intriguingly, when the fluctuating matrix spray amounts on the kidney tissue sections were controlled until the desired fluorescent intensity (~40,000) was accomplished based on fluorescent monitoring every 1–5 matrix spraying cycles, a constant matrix spraying amount (RSD of the A_{FL}= 1.3%) in which the reproducibility for the relative MS detection of FCA was significantly enhanced (RSD = 3.1%). The linear improvement of MS intensity of FCA by the increasing matrix spraying amount (fluorescent intensity of R6G) positively proves the importance of constant and homogeneous matrix spraying amount in improving the reproducibility (Figure 3-10). Moreover, Figure 3-11 exhibits that the fine crystal formation by *O*-DNB also enhanced the reproducibility of the relative MS intensities of the nifedipine and FCA in the positive and negative ion modes (n = 5).

According to this result, in this study, R6G would be defined as spraying IS to behave as both a MS normalizing standard and an index of the matrix amount. Thus, the fluorescence-assisted reproducible matrix formation by a nondestructive monitoring matrix spraying amount before MALDI laser irradiation allowed the reproducible MS intensities of the analytes between different analytical measurements.

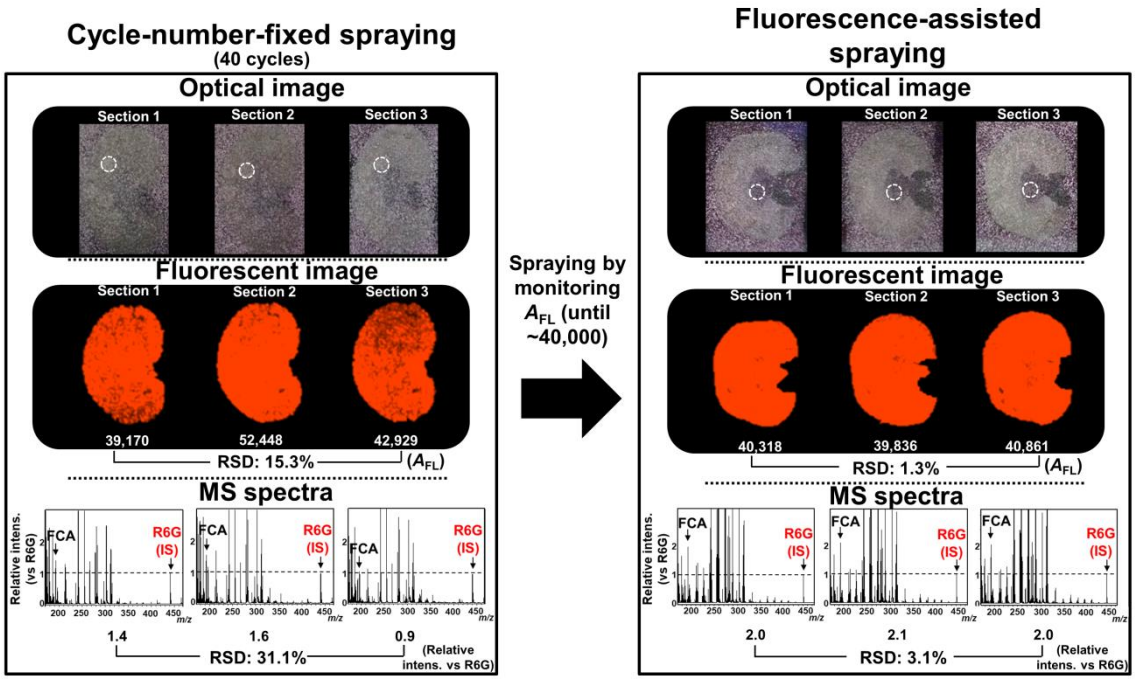

Figure 3-8 Evaluation of fluorescence-assisted spraying method for reproducible matrix crystal formation in MALDI-MS imaging technique

The optical image, fluorescent image, and MS spectra were acquired by 40 cycles of cycle-number-fixed spraying and fluorescence-assisted spraying until the desired fluorescence intensity of ~40,000 was achieved. MS spectra of the spotted analyte (FCA; 0.1 mM, 20 pmol/spot, shown as white dotted circle) were acquired for each matrix spraying method. 1,5-DAN (10 mg/mL) solution containing *O*-DNB (10 mg/mL) as a matrix additive and R6G (40 μg/mL) as the IS was sprayed onto the blank kidney tissue sections. The relative standard deviation (RSD) was calculated for relative MS intensity of FCA to R6G (IS) and A_{FL}, as acquired from the ROI of FCA spotted onto the blank kidney tissue section.

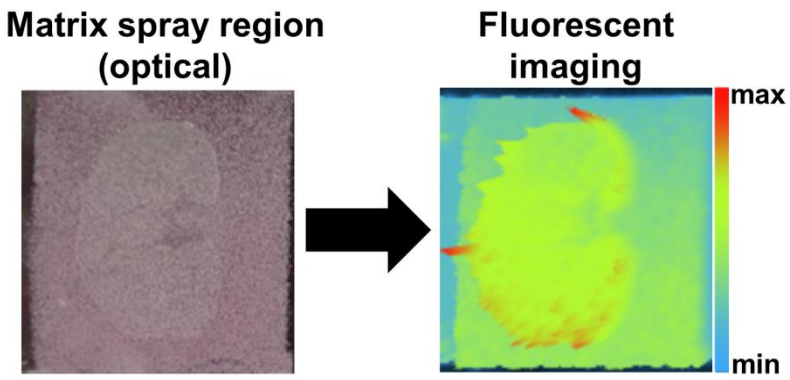

Figure 3-9 Optical and fluorescent images (shown as 3D mode) of kidney section sprayed with 1,5-DAN (10 mg/mL) containing R6G (40 µg/mL) and *O*-DNB (10 mg/mL) as the matrix additives

Optical and fluorescent images of R6G were obtained by the fluorescent imager using a green filter (excitation/emission = 530/595 nm) at a detection time of 0.5 s after fluorescence-assisted matrix spraying until the desired fluorescent intensity of ~40,000.

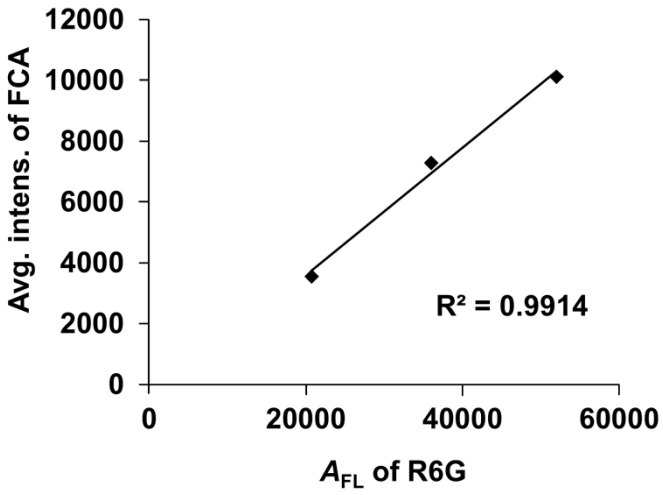

Figure 3-10 Linear correlation between MS intensity of FCA and matrix amount (fluorescent intensity of R6G)

The matrix crystal of the 1,5-DAN solution (10 mg/mL) containing R6G (40 µg/mL) and *O*-DNB (10 mg/mL) was sprayed onto spotted FCA (200 pmol/0.2 µL spot) corresponding to 50 pmol/mm^2 on the kidney tissue section. The MS intensity of FCA and fluorescent intensity of R6G extracted from the FCA spot area on kidney tissue sections were calculated as average intensity [sum of the spectra/the number of pixels in the ROI].

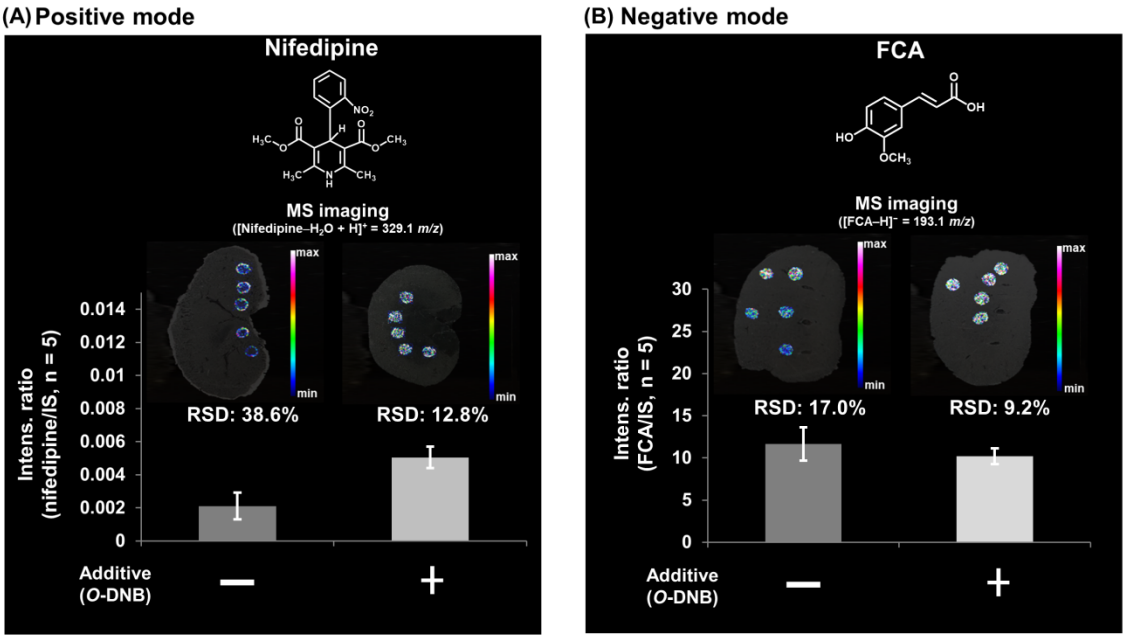

Figure 3-11 Reproducibility of the MALDI-MS imaging technique using fluorescence-assisted spraying method with or without *O*-DNB

(A) Nifedipine (200 pmol/0.2 µL spot, n = 5) and (B) FCA (200 pmol/0.2 µL spot, n = 5) were spotted on the blank kidney tissue sections, which was subjected afterward to the present MALDI-MS imaging technique. The MS images for nifedipine ($[M-H_2O+H]^+$ = 329. *m/z*) and FCA ($[M-H]^-$ = 193.1 *m/z*), as well as the ratio of their intensities to R6G (as IS), are shown. The average intensity was calculated as the sum of the MS spectra that were calculated with MS spectra from 4 mm^2 of the ROI (400 pixels/4 mm^2) covering the whole spot area (corresponding to 50 pmol/mm^2). The results are expressed as the mean ± SD obtained from five independent spots. RSD: relative standard deviation.

Moreover, since the chemical compounds *O*-DNB and R6G were developed as matrix additive to form fine crystal and spraying internal standard (IS), respectively, these compounds are applicable not only to the ImagePrep station employed in the present study but also to other automatic and robotic matrix sprayers, such as HTX TM-sprayers, which improves the reproducible capability of MALDI-MS imaging technique.

3.2. Quantitative MALDI-MS imaging technique with a fluorescence-assisted spraying method

The quantitative capabilities of the present MALDI-MS imaging technique employing fluorescence-assisted constant matrix spraying were assessed in both the positive- and negative-ion linear modes. To validate the present qMALDI-MS imaging technique of the tissue-accumulated analytes, the absorbable compounds of FCA[121−123] (a representative bioactive food compound) and nifedipine[124−126] (oral drug) were analyzed in both the positive- and negative-ion modes, respectively (Figures 3-12 and 3-13). MS images in Figure 3-12A shows a 'coffee ring effect' of the crystal formation of nifedipine, but not FCA owing to its hydrophobic characteristic (Figure 3-13A),[140] which demonstrated that the present matrix spraying method can maintain spatial distribution of the organ accumulated-analytes. According to this MALDI-MS imaging technique, a linear correlation was revealed in the intensity ratios of the spotted nifedipine (R^2 = 0.965, 0.5–40 pmol/mm^2) and FCA (R^2 = 0.9972, 0.5–75 pmol/mm^2) against R6G in the kidney tissue sections that were subjected to a constant matrix spray amount [fluorescent intensity, 43,803 ± 1,645 (in the positive ion mode), 37,395 ± 3,079 (in the negative ion mode)]. As regards the linear response of the calibration curves, it has been reported that the threshold laser fluence in MALDI depends on the analyte-to-matrix molar ratio,[141] and above the threshold, MS intensities increase

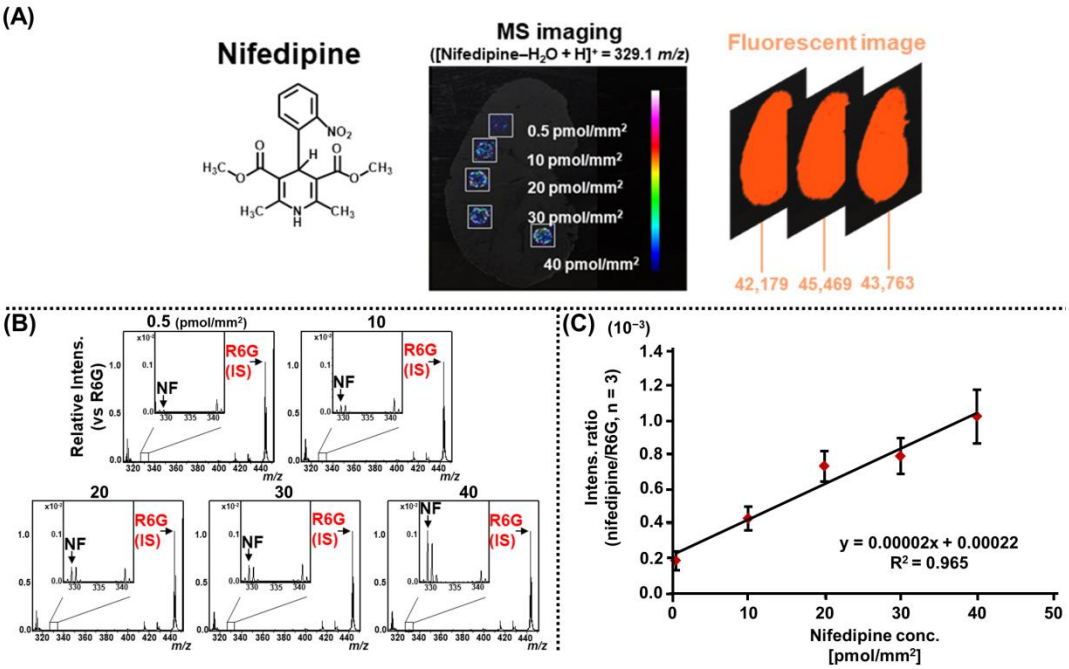

Figure 3-12 Calibration curve of nifedipine in rat kidney tissue section obtained via the qMALDI-MS imaging technique using the fluorescence-assisted matrix spraying method in the positive modes

(A) MS image of a series of spotted nifedipine (NF, $[M-H_2O+H]^+$ = 329.1 *m/z*, 0.5−40 pmol/mm^2) was acquired on the blank kidney tissue sections via positive-qMALDI-MS imaging technique. The fluorescent images of the positive MS images were inserted to show the formation of the reproducible matrix crystal. (B) The relative MS intensities of nifedipine to R6G (IS) were acquired from the sum of the spectra from the ROI (4 mm^2) to cover whole spotted analytes on the kidney tissue sections. (C) The result of the calibration curve of nifedipine was expressed as the mean ± SD of three independent tissue samples.

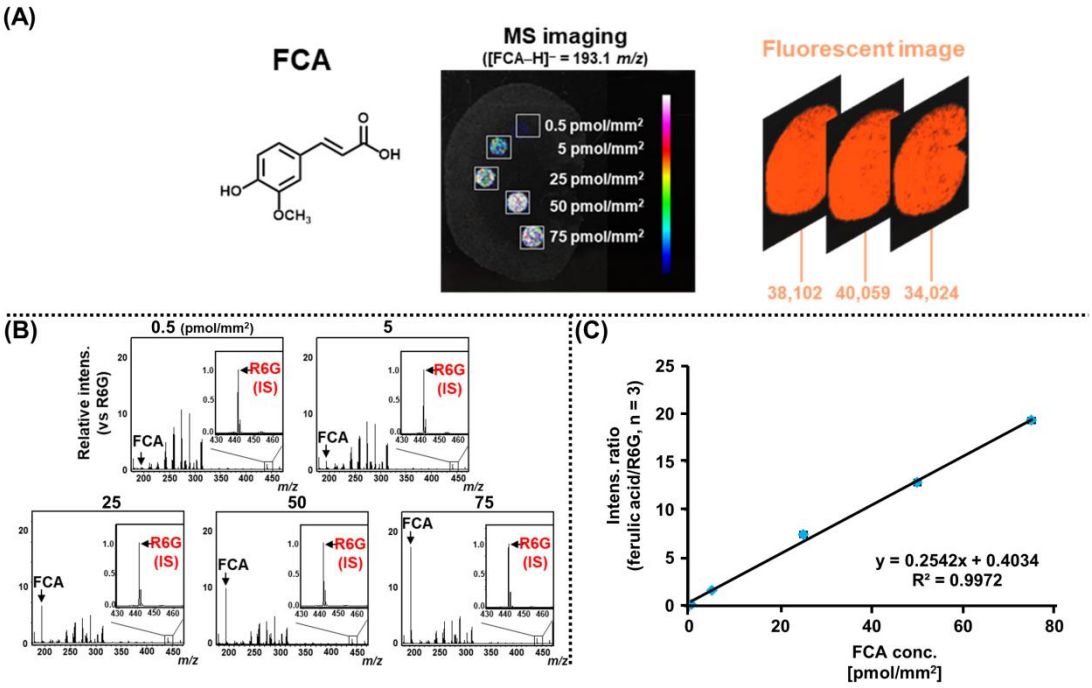

Figure 3-13 Calibration curve of FCA in rat kidney tissue section obtained via the qMALDI-MS imaging technique using the fluorescence-assisted matrix spraying method in the negative modes

(A) MS image of a series of spotted FCA ($[M-H]^-$ = 193.1 *m/z*, 0.5−75 pmol/mm^2) was acquired on the blank kidney tissue sections via negative-qMALDI-MS imaging technique. The fluorescent images of the negative MS images were inserted to show the formation of the reproducible matrix crystal. (B) The relative MS intensities of FCA to R6G (IS) were acquired from the sum of the spectra from the ROI (4 mm^2) to cover whole spotted analytes on the kidney tissue sections. (C) The result of the calibration curve of FCA was expressed as the mean ± SD of three independent tissue samples.

steeply as a power function of laser fluence.[142] Thus, the optimization of laser power along with the use of a dilution series of internal standard compensating broad changes in analyte-to-matrix molar ratio would be substantially important to enhance the linearity of calibration curves for qMALDI-MS methods. Despite the fact that a constant laser power was applied without such a compensating approach, the obtained calibration curves exhibit superb linearity in the present qMALDI-MS imaging technique (Figures 3-12 and 3-13). Based on the calibration curves of FCA and nifedipine, the LOD, LOQ, and intra- and inter-tissue precisions were obtained [for FCA: LOD, 0.12 pmol/mm^2; LOQ 0.36 pmol/mm^2; and intra- and inter-tissue RSDs, 5.4% and 2.5%, respectively (n = 3). For nifedipine, LOD, 0.35 and LOQ, 1.07 pmol/mm^2, respectively, and intra- and inter-tissue RSDs, 5.1% and 6.9%, respectively (n = 3) (Table 3-1)]. Comparing the reproducibility of the conventional cycle number-fixed spraying (Table 3-2), these validation parameters exhibited that the present fluorescence-assisted matrix spraying method significantly enhanced the quantitative capabilities of MALDI-MS imaging technique. Furthermore, Table 3-3 showed the poor reproducibility and linearity of the present data without normalization employing MS intensity of R6G, which clearly indicated the significance of the normalization to compensate the variability owing to heterogenous co-crystallization of analytes, R6G, and matrix and ion suppression.

3.3. Quantitative evaluation of tissue accumulation of FCA in rat kidney

In the present study, FCA, which can be accumulated in the tissues and organs, including kidney,[121−123] was employed to validate the quantitative capability of this qMALDI-MS assay using the fluorescence-assisted spraying method. After the oral administration of FCA, the time-course accumulation behaviors (0–60 min) of

kidney-accumulated FCA were observed by using conventional quantitative LC-MS analysis (Figures 3-14 and 3-15) after its oral administration (50 mg/kg).

Table 3-1 Method validation parameters for the present qMALDI-MS imaging technique of nifedipine and FCA using fluorescent-assisted spraying

Mode	Analyte	LOD (pmol/mm²)	LOQ (pmol/mm²)	Intra-tissue precision of the intens. ratio, RSD (%)[a]	Inter-tissue precision of the intens. ratio, RSD (%)[a]
Positive	Nifedipine	0.35	1.07	5.1	6.9
Negative	FCA	0.12	0.36	5.4	2.5

[a]: n = 3

Table 3-2 Method validation parameters for MALDI-MS imaging technique of FCA using conventional spraying method (40 cycles)

Mode	Analyte	Linearity regression r^2 value[a]	Calibration range (pmol/mm^2)	LOD (pmol/mm^2)	LOQ (pmol/mm^2)	Intra-tissue precision of the intens. ratio, RSD (%)[a]	Inter-tissue precision of the intens. ratio, RSD (%)[a]
Negative	FCA	0.9349	0.5 - 75	0.6	1.7	20.1	32.3

[a]: r^2 value across three calibration sets during validation

[b]: n = 3

Table 3-3 Method validation parameters for the present MALDI-MS imaging technique of nifedipine and FCA without normalization using MS intensity of R6G

Mode	Analyte	Linearity regression r^2 value[a]	Calibration range (pmol/mm^2)	LOD (pmol/mm^2)	LOQ (pmol/mm^2)	Intra-tissue precision of the intens. ratio, RSD (%)[a]	Inter-tissue precision of the intens. ratio, RSD (%)[a]
Positive	Nifedipine	0.894	0.5 - 40	0.36	1.09	6.4	18.5
Negative	FCA	0.9264	0.5 - 75	0.17	0.52	25.5	68.8

[a]: r^2 value across three calibration sets during validation

[b]: n = 3

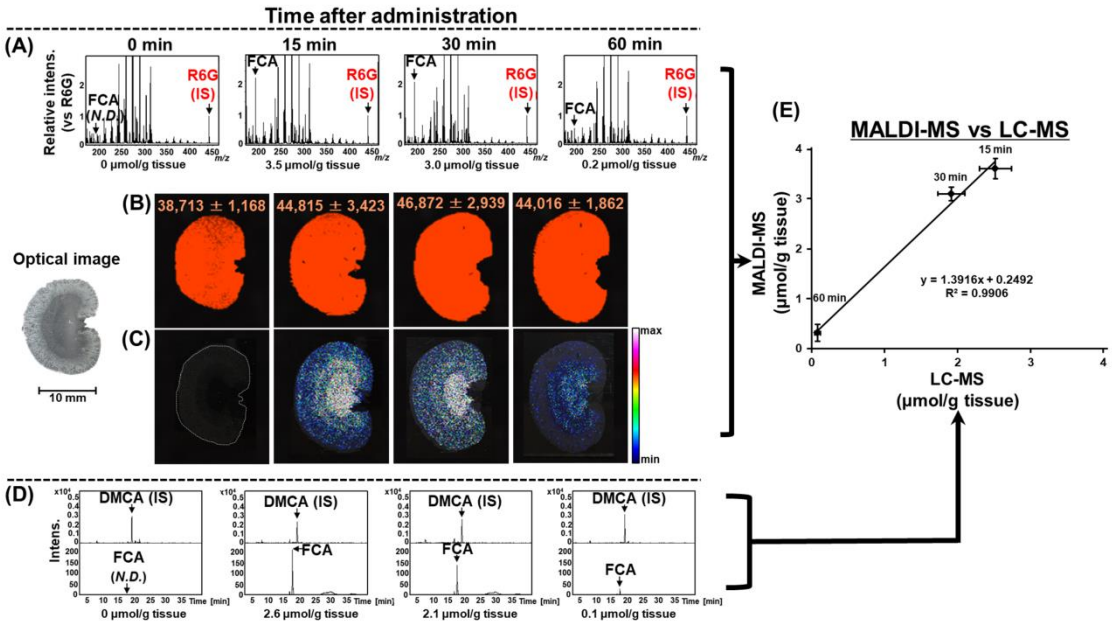

Figure 3-14 Comparison of qMALDI-MS and LC-MS of the kidney-accumulated FCA after the oral administration (50 mg/kg)

The corresponding sum of the MS spectra (A) and fluorescent images (B) was obtained from the whole MS-imaging-analyzed tissue regions (C) of FCA ($[M-H]^-$ = 193.1 *m/z*). The corresponding extracted-ion chromatograms (D) of FCA (193.0527 *m/z*) and DMCA (207.0657 *m/z*) as IS, of kidney tissue sections by quantitative LC-MS were also shown. The correlation curves (E) of the tissue-accumulated FCA were prepared for the present qMALDI-MS imaging technique and the validated LC-MS system, and these results are expressed as the mean ± SD from three independent tissue samples. *N.D.* indicates that there was no MS detection.

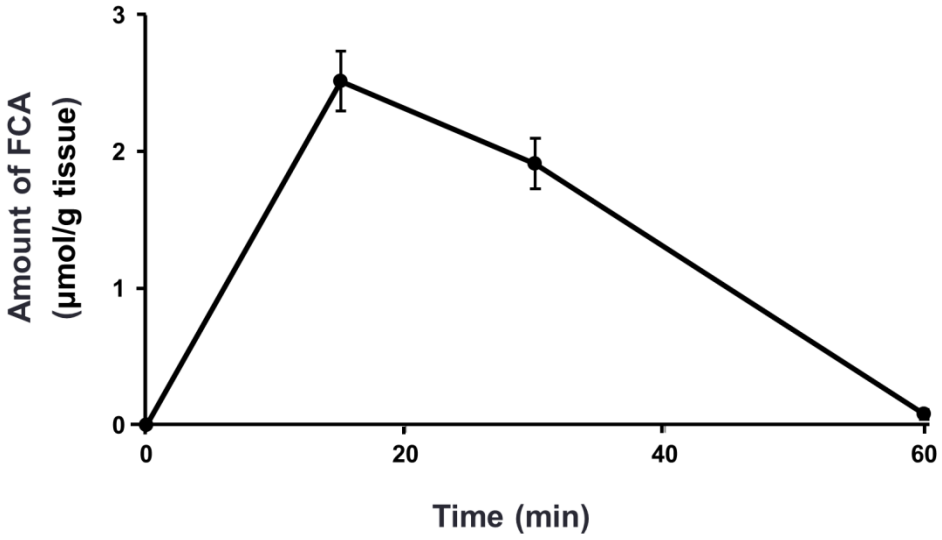

Figure 3-15 Time-course accumulation of FCA in rat kidney after the oral administration of FCA by LC-MS

The results are expressed as the mean ± SD (n = 3).

The kidney-accumulated FCA was also quantified by the present qMALDI-MS imaging technique at a constant matrix amount distribution with the following fluorescent intensities of R6G: 0 min, 37,395 ± 3,423; 15 min, 44,815 ± 3,423; 30 min, 46,872 ± 2,939; 60 min, 44,016 ± 3,225; using adjacent sequential tissue sections that were also employed for the LC-MS analysis. The amount of kidney-accumulated FCA, as quantified by the present qMALDI-MS imaging technique, was 1.4-folds higher than the quantitative value by LC-MS analyses (slope of the correlation curve: 1.3916, (Figure 3-14). These results agree with a reported one previously[105] in which the tissue-accumulated amount of the analyte (i.e. tetrandrine), as quantified by qMALDI-MS, was higher than quantitative value via LC-MS analyses. Since both the present qMALDI-MS and LC-MS used the external standardization to quantify the kidney-accumulated FCA, these higher quantitative values by qMALDI-MS method may exhibit higher extraction efficiency of kidney-accumulated FCA from extremely thin tissue sections (12 μm) by the present qMALDI-MS than that by LC-MS. Considering the higher extraction efficiency acquired from extremely thin tissue sections, this qMALDI-MS imaging technique might be applicable for various organs and analytes. Additionally, an advantage (simple sample preparation) of MALDI-MS imaging technique would also improve the extraction efficiency, thus preventing the loss of analytes and degradation via fatiguing preparation processes, as observed by LC-MS. Notably, a significant linear correlation coefficient was observed between the present qMALDI-MS imaging technique and LC-MS using the time-course accumulation of FCA into the kidney tissues of the SD rats (R^2 = 0.9906, n = 3, Figure 3-14). The quantitative performance of MALDI-MS imaging technique by Chumbley et al.[104] who used a robotic spotter and isotope-labeled ISs, is the best (RSD = 11.4%) thus far. However, their micro-spotting method was restricted by the spot distance (>250 μm), whereas this qMALDI-MS imaging technique employing the fluorescence-assisted

spraying method could be a key technique for the application of matrix spraying, which can achieve high-spatial-resolution of MS image (spatial resolution >10 μm).[143−145] Moreover, considering the utilization of the present chemical improvement in the homogeneity of matrix crystals and uniformity of matrix amount, qMALDI-MS imaging technique at micron-level resolution might be accomplished using advanced matrix sprayers.[146] Figure 3-16 shows that this qMALDI-MS imaging technique could visualize its specific tissue localization and quantify the amount of tissue-accumulated FCA. For instance, FCA was quantified in the pelvis, medulla, and cortex regions after 15 min of the oral administration at 18.5, 4.9, and 1.3 μmol/g dry tissue, respectively, assuming that the tissue density of the whole kidney tissue section was homogeneous. Moreover, the accumulated amount reduced with time after the oral administration of FCA. For example, the pelvis-specific tissue accumulations of FCA were 18.5, 11.5, and 1.5 μmol/g dry tissue in 15, 30, and 60 min, respectively (Figure 3-16). These findings indicate that this qMALDI-MS imaging technique can quantify the regional tissue accumulation of analytes.

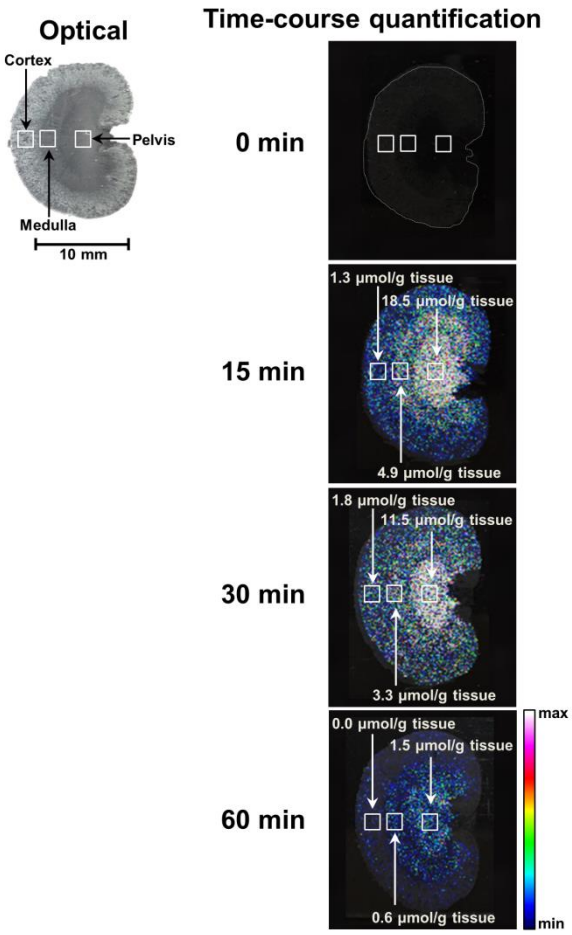

Figure 3-16 Regional and time-course quantification of the tissue-accumulated FCA in rat kidney by the present qMALDI-MS imaging technique

Regional and time-course quantification of kidney-accumulated FCA ($[M-H]^-$ = 193.1 *m/z*) after 0, 15, 30, and 60 min of its oral administration (50 mg/kg) was conducted by the present qMALDI-MS imaging technique. The FCAs were localized and quantified at the pelvis, medulla, and cortex regions; Average MS intensity ratio of FCA to R6G was calculated with MS spectra from 1 mm^2 of the ROI (100 pixels/1 mm^2) to quantify regional kidney area. The inserted MS images are the same as that in Figure 3-14C.

4. Summary

MALDI-MS imaging technique, which can visualize spaial distribution of ionizable compounds in biological tissues without the necessity for labeling such as the antibodies, is tremendously useful in evaluating physiologically active food compounds localized and accumulated in organs. However, the conventional MALDI-MS is regarded to lack quantitative properties owing to the inhomogeneity of matrix crystal formation and the low-level reproducibility of matrix spray conditions. Thus, in **Chapter III,** a new matrix additive was proposed, which can form homogeneous matrix crystals, and a fluorescent standard substance (a MS normalizing standard) to improve quantitative capability in MALDI-MS imaging technique. In this chapter, FCA was used as the aimed bioactive food compound. In order to control the spray amount of matrix and normalize the MS intensity, R6G, which is MS detectable fluorescent substance, was added to the matrix solution (1,5-DAN). Furthermore, *O*-DNB was employed as a matrix additive to form homogeneous matrix crystals on the kidney sections, and ImagePrep was employed to spray the matrix solution with fluorescence intensity (λ_{ex}: 530 nm, λ_{em}: 595 nm) of R6G at the desired value (40,000 a.u.: optimum intensity of MS ionization) on the kidney section (Figure 3-8). FCA spotted on the kidney section was prepared for qMALDI-MS imaging technique.

At the matrix spraying condition using 1,5-DAN solution containing the R6G and *O*-DNB, linearity (R^2 = 0.9972, 0.5–75 pmol/mm^2) and reproducibility (RSD = 3.1%) of relative MS intensity of FCA were significantly enhanced compared to results of conventional cycle-number-fixed spraying (40 cycles, R^2 = 0.9349, RSD = 31.1%). Then, FCA accumulated in kidney tissue was visually determined to be 3.5, 3.0, and 0.2 μmol/g dry tissue at 15, 30, and 60 min after the oral administration of FCA (50 mg/kg),

respectively. Furthermore, a linear correlation was observed between the novel qMALDI-MS imaging technique and LC-MS results (n = 3, R^2 = 0.9906). Based on these results, qMALDI-MS imaging technique was accomplished via fluorescence-assisted matrix spraying method using R6G as a MS normalizing standard in the 1,5-DAN solution containing *O*-DNB (a matrix additive), which successfully quantified tissue-accumulated FCA in kidney tissue sections after the oral administration.

Chapter IV

Conclusion

Most studies on the physiological effects of food-derived compounds such as anthocyanins have focused on evaluating bioactivity and its mechanisms *in vitro* and *in vivo*. However, there are few reports on bioactive food compounds' bioavailability such as intestinal absorption, metabolism, and tissue-accumulation in aimed organs. One of the factors would be considered as the lack of an analytical assay capable of accurate evaluation of their bioavailability and microenvironment of organs. Hence, the aim of the present study was to clarify bioavailability such as intestinal absorption, metabolism, and tissue accumulation of food compounds like anthocyanins using *in situ* MALDI-MS imaging technique. Then, the present study also aimed to establish novel MALDI-MS imaging technique to visually and quantitatively assess the tissue accumulation of food compounds.

Chapter II Visualization of rat intestinal absorption of acylated anthocyanins by MALDI-MS imaging technique

Regardless of numerous reports of the physiological benefits of anthocyanins, including acylated ones, it has been unclear whether they would be absorbed in their intact form. Therefore, in **Chapter II,** an *in situ* MALDI-MS imaging technique method that can visualize intestinal absorption/metabolism dynamics of ionizable compounds was used to evaluate the intestinal absorption process of anthocyanins, including an

acylated Cy (Cy-3-(2"-xylose-6"-feruloyl-glucose-galactoside, Cy3XFGG), in intestinal tissue. As a result, it was visualized that Cy3XFGG can be absorbed into intestinal tissue via OATP 2B1 in its intact form. Moreover, in this study, conjugated Cy3XFGG (glucuronidated, sulfated, methylated, and their combination forms) was not detected in the Cy3XFGG-transported intestine tissue sections, while Cy as a degraded form of Cy3XFGG and methylated Cy were slightly visualized in Cy3XFGG-transported tissue setions

Taken together, it was demonstrated for the first time that acylated anthocyanins could be successfully absorbed into intestine in its intact form after the intestinal transport experiment.

Chapter III Establishment of quantitative MALDI-MS imaging technique for tissue accumulation of anthocyanin-related compounds

MALDI-MS imaging technique is extremely useful for evaluating food compounds such as anthocyanins and their metabolites accumulated and localized in tissues. However, the conventional MALDI-MS method has been considered poor quantitative capability due to the lack of heterogeneity of matrix crystals on tissue sections and the reproducibility of matrix spraying conditions. Hence, **Chapter III** focused on establishing a novel quantification approach for MALDI-MS imaging technique by applying MS ionizable fluorescent compounds for nondestructive fluorescent monitoring of the sprayed matrix amount, and additives to improve the homogeneity of the matrix crystal. As a result, successful quantitative and reproducible capabilities of MALDI-MS imaging technique of FCA were achieved via fluorescence-assisted reproducible matrix spraying and formation of matrix crystals by R6G (the MS normalizing standard) in the 1,5-DAN solution containing *O*-DNB. Moreover, the

present qMALDI-MS imaging technique quantitatively visualized tissue-accumulated FCA in kidneys after the oral administration.

Taken together, the present MALDI-MS imaging technique with fluorescence-assisted spraying method was firstly established as visible and quantitative evaluation technique to evaluate bioavailability of food compounds, such as metabolism, intestinal absorption, and tissue-accumulation. In the future, it is highly expected that this qMALDI-MS imaging technique will be a powerful analytical method to clarify the mechanisms of physiological functionalities of food compounds from the viewpoint of bioavailability.

Reference

(1) Egert, S.; Bosy-Westphal, A.; Seiberl, J.; Kürbitz, C.; Settler, U.; Plachta-Danielzik, S.; Wagner, A. E.; Frank, J.; Schrezenmeir, J.; Rimbach, G.; Wolffram, S.; Müller, M. J. Quercetin reduces systolic blood pressure and plasma oxidised low-density lipoprotein concentrations in overweight subjects with a high-cardiovascular disease risk phenotype: A double-blinded, placebo-controlled cross-over study. *Br. J. Nutr.*, **2009**, *102*, 1065–1074.

(2) Toth, P. P.; Patti, A. M.; Nikolic, D.; Giglio, R. V.; Castellino, G.; Biancucci, T.; Geraci, F.; David, S.; Montalto, G.; Rizvi, A.; Rizzo, M. Bergamot reduces plasma lipids, atherogenic small dense LDL, and subclinical atherosclerosis in subjects with moderate hypercholesterolemia: A 6 months prospective study. *Front. Pharmacol.*, **2016**, *6*, 299.

(3) Jung, U. J.; Kim, H. J.; Lee, J. S.; Lee, M. K.; Kim, H. O.; Park, E. J.; Kim, H. K.; Jeong, T. S.; Choi, M. S. Naringin supplementation lowers plasma lipids and enhances erythrocyte antioxidant enzyme activities in hypercholesterolemic subjects. *Clin. Nutr.*, **2003**, *22*, 561–568.

(4) Lazarevic, B.; Boezelijn, G.; Diep, L. M.; Kvernrod, K.; Ogren, O.; Ramberg, H.; Moen, A.; Wessel, N.; Berg, R. E.; Egge-Jacobsen, W.; Hammarstrom, C.;Svindland, A.; Kucuk, O.; Saatcioglu, F.; Taskèn, K. A.; Karlsen, S. J. Efficacy and safety of short-term genistein intervention in patients with localized prostate cancer prior to radical prostatectomy: A randomized, placebo-controlled, double-blind phase 2 clinical trial. *Nutr. Cancer*, **2011**, *63*, 889–898.

(5) Yang, Y.-S.; Su, Y.-F., Yang, H.-W., Lee, Y.-H., Chou, J. I., and Ueng, K. -C. Lipid-lowering effects of curcumin in patients with metabolic syndrome: A randomized, double-blind, placebo-controlled trial. *Phytother. Res.*, **2014**, *28*, 1770–1777.

(6) Zahedi, M.; Ghiasvand, R.; Feizi, A.; Asgari, G.; Darvish, L. Does quercetin improve cardiovascular risk factors and inflammatory biomarkers in women with type 2 diabetes: A double-blind randomized controlled clinical trial. *Int. J. Prev. Med.*, **2013**, *4*, 777–785.

(7) Habauzit, V.; Verny, M.-A.; Milenkovic, D.; Barber-Chamoux, N.; Mazur, A.; Dubray, C.; and Morand, C. In arterial stiffness Flavanones protect from postmenopausal women consuming grapefruit juice for 6 Mo: A randomized, controlled, crossover trial. *Am. J. Clin. Nutr.*, **2015**, *102*, 66–74.

(8) Morand, C.; Dubray, C.; Milenkovic, D.; Lioger, D.; Martin, J. F.; Scalbert, A.; Mazur, A. Hesperidin contributes to the vascular protective effects of orange juice: A randomized crossover study in healthy volunteers. *Am. J. Clin. Nutr.*, **2011**, *93*, 73–80.

(9) Reshef, N.; Hayari, Y.; Goren, C.; Boaz, M.; Madar, Z.; Knobler, H. Antihypertensive effect of sweetie fruit in patients with stage I hypertension. *Am. J. Hypertens.*, **2005**, *18*, 1360–1363.

(10) Brasnyó, P.; Molnár, G. A.; Mohás, M.; Markó, L.; Laczy, B.; Cseh, J.; Mikolás, E.; Szijártó, I. A.; Mérei, Á .; Halmai, R.; Mészáros, L. G.; Sümegi, B.; Wittmann, I. Resveratrol improves insulin sensitivity, reduces oxidative stress and activates the Akt pathway in type 2 diabetic patients. *Br. J. Nutr.*, **2011**, *106*, 383–389.

(11) Chuengsamarn, S.; Rattanamongkolgul, S.; Luechapudiporn, R.; Phisalaphong, C.; Jirawatnotai, S. Curcumin extract for prevention of type 2 diabetes. *Diabetes Care*, **2012**, *35*, 2121–2127.

(12) Homayouni, F.; Haidari, F.; Hedayati, M.; Zakerkish, M.; Ahmadi, K. Blood pressure lowering and anti-inflammatory effects of hesperidin in type 2 diabetes; A randomized double-blind controlled clinical trial. *Phytother. Res.*, **2018**, *32*, 1073–1079.

(13) Espinoza, J. L.; Trung, L. Q.; Inaoka, P. T.; Yamada, K.; An, D. T.; Mizuno, S.; Nakao, S.; Takami, A. The repeated administration of resveratrol has measurable effects on circulating T-cell subsets in humans. *Oxid. Med. Cell. Longev.*, **2017**, e6781872.

(14) Ganjali, S.; Sahebkar, A.; Mahdipour, E.; Jamialahmadi, K.; Torabi, S.; Akhlaghi, S.; Ferns, G.; Parizadeh, S. M. R.; Ghayour-Mobarhan, M. Investigation of the effects of curcumin on serum cytokines in obese individuals: A randomized controlled trial. *Sci. World J.*, **2014**, e898361.

(15) Terahara, N. Flavonoids in foods: A review. *Nat. Prod. Commun.*, **2015**, *10*, 521−528.

(16) De Ferrars, R.; Czank, C.; Zhang, Q.; Botting, N.; Kroon, P.; Cassidy, A.; Kay, C. The pharmacokinetics of anthocyanins and their metabolites in humans. *Br. J. Pharmacol.*, **2014**, *171*, 3268−3282.

(17) Prior, R. L.; Wu, X. Anthocyanins: Structural characteristics that result in unique metabolic patterns and biological activities. *Free Radic. Res.*, **2006**, *40*, 1014−1028.

(18) Yoshikawa, M.; Fujita, H.; Matoba, N.; Takenaka, Y.; Yamamoto, T.; Yamauchi, R.; Tsuruki, H.; Takahata, K. Bioactive peptides derived from food proteins preventing lifestyle-related diseases. *BioFactors*, **2000**, *12*, 143−146.

(19) Á vila-Gálvez, M.; García-Villalba, R.; Martínez-Díaz, F.; Ocaña-Castillo, B.; Monedero-Saiz, T.; Torrecillas-Sánchez, A.; Abellán, B.; González-Sarrías, A.; Espín, J. Metabolic profiling of dietary polyphenols and methylxanthines in normal and malignant mammary tissues from breast cancer patients. *Mol. Nutr. Food Res.*, **2019**, *63*, e1801239.

(20) Song, N. R.; Yang, H.; Park, J.; Kwon, J. Y.; Kang, N. J.; Heo, Y. S.; Lee, K. W.; Lee, H. J. Cyanidin suppresses neoplastic cell transformation by directly targeting phosphatidylinositol 3-kinase. *Food Chem.*, **2012**, *133*, 658−664.

(21) Valenza, A.; Bonfanti, C.; Pasini, M. E.; Bellosta, P. Anthocyanins function as anti-inflammatory agents in a Drosophila model for adipose tissue macrophage infiltration. *BioMed Res. Int.*, **2018**, 6413172.

(22) Karlsen, A.; Retterstøl, L.; Laake, P.; Paur, I.; Kjølsrud-Bøhn, S.; Sandvik, L.; Blomhoff, R. Anthocyanins inhibit nuclear factor-κB activation in monocytes and reduce plasma concentrations of pro-inflammatory mediators in healthy adults. *J. Nutr.*, **2007**, *137*, 1951−1954.

(23) Hoggard, N.; Cruickshank, M.; Moar, K.-M.; Bestwick, C.; Holst, J. J.; Russell, W.; Horgan, G. A single supplement of a standardised bilberry (*Vaccinium myrtillus* L.) extract (36% wet weight anthocyanins) modifies glycaemic response in individuals with type 2 diabetes controlled by diet and lifestyle. *J. Nutr. Sci.*, **2013**, *2*, e22.

(24) Hassimotto, N.; Genovese, M.; Lajolo, F. Absorption and metabolism of cyanidin-3-glucoside and cyanidin-3-rutinoside extracted from wild mulberry (*Morus nigra* L.) in rats. *Nutr. Res.*, **2008**, *28*, 198−207.

(25) Peng, N.; Clark, J. T.; Prasain, J.; Kim, H.; White, C. R.; Wyss, J. M. Antihypertensive and cognitive effects of grape polyphenols in estrogen-depleted, female, spontaneously hypertensive rats. *Am. J. Physiol.: Regul., Integr. Comp. Physiol.*, **2005**, *289*, R771−R775.

(26) Matsui, T.; Ebuchi, S.; Kobayashi, M.; Fukui, K.; Sugita, K.; Terahara, N.; Matsumoto, K. Anti-hyperglycemic effect of diacylated anthocyanin derived from Ipomoea batatas cultivar Ayamurasaki can be achieved through the α-glucosidase inhibitory action. *J. Agric. Food Chem.*, **2002**, *50*, 7244−7248.

(27) Reis, J. F.; Monteiro, V. V. S.; de Souza Gomes, R.; do Carmo, M. M.; da Costa, G. V.; Ribera, P. C.; Monteiro, M. C. Action mechanism and cardiovascular effect of anthocyanins: a systematic review of animal and human studies. *J. Transl. Med.*, **2016**, *14*, 315.

(28) Vendrame, S.; Klimis-Zacas, D. Potential factors influencing the effects of anthocyanins on blood pressure regulation in humans: a review. *Nutrients*, **2019**, *11*, 1431.

(29) Kamiloglu, S.; Grootaert, C.; Capanoglu, E.; Ozkan, C.; Smagghe, G.; Raes, K.; Van Camp, J. Anti-inflammatory potential of black carrot (*Daucus carota* L.) polyphenols in a co-culture model of intestinal Caco-2 and endothelial EA.hy926 cells. *Mol. Nutr. Food Res.*, **2017**, *61*, 1600455.

(30) Tsutsumi, A.; Horikoshi, Y.; Fushimi, T.; Saito, A.; Koizumi, R.; Fujii, Y.; Hu, Q. Q.; Hirota, Y.; Aizawa, K.; Osakabe, N. Acylated anthocyanins derived from purple carrot (*Daucus carota* L.) induce elevation of blood flow in rat cremaster arteriole. *Food Funct.*, **2019**, *10*, 1726−1735.

(31) Cardona, F.; Andres-Lacueva, C.; Tulipani, S.; Tinahones, F. J.; Queipo-Ortuno, M. I. Benefits of polyphenols on gut microbiota and implications in human health. *J. Nutr. Biochem.*, **2013**, *24*, 1415−1422.

(32) Faria, A.; Fernandes, I.; Norberto, S.; Mateus, N.; Calhau, C. Interplay between anthocyanins and gut microbiota. *J. Agric. Food Chem.*, **2014**, *62*, 6898−6902.

(33) Jones, C. B.; Davis, C. M.; Sfanos, K. S. The potential effects of radiation on the gut-brain axis. *Radiat. Res.*, **2020**, *193*, 209−222.

(34) Matsui, T. Polyphenols-absorption and occurrence in the body system. *Food Sci. Technol. Res.*, **2022**, *28*,13−33.

(35) Manach, C.; Morand, C.; Demigne, C.; Texier, O.; Regerat, F.; Rémésy, C. Bioavailability of rutin and quercetin in rats. *FEBS. Lett.*, **1997**, *409*,12−16.

(36) Han, H.; Liu, C.; Gao, W.; Li, Z.; Qin, G.; Qi, S.; Jiang, H.; Li, X.; Liu, M.; Yan, F.; Guo, Q.; Hu, C. Y. Anthocyanins Are Converted into Anthocyanidins and Phenolic Acids and Effectively Absorbed in the Jejunum and Ileum. *J. Agric. Food Chem.*, **2021**, *69*, 992−1002.

(37) Kurilich, A. C.; Clevidence, B. A.; Britz, S. J.; Simon, P. W.; Novotny, J. A. Plasma and urine responses are lower for acylated vs nonacylated anthocyanins from raw and cooked purple carrots. *J. Agric. Food Chem.*, **2005**, *53*, 6537−6542.

(38) Charron, C. S.; Clevidence, B. A.; Britz, S. J.; Novotny, J. A. Effect of dose size on bioavailability of acylated and nonacylated anthocyanins from red cabbage (Brassica oleracea L. var. capitata). *J. Agric. Food Chem.*, **2007**, *55*, 5354−5362.

(39) Tsuda, T.; Horio, F.; Osawa, T. Absorption and metabolism of cyanidin-3-*O*-*β*-D-glucoside in rats. *FEBS. Lett.*, **1999**, *449*, 179−182.

(40) Kirakosyan, A.; Seymour, E. M.; Wolforth, J.; McNish, R.; Kaufman, P. B.; Bolling, S. F. Tissue bioavailability of anthocyanins from whole tart cherry in healthy rats. *Food Chem.*, **2015**, *171*, 26−31.

(41) Miyazawa, T.; Nakagawa, K.; Kudo, M.; Muraishi, K.; Someya, K. Direct intestinal absorption of red fruit anthocyanins, cyanidin-3-glucoside and cyanidin-3,5-diglucoside, into rats and humans. *J. Agric. Food Chem.*, **1999**, *47*, 1083−1091.

(42) Matsumoto, H.; Inaba, H.; Kishi, M.; Tominaga, S.; Hirayama, M.; Tsuda, T. Orally administered delphinidin 3-rutinoside and cyanidin 3-rutinoside are directly absorbed in rats and humans and appear in the blood as the intact forms. *J. Agric. Food Chem.*, **2001**, *49*, 1546−1551.

(43) Matsumoto, H.; Ichiyanagi, T.; Iida, H.; Ito, K.; Tsuda, T.; Hirayama, M.; Konishi, T. Ingested delphinidin-3-rutinoside is primarily excreted to urine as the intact form and to bile as the methylated form in rats. *J. Agric. Food Chem.*, **2006**, *54*, 578−582.

(44) Cao, G.; Muccitelli, H. U.; Sanchez-Moreno, C.; Prior, R. L. Anthocyanins are absorbed in glycated forms in elderly women: a pharmacokinetic study. *Am. J. Clin. Nutr.*, **2001**, *73*, 920−926.

(45) Bub, A.; Watzl, B.; Heeb, D.; Rechkemmer, G.; Briviba, K. Malvidin-3-glucoside bioavailability in humans after ingestion of red wine, dealcoholized red wine and red grape juice. *Eur. J. Nutr.*, **2001**, *40*, 113−120.

(46) Frank, T.; Netzel, M.; Strass, G.; Bitsch, R.; Bitsch, I. Bioavailability of anthocyanidin-3-glucosides following consumption of red wine and red grape juice. *Can. J. Physiol. Pharmacol.*, **2003**, *81*, 423−435.

(47) Bitsch, R.; Netzel, M.; Frank, T.; Strass, G.; Bitsch, I. Bioavailability and biokinetics of anthocyanins from red grape juice and red wine. *J. Biomed. Biotechnol.*, **2004**, 293−298.

(48) Kay, C. D.; Mazza, G.; Holub, B. J. Anthocyanins exist in the circulation primarily as metabolites in adult men. *J. Nutr.*, **2005**, *135*, 2582−2588.

(49) Stoner, G. D.; Sardo, C.; Apseloff, G.; Mullet, D.; Wargo, W.; Pound, V.; Singh, A.; Sanders, J.; Aziz, R.; Casto, B.; Sun, X. Pharmacokinetics of anthocyanins and ellagic acid in healthy volunteers fed freeze-dried black raspberries daily for 7 days. *J. Clin. Pharmacol.*, **2005**, *45*, 1153−1164.

(50) Hollman, P. C.; Bijsman, M. N.; van Gameren, Y.; Cnossen, E. P.; de Vries, J.H.; Katan, M.B. The sugar moiety is a major determinant of the absorption of dietary flavonoid glycosides in man. *Free Radic. Res.*, **1999**, *31*, 569-573.

(51) Shen, C.; Chen, R.; Qian, Z.; Meng, X.; Hu, T.; Li, Y.; Chen, Z.; Huang, C.; Hu, C.; Li, J. Intestinal absorption mechanisms of MTBH, a novel hesperetin derivative, in Caco-2 cells, and potential involvement of monocarboxylate transporter 1 and multidrug resistance protein 2. *Eur. J. Pharmacol.*, **2015**, *78*, 214−224.

(52) Kondo, A.; Narumi, K.; Ogura, J.; Sasaki, A.; Yabe, K.; Kobayashi, T.; Furugen, A.; Kobayashi, M.; Iseki, K. Organic anion-transporting polypeptide (OATP) 2B1 contributes to the cellular uptake of theaflavin. *Drug Metab. Pharmcokinet.*, **2017**, *32*, 145−150.

(53) Hansen, S.; Olsson, A.; Casanova, J. Wortmannin, an inhibitor of phosphoinositide 3-kinase, inhibits transcytosis in polarized epithelial cells. *J. Biol. Chem.*, **1995**, *270*, 28425−28432.

(54) Qadir, M.; O'Loughlin, K. L.; Fricke, S. M.; Williamson, N. A.; Greco, W. R.; Minderman, H.; Baer, M. R. Cyclosporin A is a broad-spectrum multidrug resistance modulator. *Clin. Cancer Res.*, **2005**, *11*, 2320−2326.

(55) Shimizu, M. Interaction between food substances and the intestinal epithelium. *Biosci. Biotechnol. Biochem.*, **2010**, *74*, 232–241.

(56) Claro, T.; Polli, J. E.; Swaan, P. W.; Editor, G.; Hediger, M. A. The solute carrier family 10 (SLC10): beyond bile acid transport. *Mol. Aspects Med.*, **2013**, *34*, 252–269.

(57) Baldwin, S. A.; Beal, P. R.; Yao, S. Y. M.; King, A. E.; Cass, C. E.; Young, J. D. The equilibrative nucleoside transporter family, SLC29. *Pflugers Arch.*, **2004**, *447*, 735–743.

(58) Yu, J.; Zhou, Z.; Tay-Sontheimer, J.; Levy, R. H.; Ragueneau-Majlessi, I. Intestinal drug interactions mediated by OATPs: a systematic review of preclinical and clinical findings. *J. Pharm. Sci.*, **2017**, *106*, 2312–2325.

(59) Halestrap, A. P.; Wilson, M. C. The monocarboxylate transporter family-role and regulation. *IUBMB Life*, **2012**, *64*, 109–119.

(60) Turk, E.; Martingn, M. G.; Wright, E. M. Structure of the human Na^+/glucose cotransporter gene SGLT1. *J. Biol. Chem.*, **1994**, *269*, 15204–15209.

(61) Meredith, D.; Price, R. A. Molecular modeling of PepT1-towards a structure. *J. Membr. Biol.*, **2006**, *213*, 79–88.

(62) Chen, Z.; Shi, T.; Zhang, L.; Zhu, P.; Deng, M.; Huang, C.; Hu, T.; Jiang, L.; Li, J. Mammalian drug efflux transporters of the ATP binding cassette (ABC) family in multidrug resistance: a review of the past decade. *Cancer Lett.*, **2016**, *370*, 153–164.

(63) Booth, A. N.; Jones, F. T.; deEds, F. Metabolic fate of hesperidin, eriodictyol, homoeriodictyol, and diosmin. *J. Biol. Chem.*, **1958**, *230*, 661–668.

(64) Nielsen, S. E.; Breinholt, V.; Justesen, U.; Cornett, C.; Dragsted, L. O. *In vitro* biotransformation of flavonoids by rat liver microsomes. *Xenobiotica*, **1998**, *28*, 389–401.

(65) Miyake, Y.; Shimoi, K.; Kumazawa, S.; Yamamoto, K.; Kinae, N.; Osawa, T. Identification and antioxidant activity of flavonoid metabolites in plasma and urine of eriocitrin-treated rats. *J. Agric. Food Chem.*, **2000**, *48*, 3217–3224.

(66) Bravo, L. Polyphenols: chemistry, dietary sources, metabolism, and nutritional significance. *Nutr. Rev.*, **1998**, *56*, 317–333.

(67) Marques Peixoto, F.; Fernandes, I.; Gouvea, A. C. M. S.; Santiago, M. C. P. A.; Galhardo Borguini, R.; Mateus, N.; Freitas, V.; Godoy, R. L. O.; Ferreira, I. M. P. L. V. O. Simulation of *in vitro* digestion coupled to gastric and intestinal transport models to estimate absorption of anthocyanins from peel powder of jabuticaba, jamelao and jambo fruits. *J. Funct. Foods*, **2016**, *24*, 373−381.

(68) Faria, A.; Pestana, D.; Azevedo, J.; Martel, F.; de Freitas, V.; Azevedo, I.; Mateus, N.; Calhau, C. Absorption of anthocyanins through intestinal epithelial cells − Putative involvement of GLUT2. *Mol. Nutr. Food Res.*, **2009**, *53*, 1430−1437.

(69) Zou, T. B.; Feng, D.; Song, G.; Li, H. W.; Tang, H. W.; Ling, W. H. The role of sodium-dependent glucose transporter 1 and glucose transporter 2 in the absorption of cyanidin-3-*O*-*β*-glucoside in Caco-2 cells. *Nutrients*, **2014**, *6*, 4165−4177.

(70) Steinert, R.; Ditscheid, B.; Netzel, M.; Jahreis, G. Absorption of black currant anthocyanins by monolayers of human intestinal epithelial Caco-2 cells mounted in Ussing type chambers. *J. Agric. Food Chem.*, **2008**, *56*, 4995−5001.

(71) Kosinska-Cagnazzo, A.; Diering, S.; Prim, D.; Andlauer, W.́Identification of bioaccessible and uptaken phenolic compounds from strawberry fruits in *in vitro* digestion/Caco-2 absorption model. *Food Chem.*, **2015**, *170*, 288−294.

(72) Yi, W.; Akoh, C. C.; Fischer, J.; Krewer, G. Absorption of anthocyanins from blueberry extracts by caco-2 human intestinal cell monolayers. *J. Agric. Food Chem.*, **2006**, *54*, 5651−5658.

(73) Kamiloglu, S.; Capanoglu, E.; Grootaert, C.; Van Camp, J. Anthocyanin Absorption and Metabolism by Human Intestinal Caco-2 Cells--A Review. *Int. J. Mol. Sci.*, **2015**, *16*, 21555−21574.

(74) Kim, Y. H.; Fujimura, Y.; Hagihara, T.; Sasaki, M.; Yukihira, D.; Nagao, T.; Miura, D.; Yamaguchi, S.; Saito, K.; Tanaka, H.; Wariishi, H.; Yamada, K.; Tachibana, H. *In situ* label-free imaging for visualizing the biotransformation of a bioactive polyphenol. *Sci. Rep.*, **2013**, *3*, 2805.

(75) Lorenz, M.; Urban, J.; Engelhardt, U.; Baumann, G.; Stangl, K.; Stangl, V. Green and black teas are equally potent stimuli of NO production and vasodilation: new insights into tea ingredients involved. *Basic Res. Cardiol.*, **2009**, *104*, 100–110.

(76) Loke, W. M.; Proudfoot, J. M.; Hodgson, J. M.; McKinley, A. J.; Hime, N.; Magat, M.; Stocker, R.; Croft, K. D. Specific dietary polyphenols attenuate atherosclerosis in apolipoprotein E-knowckout mice by alleviating inflammation and endothelial dysfunction. *Aerterioscler. Thromb. Vasc. Biol.*, **2010**, *30*, 749–757.

(77) Nguyen, H.-N.; Tanaka, M.; Li, B.; Ueno, T.; Matsuda, H.; Matsui, T. Novel *in situ* visualisation of rat intestinal absorption of polyphenols via matrix-assisted laser desorption/ionisation mass spectrometry. *Sci. Rep.*, **2019**, *9*, 3166.

(78) Lemaire, R.; Tabet, J. C.; Ducoroy, P.; Hendra, J. B.; Salzet, M.; Fournier, I. Solid ionic matrixes for direct tissue analysis and MALDI imaging. *Anal. Chem.*, **2006**, *78*, 809–819.

(79) Porta, T.; Lesur, A.; Varesio, E.; Hopfgartner, G. Quantification in MALDI-MS imaging: what can we learn from MALDI-selected reaction monitoring and what can we expect for imaging? *Anal. Bioanal. Chem.*, **2015**, *407*, 2177–2187.

(80) Gemperline, E.; Rawson, S.; Li, L. Optimization and comparison of multiple MALDI matrix application methods for small molecule mass spectrometric imaging. *Anal. Chem.*, **2014**, *86*, 10030–10035.

(81) Xie, H.; Wu, R.; Hung, Y. L. W.; Chen, X.; Chan, T. W. D. Development of a matrix sublimation device with controllable crystallization temperature for MALDI mass spectrometry imaging. *Anal. Chem.*, **2021**, *93*, 6342–6347.

(82) Benabdellah, F; Touboul, D; Brunelle, A; Laprevote, O. *In situ* primary metabolites localization on a rat brain section by chemical mass spectrometry imaging. *Anal. Chem.*, **2009**, *81*, 5557–5560.

(83) Harborne, J. B. Phenolic compounds in phytochemical methods a guide to modern techniques of plant analysis (third ed.). *New York*: *Chapman & Hall*, **1998**, 66–74.

(84) Pedersen, C., Kyle, J., Jenkinson, A., Gardner, P., Mcphail, D.;Duthie, G. Effects of blueberry and cranberry juice consumption on the plasma antioxidant capacity of healthy female volunteers. *Eur. J. Clin. Nutr.*, **2000**, *54*, 405–408.

(85) Soares, G.; de Moura, C.; Silva, M.; Vilegas, W.; Santamarina, A.; Pisani, L.; Ribeiro, D. Protective effects of purple carrot extract (*Daucus carota*) against rat tongue carcinogenesis induced by 4-nitroquinoline 1-oxide. *Med. Oncol.*, **2018**, *35*, 54.

(86) Wright, O.; Netzel, G.; & Sakzewski, A. A randomized, double-blind, placebocontrolled trial of the effect of dried purple carrot on body mass, lipids, blood pressure, body composition, and inflammatory markers in overweight and obese adults, the QUENCH trial. *Can. J. Physiol. Pharmacol*., **2013**, *91*, 480–488.

(87) Guo, X., Yang, B., Tan, J., Jiang, J., Li, D. Associations of dietary intakes of anthocyanins and berry fruits with risk of type 2 diabetes mellitus: a systematic review and meta-analysis of prospective cohort studies. *Eur. J. Clin. Nutr.*, **2016**, *70*, 1360–1367.

(88) Crozier, A.; Jaganath, I.; Clifford, M. Dietary phenolics: chemistry, bioavailability and effects on health. *Nat. Prod. Rep.*, **2009**, *26*, 1001–1043.

(89) liopoulou, I.; Thaeron, D.; Baker, A.; Jones, A.; Robertson, N. Analysis of the thermal degradation of the individual anthocyanin compounds of black carrot (*Daucus carota* L.): a new approach using high-resolution proton nuclear magnetic resonance Spectroscopy. *J. Agric. Food Chem.*, **2015**, *63*, 7066–7073.

(90) Glabgen, W.; Wray, V.; Strack, D.; Metzger, J.; Seitz, H. Anthocyanins from suspension cultures of Daucus carota. *Phytochemistry*, **1992**, *31*, 1593–1601.

(91) Alzaid, F.; Cheung, H.; Preedy, V.; Sharp, P. Regulation of glucose transporter expression in human intestinal Caco-2 cells following exposure to an anthocyaninrich berry extract. *PLoS ONE*, **2013**, *8*, e7893.

(92) Gee, J.; Dupont, M.; Day, A.; Plumb, G.; Williamson, G.; Johnson, I. Intestinal transport of quercetin glycosides in rats involves both deglycosylation and interaction with the hexose transport pathway. *J. Nutr.*, **2000**, *130*, 2765–2771.

(93) Malunga, L.; Eck, P.; Beta, T. Inhibition of intestinal α -glucosidase and glucose absorption by feruloylated arabinoxylan mono- and oligosaccharides from corn bran and wheat aleurone. *J. Nutr. Metab.*, **2016**, *5*, e00106.

(94) Fernandes, I.; Faria, A.; de Freitas, V.; Calhau, C.; Mateus, N. Multiple-approach studies to assess anthocyanin bioavailability. *Phytochem. Rev.*, **2015**, 14, 899–919.

(95) Clifford, M. Anthocyanins – nature, occurrence and dietary burden. *J. Sci. Food Agric.*, **2000**, *80*, 1063–1072.

(96) Tamai, I. Oral drug delivery utilizing intestinal OATP transporters. *Adv. Drug Deliv. Rev.*, **2012**, *64*, 508–514.

(97) Mikkaichi, T.; Suzuki, T.; Tanemoto, M.; Ito, S.; Abe, T. The organic anion transporter (OATP) Family. *Drug Metab. Pharmacokinet.*, **2004**, *19*, 171–179.

(98) Talavéra, S.; Felgines, C.; Texier, O.; Besson, C.; Manach, C.; Lamaison, J. L.; Rémésy, C. Anthocyanins are efficiently absorbed from the small intestine in rats. *J. Nutr.*, **2004**, *134*, 2275–2279.

(99) Tsuda, T.; Horio, F.; Uchida, K.; Aoki, H.; Osawa, T. Dietary cyanidin 3-*O*-*β*-D-glucoside-rich purple corn color prevents obesity and ameliorates hyperglycemia in mice. *J. Nutr.*, **2003**, *133*, 2125–2130.

(100) Karasu-Yalcin, S.; Soylemez-Milli, N.; Eren, O.; Eryasar-Orer, K. Reducing time in detection of *Listeria monocytogenes* from food by MALDI-TOF mass spectrometry. *J. Food Sci. Technol.* **2021**, *58*, 4102–4109.

(101) Tanaka, M.; Dohgu, S.; Komabayashi, G.; Kiyohara, H.; Takata, F.; Kataoka, Y.; Nirasawa, T.; Maebuchi, M.; Matsui T. Brain-transportable dipeptides across the blood-brain barrier in mice. *Sci. Rep.*, **2019**, *9*, 5769.

(102) Wang, J; Yang, E.; Chaurand, P.; Raghavan, V. Visualizing the distribution of strawberry plant metabolites at different maturity stages by MALDI-TOF imaging mass spectrometry. *Food Chem.*, **2021**, *345*, 128838.

(103) Nakagawa, K.; Tanaka, M.; Hahm, T. H.; Nguyen, H. N.; Matsui, T.; Chen Y. X.; Nakashima, Y. Accumulation of plasma-derived lipids in the lipid core and necrotic core of human atheroma: imaging mass spectrometry and histopathological analyses. *Arterioscler. Thromb. Vasc. Biol.*, **2021**, *41*, e498–e511.

(104) Chumbley, C. W.; Reyzer, M. L.; Allen, J. L.; Marriner, G. A.; Via, L. E.; Barry, C. E.; Caprioli, R. M. Absolute quantitative MALDI imaging mass spectrometry: a case of rifampicin in liver tissues. *Anal. Chem.*, **2016**, *88*, 2392–2398.

(105) Tang, W.; Chen, J.; Zhou, J.; Ge, J.; Zhang, Y.; Li, P.; Li. B. Quantitative MALDI imaging of spatial distributions and dynamic changes of tetrandrine in multiple organs of rats. *Theranostics*, **2019**, *9*, 932–944.

(106) Shiono, K.; Hashizaki, R.; Nakanishi, T.; Sakai, T.; Yamamoto, T.; Ogata, K.; Harada, K.; Ohtani, H.; Katano, H.; Taira, S. Multi-imaging of cytokinin and abscisic acid on the roots of rice (Oryza sativa) using matrix-assisted laser desorption/ionization mass spectrometry. *J. Agric. Food Chem.*, **2017**, *65*, 7624−7628.

(107) Unsihuay, D.; Sanchez, D. M.; Laskin, J. Quantitative mass spectrometry imaging of biological systems. *Annu. Rev. Phys. Chem.*, **2021**, *72*, 307-329.

(108) Yao, J.; Scott, J. R.; Young, M. K.; Wilkins, C. L. Importance of matrix: analyte ratio for buffer tolerance using 2,5-dihydroxybenzoic acid as a matrix in matrix-assisted laser desorption/ionization-fourier transform mass spectrometry and matrix-assisted laser desorption/ionization-time of flight. *J. Am. Soc. Mass Spectrom.*, **1998**, *9*, 805–813.

(109) Hanton, S.D.; Clark, P. A. C.; Owens, K. G.; Investigations of matrix-assisted laser desorption/ionization sample preparation by time-of-flight secondary ion mass spectrometry. *J. Am. Soc. Mass Spectrom.*, **1999**, *10*, 104-111.

(110) Albrethsen, J. Reproducibility in protein profiling by MALDI-TOF mass spectrometry. *Clin. Chem.*, **2007**, *53*, 852–858.

(111) Hamm, G.; Bonnel, D.; Legouffe, R.; Pamelard, F.; Delbos, J. M.; Bouzom, F.; Stauber, J. Quantitative mass spectrometry imaging of propranolol and olanzapine using tissue extinction calculation as normalization factor. *J. Proteomics*, **2012**, *75*, 4952–4961.

(112) Taga, Y.; Iwasaki, Y.; Shigemura, Y.; Mizuno, K. Improved *in vivo* tracking of orally administered collagen hydrolysate using stable isotope labeling and LC–MS techniques. *J. Agric. Food Chem.*, **2019**, *67*, 4671–4678.

(113) Norris, J. L.; Caprioli, R. M. Absolute quantification of rifampicin by MALDI imaging mass spectrometry using multiple TOF/TOF events in a single laser shot. *Chem. Rev.*, **2013**, *113*, 2309–2342.

(114) Pirman, D. A.; Reich, R. F.; Kiss, A.; Heeren, R. M. A.; Yost, R. A. Quantitative MALDI tandem mass spectrometric imaging of cocaine from brain tissue with a deuterated internal standard. *Anal. Chem.*, **2013**, *85*, 1081–1089.

(115) Sammour, D. A.; Marsching, C.; Geisel, A.; Erich, K.; Schulz, S.; Guevara, C. R.; Rabe, J. H.; Marx, A.; Findeisen, P.; Hohenberger, P.; Hopf, C. Quantitative mass spectrometry imaging reveals mutation status-independent lack of imatinib in liver metastases of gastrointestinal stromal tumors. *Sci. Rep.*, **2019**, *9*, 10698.

(116) Barry, J. A.; Ait-Belkacem, R.; Hardesty, W. M.; Benakli, L.; Andonian, C.; Licea-Perez, H.; Stauber, J.; Castellino, S. Multicenter validation study of quantitative imaging mass spectrometry. *Anal. Chem.*, **2019**, *91*, 6266–6274.

(117) Koeniger, S. L.; Talaty, N.; Luo, Y.; Ready, D.; Voorbach, M.; Seifert, T.; Cepa, S.; Fagerland, J. A.; Bouska, J.; Buck, W.; Johnson, R. W.; Spanton, S. A quantitation method for mass spectrometry imaging. *Rapid Commun. Mass Spectrom.*, **2011**, *25*, 503–510.

(118) Prentice, B. M.; Chumbley, C. W.; Caprioli, R. M. Absolute quantification of rifampicin by MALDI imaging mass spectrometry using multiple TOF/TOF events in a single laser shot. *J. Am. Soc. Mass. Spectrom.*, **2017**, 28, 136–144.

(119) Benabdellah, F.; Touboul, D.; Brunelle, A.; Laprevote, O. *In situ* primary metabolites localization on a rat brain section by chemical mass spectrometry imaging. *Anal. Chem.*, **2009**, *81*, 5557–5560.

(120) Rzagalinski, I.; Hainz, N.; Meier, C.; Tschernig, T.; Volmer, D. A. MALDI mass spectral imaging of bile acids observed as deprotonated molecules and proton-bound dimers from mouse liver sections. *J. Am. Soc. Mass Spectrom.*, **2018**, *29*, 711−722.

(121) Terahara, N.; Matsui, T.; Fukui, K. Matsugano, K.; Sugita, K. Matsumoto K. Caffeoylsophorose in a red vinegar produced through fermentation with purple sweetpotato. *J. Agric. Food Chem.* **2003**, *9*, 2539–2543.

(122) Zhang, J. L.; Zhang, G. D.; Zhou, T. H. Metabolism of ferulic acid in rats. *J. Asian Nat. Prod. Res.*, **2005**, *7*, 49–58.

(123) Zhao, Z.; Moghadasian M. H. Chemistry, natural sources, dietary intake and pharmacokinetic properties of ferulic acid: a review. *Food. Chem.*, **2008**, *109*, 691–702.

(124) Iwao, T.; Inoue, K.; Hayashi, Y.; Yuasa, H.; Watanabe, J. Metabolic extraction of nifedipine during absorption from the rat small intestine. *Drug Metab. Pharmacokin.*, **2002**, *17*, 546–553.

(125) Momma, K.; Takao, A. Fetal Cardiovascular effects of nifedipine in rats. *Pediatr. Res.*, **1989**, *26*, 442–447.

(126) Rashid, J.; Mckinstry, C.; Renwick, A. G.; Dirnhuber, M.; Waller, D. G.; George, C. F. Quercetin, an *in vitro* inhibitor of CYP3A, does not contribute to the interaction between nifedipine and grapefruit juice. *Br. J. clin. Pharmac.*, **1993**, *36*, 460–463.

(127) Chu, H. W.; Unnikrishnan, B.; Anand, A.; Mao, J. Y.; Huang, C. C. Nanoparticle-based laser desorption/ionization mass spectrometric analysis of drugs and metabolites. *JFDA*, **2018**, *4*, 1215–1228.

(128) Cornett, D. S.; Duncan, M. A.; Amster, I. Liquid mixtures for matrix-assisted laser desorption. *Anal. Chem.*, **1993**, *65*, 2608–2613.

(129) Sun, Z.; Findsen, E. W.; Isailovic, D. Atmospheric pressure visible-wavelength MALDI-MS, *Int. J. Mass Spectrom.*, **2012**, *315*, 66–73.

(130) Gary, R, P.; Michael, C. F.; Lloyd, M. S. Matrix-assisted laser desorption/ionization mass spectrometry of synthetic oligodeoxyribonucleotides. *Rapid Commun. Mass Spectrom.*, **1992**, *6*, 369–372.

(131) Van de Plas, R.; Yang, J.; Spraggins, J.; Caprioli, R. M. Image fusion of mass spectrometry and microscopy: a multimodality paradigm for molecular tissue mapping. *Nat. Methods*, **2015**, *12*, 366–372.

(132) Spraggins, J. M.; Djambazova, K. V.; Rivera, E. S.; Migas, L. G.; Neumann, E. K.; Fuetterer, A.; Suetering, J.; Goedecke, N.; Ly, A.; Van de Plas, R.; Caprioli, R. M. High-performance molecular imaging with MALDI trapped ion-mobility time-of-flight (timsTOF) mass spectrometry. *Anal. Chem.*, **2019**, *91*, 14552–14560.

(133) Wang, X.; Han, J.; Hardie, D. B.; Yang, J.; Pan. J.; Borchers, C. H. Metabolomic profiling of prostate cancer by matrix assisted laser desorption/ionization-fourier transform ion cyclotron resonance mass spectrometry imaging using matrix coating assisted by an electric field (MCAEF). *Biochim. Biophys. Acta.*, **2017**, *7*, 755–767.

(134) Schiller, J.; Süss, R.; Fuchs, B.; Müller, M.; Petković, M. Zschörnig, O.; Waschipky, H. The suitability of different DHB isomers as matrices for the MALDI-TOF MS analysis of phospholipids: which isomer for what purpose?. *Eur. Biophys. J.*, **2007**, *36*, 517–527.

(135) Dueñas, M. E.; Carlucci, L.; Lee, Y. J. Matrix recrystallization for MALDI-MS imaging of maize lipids at high-spatial resolution. *J. Am. Soc. Mass Spectrom.*, **2016**, *27*, 1575–1578.

(136) Hankin, J. A.; Barkley, R. M.; Murphy, R. C. Sublimation as a method of matrix application for mass spectrometric imaging. *J. Am. Soc. Mass Spectrom.*, **2007**, *18*, 1646–1652.

(137) Zaleski, J.; Daszkiewicz, Z.; Kyziol, J. B. Structure of N,4-dinitroaniline and its complex with sulfolane at 85 K; on the proton donor-acceptor affinity of the primary nitramine ($HNNO_2$) Group. *Acta Cryst.*, **2002**, B58, 109–115.

(138) Bu, R.; Xiong, Y.; Wei, X.; Li, H.; Zhang, C. Hydrogen bonding in CHON-containing energetic crystals: a review. *Cryst. Growth Des.*, **2019**, *19*, 5981–5997.

(139) Quinn, J. R.; Zimmerman, S. C.; Del Bene, J. E.; Shavitt, I. Does the A·T or G·C base-pair possess enhanced stability? Quantifying the effects of CH···O interactions and secondary interactions on base-pair stability using a phenomenological analysis and ab initio calculations. *J. Am. Chem. Soc.*, **2007**, *129*, 934–941.

(140) Deegan, R. D.; Bakajin, O.; Dupont, T. F.; Huber, G.; Nagel, S. R.; Witten, T. A. Capillary flow as the cause of ring stains from dried liquid drops. *Nature*, **1997**, *389*, 827–829.

(141) Medina, N.; Huth-Fehre, T.; Westman, A. Matrix-assisted laser desorption: dependence of the threshold fluence on analyte concentration. *J. Mass Spectrom.*, **1994**, *29*, 207–209.

(142) Dreisewerd, K.; Schürenberg, M.; Karas, M.; Hillenkamp, F. Influence of The laser intensity and spot size on the desorption of molecules and ions in matrix-assisted laser desorption/ionization with a uniform beam profile. *Int. J. Mass Spectrom. Ion Processes*, **1995**, *141*, 127−148.

(143) Aichler, M.; Walch, A. MALDI imaging mass spectrometry: current frontiers and perspectives in pathology research and practice. *Lab. Invest.*, **2015**, *95*, 422–431.

(144) Gessel, M. M.; Norris, J. L.; Caprioli, R. M. MALDI imaging mass spectrometry: spatial molecular analysis to enable a new age of discovery. *J. Proteom.*, **2014**, *107*, 71–82.

(145) Caprioli, R. M. Imaging mass spectrometry: enabling a new age of discovery in biology and medicine through molecular microscopy. *J. Am. Soc. Mass Spectrom.*, **2015**, *26*, 850–852.

(146) Rzagalinski I, Kovačević B., Hainz N., Meier C., Tschernig T., Volmer DA. Toward higher sensitivity in quantitative MALDI imaging mass spectrometry of CNS drugs using a nonpolar matrix. *Anal. Chem.*, **2018**, *90*, 12592−12600.

Acknowledgements

Undertaking this doctoral degree has been a precious and enriching experience for me, which would not have been possible without the guidance and support I received from many people.

There have been a number of people without whom this doctoral dissertation could not have been completed. I owe a real debt of my gratitude to all those people who have made this dissertation possible and give me the graduate experience that I will forever cherish.

First and foremost, I am immensely grateful to Prof. Toshiro Matsui who supported me enormously over these past five years with an abiding and deep interest in any given situation. It is been great pleasure studying with a supervisor who taught so much about my research with his erudition and scientific expertise, and also who cared about my life of studying in Japan. His passion, guidance, and discipline have been indispensable to my growth as a scientist and as a person during my doctoral degree term.

Furthermore, I would like to express my sincere gratitude to Asst. Prof. Mitsuru Tanaka for giving me invaluable advice. During these five years, he has constantly shared with me his valuable knowledge and plentiful experience, thanks to his help and support, I was able to finish my doctoral course and enjoy successful life in Japan. Besides, I would like to thank the rest of my doctoral dissertation committee Prof. Furuya Shigeki. In addition, I would like to express my sincere appreciation to Kaori Miyazaki for taking care of all official matters to keep studying without any official problems and for invaluable and efficient help and technical support in many kinds of situations, from laboratory work to the booking hotel and public transport ticket for national and international conferences.

Specially, I am deeply grateful to all the members of Food Analysis Laboratory for their kindness and cherished time spent together in the lab, and in social settings. I received much more than all I had been expecting, thank you so much for your boundless generosity, you have made my study and wonderful time in japan.

I would also like to offer my special thanks to the Rotary Yoneyama Scholarship in japan for the financial support during my Ph.D.

Most of all, I express my appreciation to my wife and loving family for their unconditional and unwavering support. Without their deep love, understanding, encouragement, and belief in me, I would not have achieved this glory and happy day. I love you so much and thank you.